

Klimaänderung II

5. Der globale Kohlenstoff, andere biogeochemische Zyklen und Rückkopplungen

Robert Sausen

Institut für Physik der Atmosphäre
Deutsches Zentrum für Luft- und Raumfahrt
Oberpfaffenhofen

Vorlesung SS 2023

LMU München



Knowledge for Tomorrow

Technical information

- <http://www.pa.op.dlr.de/~RobertSausen/vorlesung/index.html>
 - Most recent update on the lecture
 - Slides of the lecture (with some delay)

 - See also LSF <https://lsf.verwaltung.uni-muenchen.de/>

- Contact: robert.sausen@dlr.de

- Further information:
 - www.ipcc.ch
 - www.de-ipcc.de



Contents of IPCC AR 6 2021: Working Group I: the Physical Science Basis

Chapters

- Chapter 1 Framing, Context, and Methods
- Chapter 2 Changing State of the Climate System
- Chapter 3 Human Influence on the Climate System
- Chapter 4 Future Global Climate: Scenario-based Projections and Near-term Information
- Chapter 5 Global Carbon and Other Biogeochemical Cycles and Feedbacks**
- Chapter 6 Short-lived Climate Forcers
- Chapter 7 The Earth's Energy Budget, Climate Feedbacks and Climate Sensitivity
- Chapter 8 Water Cycle Changes
- Chapter 9 Ocean, Cryosphere and Sea Level Change
- Chapter 10 Linking Global to Regional Climate Change
- Chapter 11 Weather and Climate Extreme Events in a Changing Climate
- Chapter 12 Climate Change Information for Regional Impact and for Risk Assessment
- Atlas

IPCC 2021



Chapter 5: Global Carbon and other Biogeochemical Cycles and Feedbacks

Coordinating Lead Authors:

Josep G. Canadell (Australia), Pedro M.S. Monteiro (South Africa)

Lead Authors:

Marcos H. Costa (Brazil), Leticia Cotrim da Cunha (Brazil), Peter M. Cox (United Kingdom), Alexey V. Eliseev (Russian Federation), Stephanie Henson (United Kingdom), Masao Ishii (Japan), Samuel Jaccard (Switzerland), Charles Koven (United States of America), Annalea Lohila (Finland), Prabir K. Patra (Japan/India), Shilong Piao (China), Joeri Rogelj (United Kingdom/Belgium), Stephen Syampungani (Zambia), **Sönke Zaehle (Germany)**, **Kirsten Zickfeld (Canada/Germany)**



Chapter 5: Global Carbon and other Biogeochemical Cycles and Feedbacks

Contributing Authors:

Georgii A. Alexandrov (Russian Federation), Govindasamy Bala (India/ United States of America), Laurent Bopp (France), **Lena Boysen (Germany)**, Long Cao (China), Naveen Chandra (Japan/India), Philippe Ciais (France), Sergey N. Denisov (Russian Federation), Frank J. Dentener (EU, The Netherlands), Hervé Douville (France), Amanda Fay (United States of America), Piers Forster (United Kingdom), Baylor Fox-Kemper (United States of America), Pierre Friedlingstein (United Kingdom), Weiwei Fu (United States of America /China), **Sabine Fuss (Germany)**, Véronique Garçon (France), **Bettina Gier (Germany)**, Nathan P. Gillett (Canada), Luke Gregor (Switzerland/South Africa), **Karsten Haustein (United Kingdom /Germany)**, Vanessa Haverd (Australia), Jian He (United States of America /China), Helene T. Hewitt (United Kingdom), Forrest M. Hoffman (United States of America), **Tatiana Ilyina (Germany)**, Robert Jackson (United States of America), Christopher Jones (United Kingdom), **David P. Keller (Germany/ United States of America)**, Lester Kwiatkowski (France/ United Kingdom), Robin D. Lamboll (United Kingdom/United States of America, United Kingdom), Xin Lan (United States of America/China), **Charlotte Laufkötter (Switzerland/Germany)**, Corinne Le Quéré (United Kingdom), Andrew Lenton (Australia), Jared Lewis (Australia/New Zealand), Spencer Liddicoat (United Kingdom), Laura Lorenzoni (United States of America/Venezuela), Nicole Lovenduski (United States of America), Andrew H. MacDougall (Canada), **Sabine Mathesius (Canada/Germany)**, Damon H. Matthews (Canada), **Malte Meinshausen (Australia/Germany)**, Igor I. Mokhov (Russian Federation), Vaishali Naik (United States of America), Zebedee R. J. Nicholls (Australia), Intan Suci Nurhati (Indonesia), Michael O'Sullivan (United Kingdom), Glen Peters (Norway), **Julia Pongratz (Germany)**, Benjamin Poulter (United States of America), Jean-Baptiste Sallée (France), Marielle Saunois (France), Edward A.G. Schuur (United States of America), Sonia I. Seneviratne (Switzerland), Ann Stavert (Australia), Parvatha Suntharalingam (United Kingdom/United States of America), Kaoru Tachiiri (Japan), Jens Terhaar (Switzerland/Germany), Rona Thompson (Norway, Luxembourg/New Zealand), Hanqin Tian (United States of America), Jocelyn Turnbull (New Zealand), Sergio M. Vicente-Serrano (Spain), Xuhui Wang (China), Rik Wanninkhof (United States of America), Phil Williamson (United Kingdom)



Chapter 5: Global Carbon and other Biogeochemical Cycles and Feedbacks

Review Editors:

Victor Brovkin (Germany/Russian Federation), Richard A. Feely (United States of America)

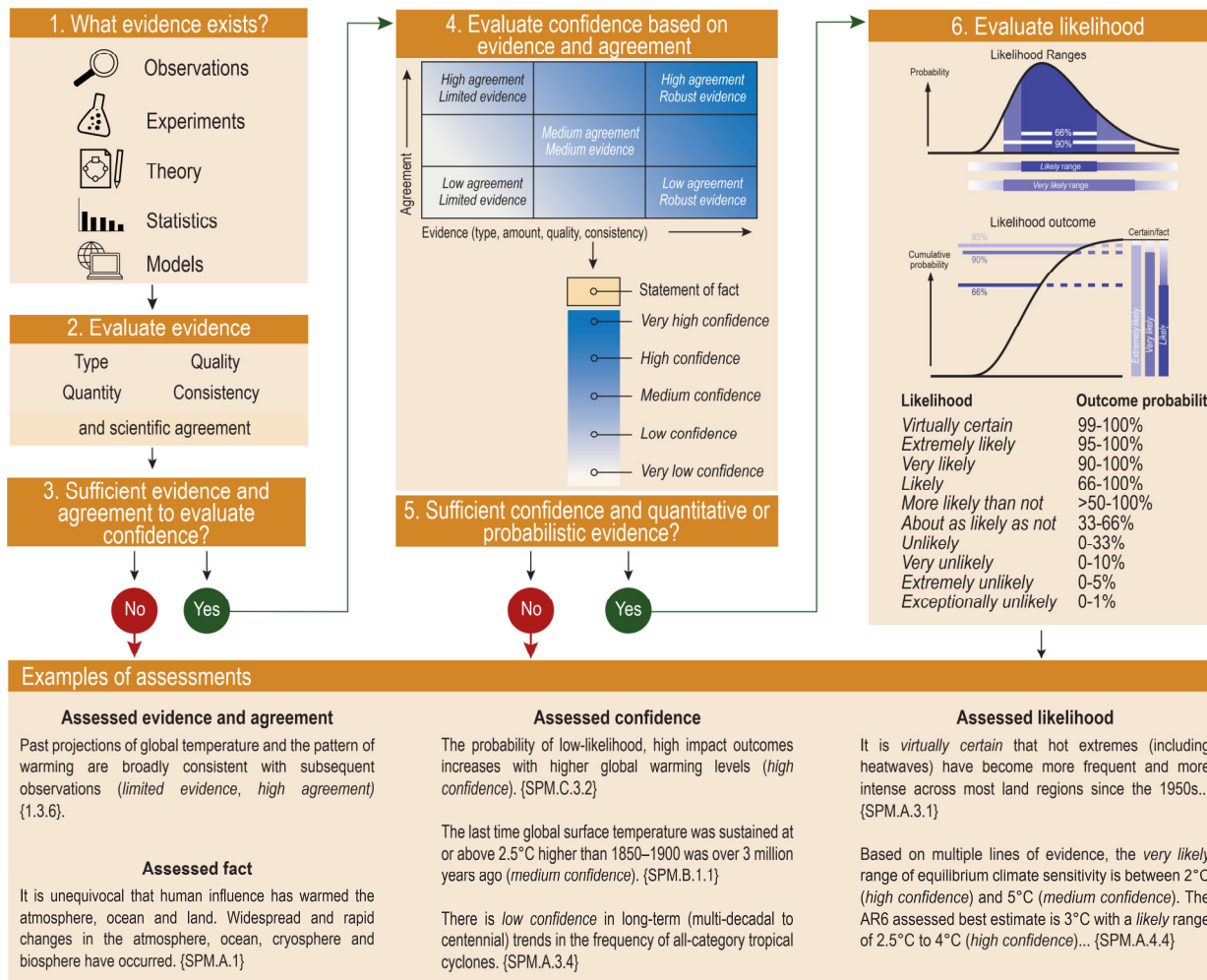
Chapter Scientist:

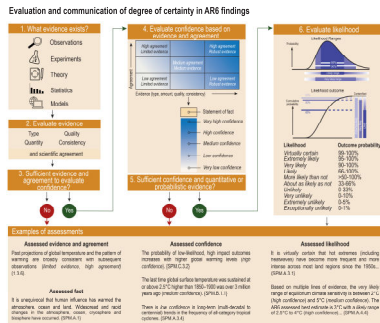
Alice D. Lebehot (South Africa/France)





Evaluation and communication of degree of certainty in AR6 findings





4. Evaluate confidence based on evidence and agreement

Agreement ↑	High agreement Limited evidence		High agreement Robust evidence
		Medium agreement Medium evidence	
	Low agreement Limited evidence		Low agreement Robust evidence
	Evidence (type, amount, quality, consistency) →		

5. Sufficient confidence and quantitative or probabilistic evidence?



- Statement of fact
- Very high confidence
- High confidence
- Medium confidence
- Low confidence
- Very low confidence

6. Evaluate likelihood



Likelihood	Outcome probability
Virtually certain	99-100%
Extremely likely	95-100%
Very likely	90-100%
Likely	66-100%
More likely than not	>50-100%
About as likely as not	33-66%
Unlikely	0-33%
Very unlikely	0-10%
Extremely unlikely	0-5%
Exceptionally unlikely	0-1%

Statements in the Executive Summary

It is unequivocal that emissions of the well-mixed greenhouse gases (GHG) carbon dioxide (CO₂), methane (CH₄) and nitrous oxide (N₂O) from human activities are the main driver of increases in atmospheric GHG concentrations since the pre-industrial period.

The accumulation of GHGs in the atmosphere is determined by the balance between anthropogenic emissions, anthropogenic removals, and physical-biogeochemical source and sink dynamics on land and in the ocean.

This chapter assesses how physical and biogeochemical processes of the carbon and nitrogen cycles affect the variability and trends of GHGs in the atmosphere as well as ocean acidification and deoxygenation.

It identifies physical and biogeochemical feedbacks that have affected or could affect future rates of GHG accumulation in the atmosphere, and therefore, influence climate change and its impacts.

This chapter also assesses the remaining carbon budget to limit global warming within various goals, as well as the large-scale consequences of carbon dioxide removal (CDR) and solar radiation modification (SRM) on biogeochemical cycles {Figures 5.1, 5.2}.

Chapter 5: Carbon and biogeochemical cycles

Chapter 5 identifies biogeochemical feedbacks with potentially significant climatic effects.

Section 5.1
Introduction and the paleo context

Section 5.2
Historical trends, variability & budgets of

5.2.1 ● CO₂ **5.2.2** ● CH₄ **5.2.3** ● N₂O **Section 5.2.4** ● ● Relative importance of CO₂, CH₄ and N₂O

Section 5.3
Ocean acidification and deoxygenation

Section 5.4
Biogeochemical feedbacks on climate change

Section 5.5
Remaining carbon budgets

Section 5.6
Implications of CO₂ removal and solar radiation modification

Section 5.7
Final remarks

FAQs

Boxes

Box 5.1
Permafrost

Box 5.2
Carbon budget improvements and implications

Box 5.3
Response to CO₂ removal

Chapter 5: Quick guide

Key topics and corresponding sub-sections

- Anthropogenic greenhouse gas emissions
5.2.1.1 | **5.2.2.2** | **5.2.3.2** | **5.2.4**
- CO₂ and non-CO₂ biogeochemical feedbacks
5.1.1 | **Box 5.1** | **5.4.7** | **5.4.8** | **5.4.9**
- Future projections
5.3.4 | **5.4.5** | **5.4.10**
- Historical and remaining greenhouse gas budgets
5.2.1.5 | **5.2.2.5** | **5.2.3.5** | **5.5.2**
- Mitigation, negative emissions and solar radiation modification
5.5 | **5.6**
- Ocean sinks, acidification and deoxygenation
5.2.1.3 | **5.3.2** | **5.3.3**
- Paleo context
5.1.2 | **5.3.1**

Cross-chapter boxes

CC Box 5.1
Land Carbon-Water Interactions

CC Box 5.2
Drivers of atmospheric methane change

CC Box 5.3
Ocean carbon-heat nexus

Figure 5.1 | Visual guide to Chapter 5.
IPCC 2021, Chap. 5



Key compartments, processes and pathways that govern historical and future CO₂ concentrations and carbon–climate feedbacks

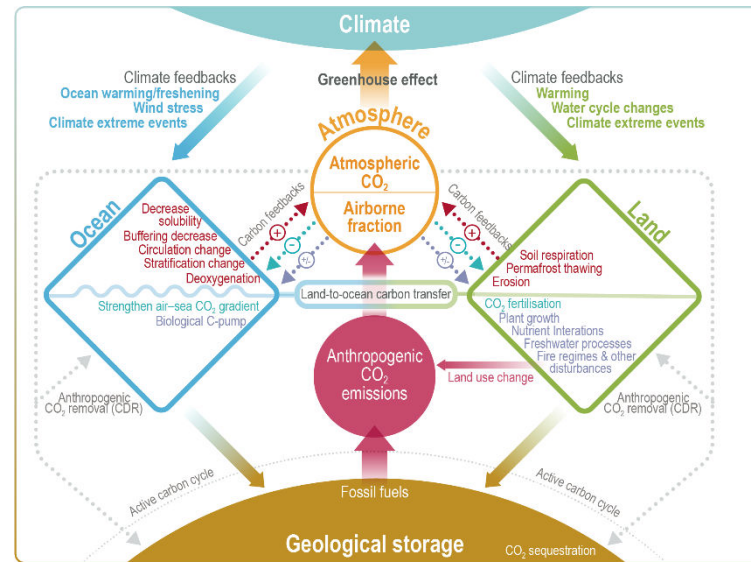
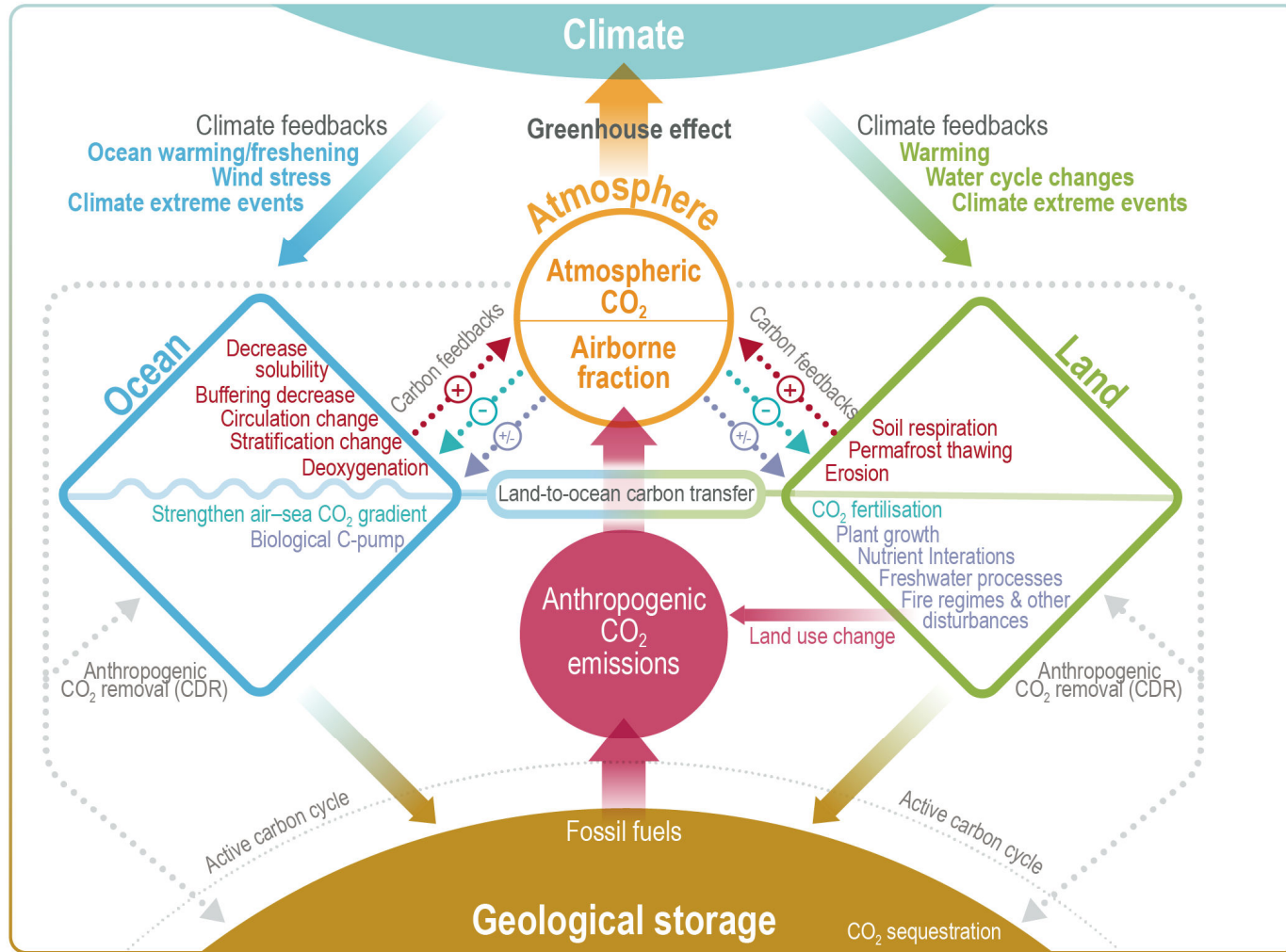


Figure 5.2 | Key compartments, processes and pathways that govern historical and future CO₂ concentrations and carbon–climate feedbacks through the coupled Earth system. The anthropogenic CO₂ emissions, including land-use change, are partitioned via negative feedbacks (turquoise dotted arrows) between the ocean (23%), the land (31%) and the airborne fraction (46%) of anthropogenic CO₂ that sets the changing CO₂ concentration in the atmosphere (2010–2019; Table 5.1). This regulates most of the radiative forcing that creates the heat imbalance that drives the climate feedbacks to the ocean (blue) and land (green). Positive feedbacks (red arrows) result from processes in the ocean and on land (red text). Positive feedbacks are influenced by both carbon-concentration and carbon–climate feedbacks simultaneously. Additional biosphere processes have been included, but these have an as-yet-uncertain feedback impact (blue-dotted arrows). CO₂ removal from the atmosphere into the ocean, land and geological reservoirs, necessary for negative emissions, has been included (grey arrows). Although this schematic is built around CO₂ (the dominant greenhouse gas), some of the same processes also influence the fluxes of CH₄ and N₂O and the strength of the positive feedbacks from the terrestrial and ocean systems.



Statements in the Executive Summary

The Human Perturbation of the Carbon and Biogeochemical cycles

Global mean concentrations for well-mixed GHGs (CO₂, CH₄ and N₂O) in 2019 correspond to increases of about 47%, 156%, and 23%, respectively, above the levels in 1750 (representative of the pre-industrial) (*high confidence*). Current atmospheric concentrations of the three GHGs are higher than at any point in the last 800,000 years, and in 2019 reached 409.9 ppm of CO₂, 1866.3 ppb of CH₄, and 332.1 ppb of N₂O (*very high confidence*). Current CO₂ concentrations in the atmosphere are also unprecedented in the last 2 million years (*high confidence*). In the past 60 Myr, there have been periods in Earth's history when CO₂ concentrations were significantly higher than at present, but multiple lines of evidence show that the rate at which CO₂ has increased in the atmosphere during 1900–2019 is at least 10 times faster than at any other time during the last 800,000 years (*high confidence*), and 4-5 times faster than during the last 56 million years (*low confidence*). {5.1.1, 2.2.3; Figures 5.3, 5.4; Cross-Chapter Box 2.1}



Atmospheric CO₂ concentrations and growth rates for the past 60 million years and projections to 2100

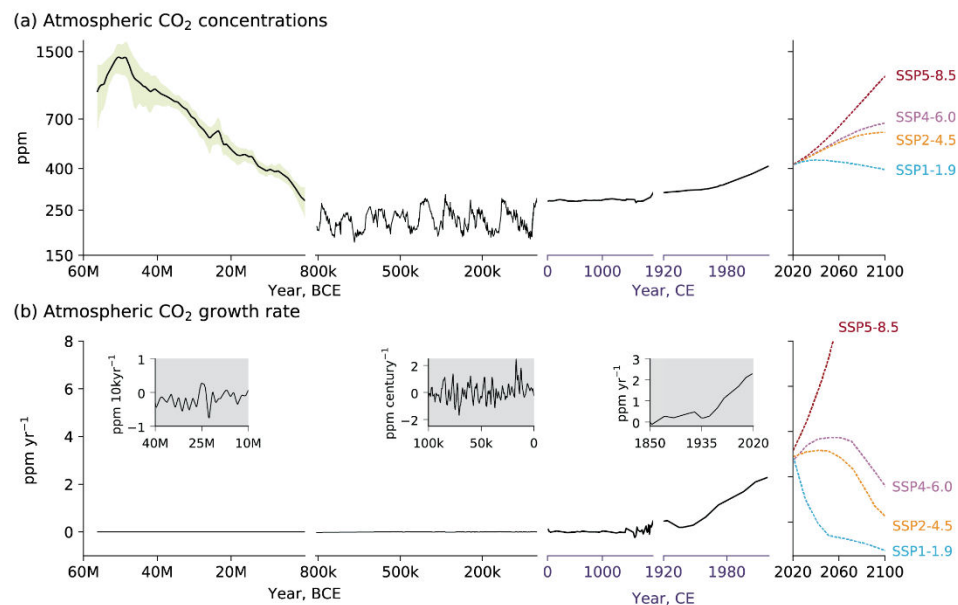
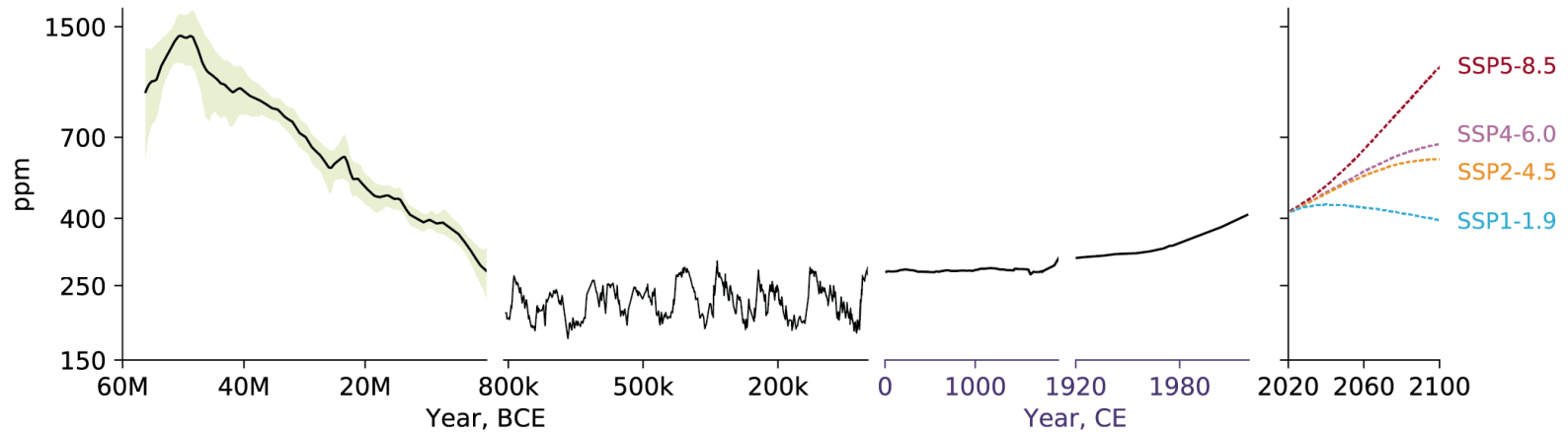


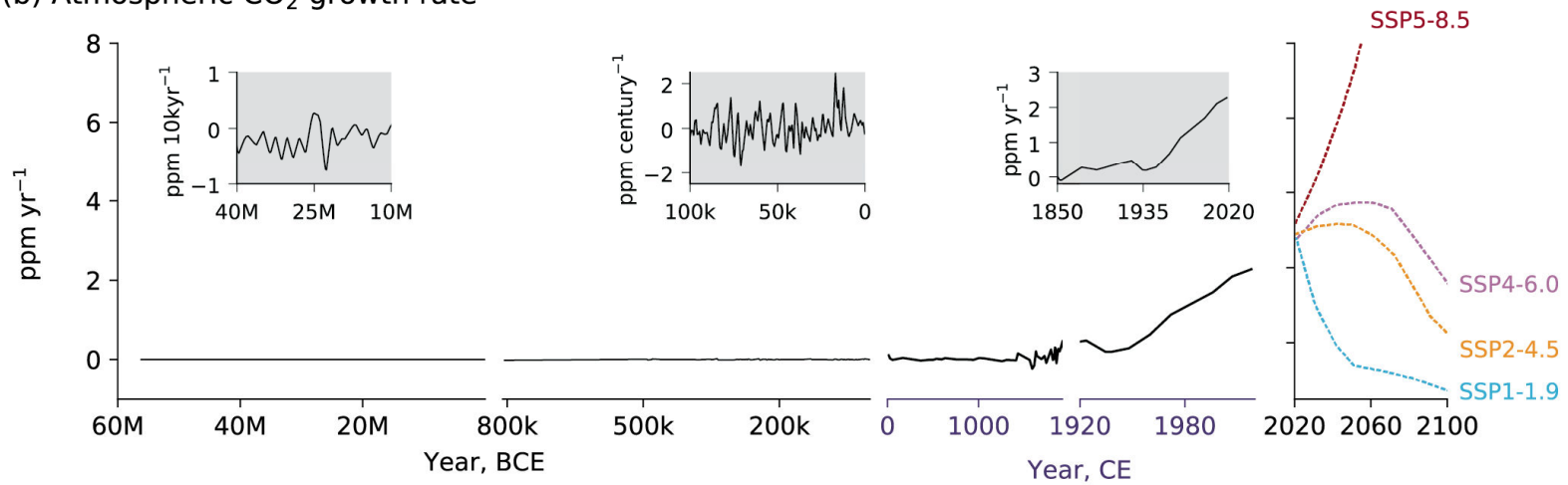
Figure 5.3 | Atmospheric CO₂ concentrations and growth rates for the past 60 million years (Myr) and projections to 2100. (a) CO₂ concentrations data for the period 60 Myr to the time prior to 800 kyr (left column) are shown as the LOESS Fit and 68% range (data from Chapter 2) (Foster et al., 2017). Concentrations from 1750 and projections through 2100 are taken from Shared Socio-economic Pathways of IPCC AR6 (Meinshausen et al., 2017). (b) Growth rates are shown as the time derivative of the concentration time series. Inserts in (b) show growth rates at the scale of the sampling resolution. Further details on data sources and processing are available in the chapter data table (Table 5.SM.6).



(a) Atmospheric CO₂ concentrations



(b) Atmospheric CO₂ growth rate



Atmospheric concentrations of CO₂, CH₄ and N₂O in air bubbles and clathrate crystals in ice cores (800,000 BCE to 1990 CE)

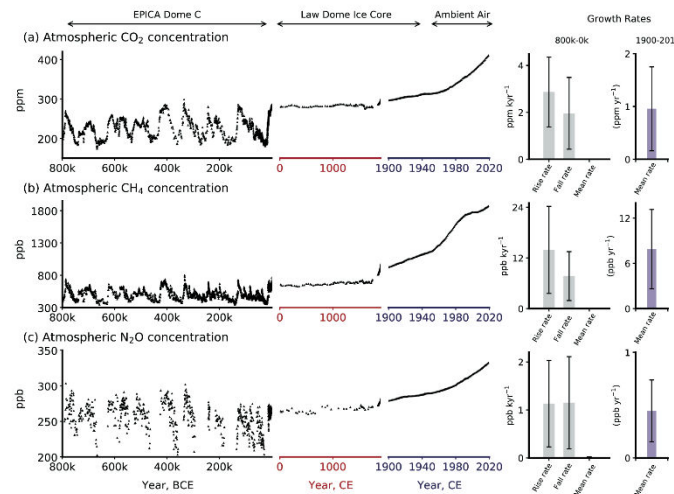
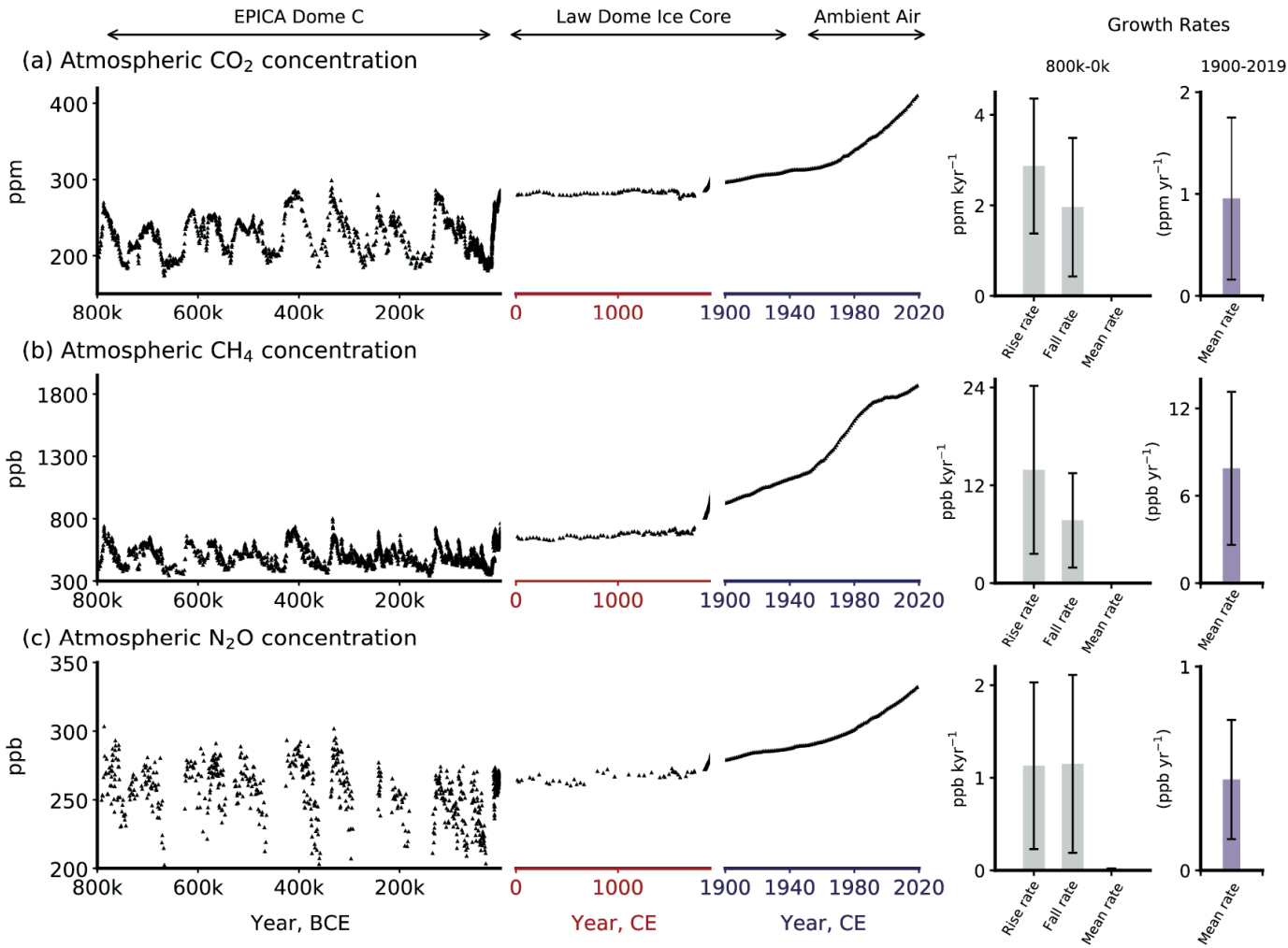


Figure 5.4 | Atmospheric concentrations of CO₂, CH₄ and N₂O in air bubbles and clathrate crystals in ice cores (800,000 BCE to 1990 CE). Note the variable x-axis range and tick mark intervals for the three columns. Ice core data is over-plotted by atmospheric observations from 1958 to present for CO₂, from 1984 for CH₄ and from 1994 for N₂O. The time-integrated, millennial-scale linear growth rates for different time periods (800,000–0 BCE, 0–1900 CE and 1900–2017 CE) are given in each panel. For the BCE period, mean rise and fall rates are calculated for the individual slopes between the peaks (interglacials) and troughs (glacial periods), which are given in the panels in left column. The data for BCE period are used from the Vostok, EPICA, Dome C and WAIS ice cores (Petit et al., 1999; Monnin, 2001; Pépin et al., 2001; Raynaud et al., 2005; Siegenthaler et al., 2005; Loulergue et al., 2008; Lüthi et al., 2008; Schilt et al., 2010a). The data after 0–yr CE are taken mainly from Law Dome ice core analysis (MacFarling Meure et al., 2006). The surface observations for all species are taken from NOAA cooperative research network (Dlugokencky and Tans, 2019), where ALT, MLO and SPO stand for Alert (Canada), Mauna Loa Observatory, and South Pole Observatory, respectively. BCE = before current era, CE = current era. Further details on data sources and processing are available in the chapter data table (Table 5.SM.6).





22.05.2023



Statements in the Executive Summary

Contemporary Trends of Greenhouse Gases (1)

It is unequivocal that the increase of CO₂, CH₄, and N₂O in the atmosphere over the industrial era is the result of human activities (*very high confidence*). This assessment is based on multiple lines of evidence including atmospheric gradients, isotopes, and inventory data. During the last measured decade, global average annual anthropogenic emissions of CO₂, CH₄, and N₂O, reached the highest levels in human history at 10.9 ± 0.9 PgC yr⁻¹ (2010–2019), 335–383 Tg CH₄ yr⁻¹ (2008–2017), and 4.2–11.4 TgN yr⁻¹ (2007–2016), respectively (*high confidence*). {5.2.1, 5.2.2, 5.2.3, 5.2.4; Figures 5.6, 5.13, 5.15}.

$$1 \text{ Pg} = 10^{15} \text{ g} = 10^9 \text{ Mg} = 10^9 \text{ t}$$



Statements in the Executive Summary

Contemporary Trends of Greenhouse Gases (2)

The CO₂ emitted from human activities during the decade of 2010–2019 (decadal average 10.9 ± 0.9 PgC yr⁻¹) was distributed between three Earth system components: 46% accumulated in the atmosphere (5.1 ± 0.02 PgC yr⁻¹), 23% was taken up by the ocean (2.5 ± 0.6 PgC yr⁻¹) and 31% was stored by vegetation in terrestrial ecosystems (3.4 ± 0.9 PgC yr⁻¹) (*high confidence*). Of the total anthropogenic CO₂ emissions, the combustion of fossil fuels was responsible for 81–91%, with the remainder being the net CO₂ flux from land-use change and land management (e.g., deforestation, degradation, regrowth after agricultural abandonment or peat drainage). {5.2.1.2, 5.2.1.5; Table 5.1; Figures 5.5, 5.7, 5.12}



Global anthropogenic CO₂ emissions

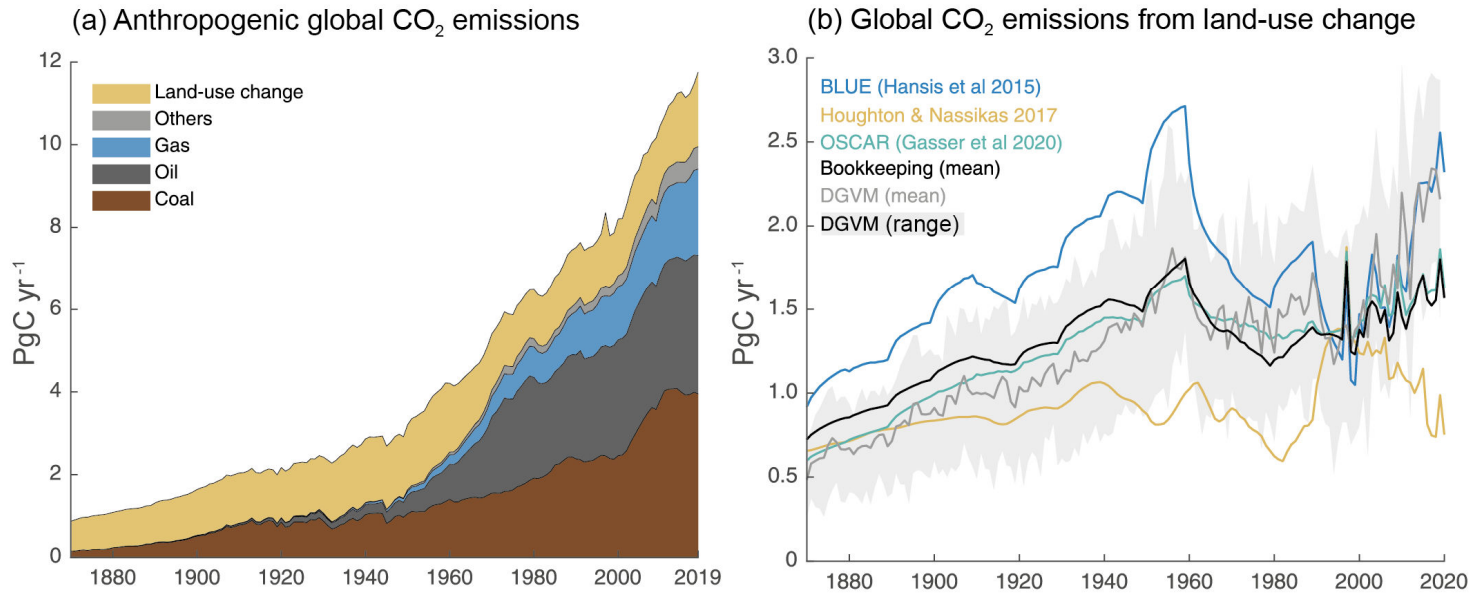
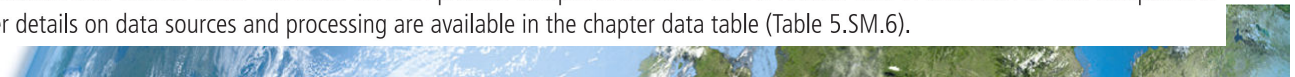
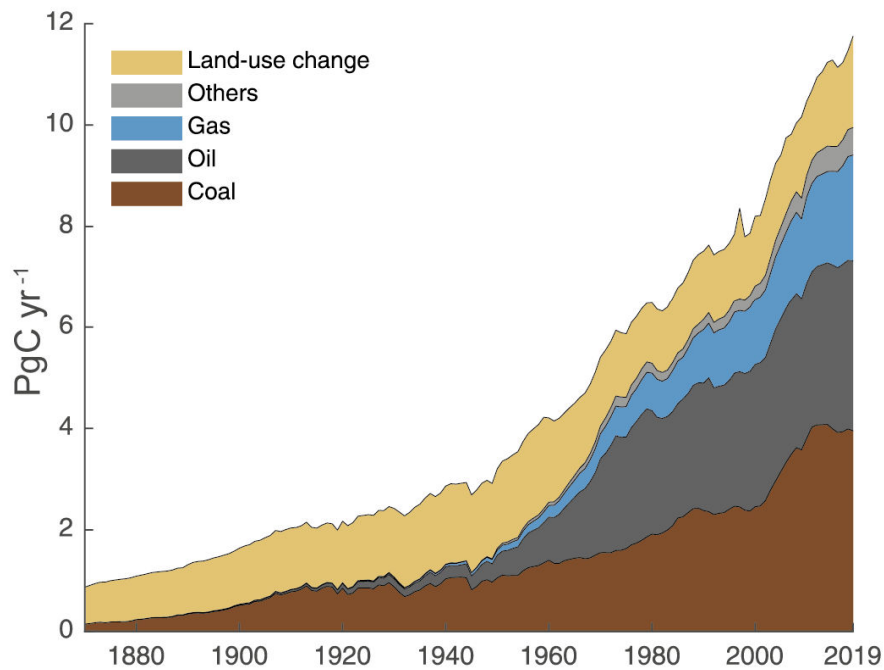


Figure 5.5 | Global anthropogenic CO₂ emissions. (a) Historical trends of anthropogenic CO₂ emissions (fossil fuels and net land-use change, including land management, called LULUCF flux in the main text) for the period 1870 to 2019, with ‘others’ representing flaring, emissions from carbonates during cement manufacture. Data sources: (Boden et al., 2017; IEA, 2017; Andrew, 2018; BP, 2018; Le Quéré et al., 2018a; Friedlingstein et al., 2020). (b) The net land-use change CO₂ flux (PgC yr⁻¹) as estimated by three bookkeeping models and 16 Dynamic Global Vegetation Models (DGVMs) for the global annual carbon budget 2019 (Friedlingstein et al., 2020). The three bookkeeping models are from Hansis et al., 2015; Houghton and Nassikas, 2017; Gasser et al., 2020 and are all updated to 2019. Their average is used to determine the net land-use change flux in the annual global carbon budget (black line). The DGVM estimates are the result of differencing a simulation with and without land-use changes run under observed historical climate and CO₂, following the Trendy v9 protocol (<https://sites.exeter.ac.uk/trendy/protocol/>); they are used to provide an uncertainty range to the bookkeeping estimates (Friedlingstein et al., 2020). All estimates are unsmoothed annual data. Estimates differ in process comprehensiveness of the models and in definition of flux components included in the net land use change flux. Further details on data sources and processing are available in the chapter data table (Table 5.SM.6).

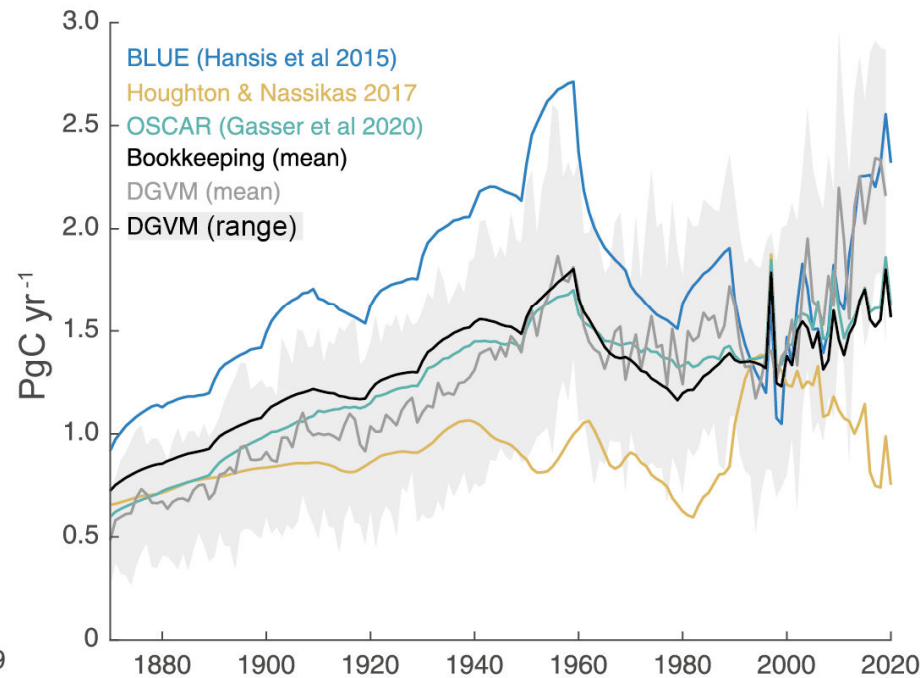


Global anthropogenic CO₂ emissions

(a) Anthropogenic global CO₂ emissions



(b) Global CO₂ emissions from land-use change



Statements in the Executive Summary

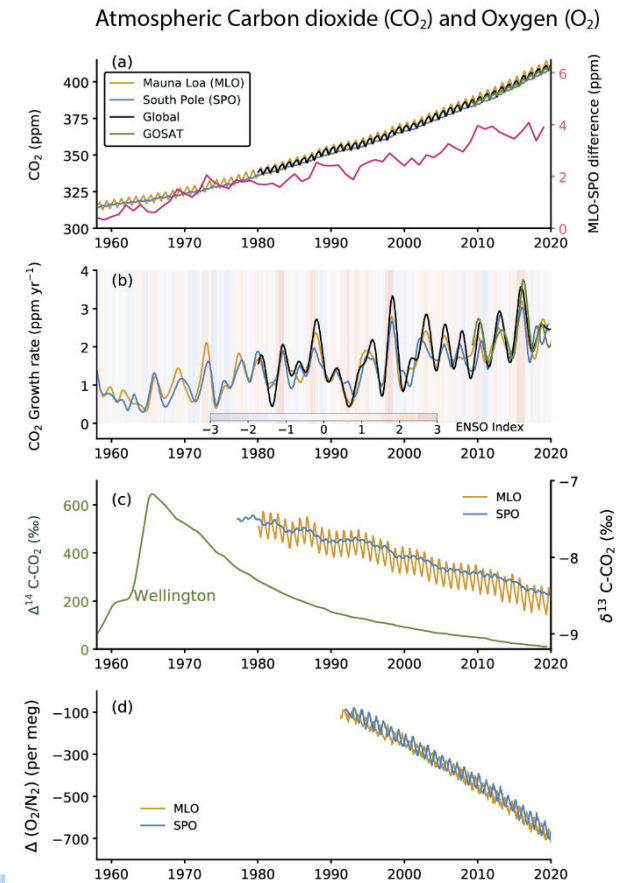
Contemporary Trends of Greenhouse Gases (3)

Over the past six decades, the average fraction of anthropogenic CO₂ emissions that has accumulated in the atmosphere (referred to as the airborne fraction) has remained nearly constant at approximately 44%. The ocean and land sinks of CO₂ have continued to grow over the past six decades in response to increasing anthropogenic CO₂ emissions (*high confidence*). Interannual and decadal variability of the regional and global ocean and land sinks indicate that these sinks are sensitive to climate conditions and therefore to climate change (*high confidence*). {5.2.1.1, 5.2.1.3, 5.2.1.4.2; Figures 5.7, 5.8, 5.10}



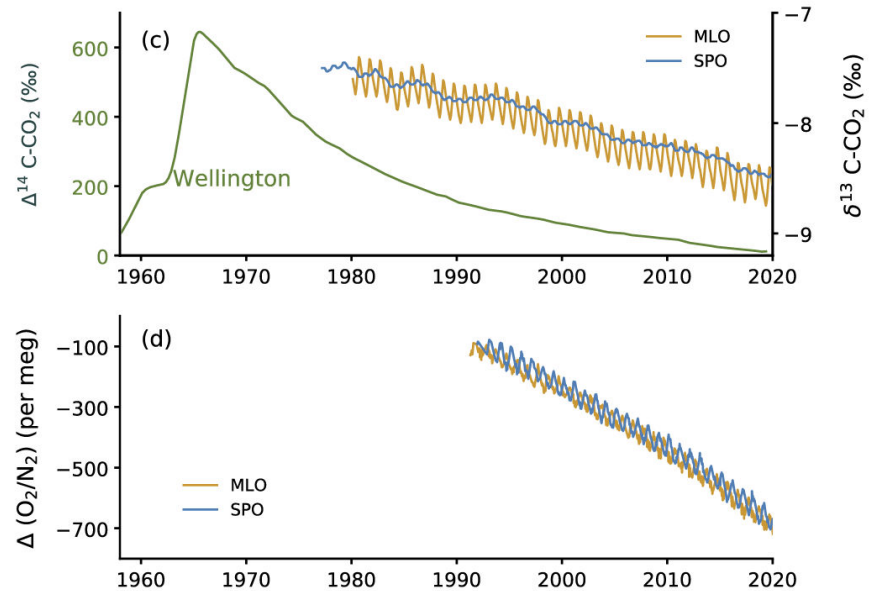
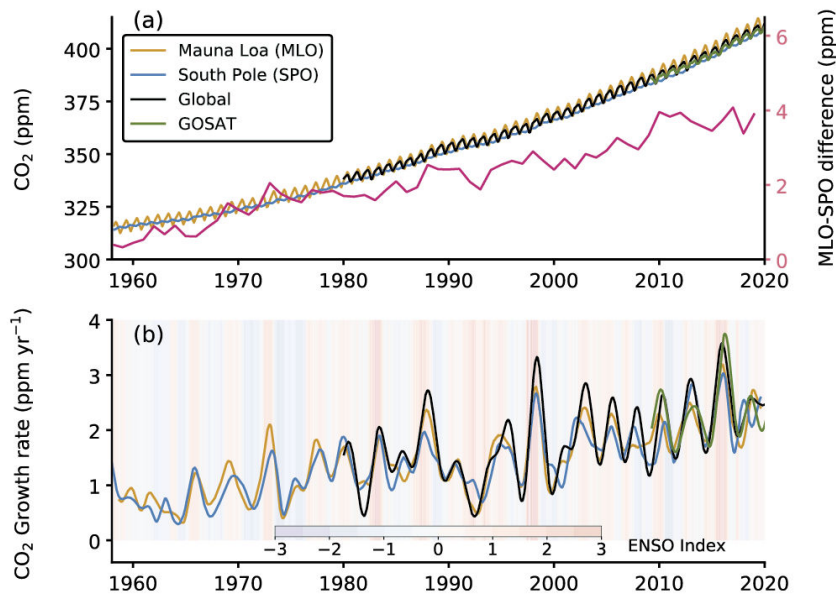
Time series of CO₂ concentrations and related measurements in ambient air

Figure 5.6 | Time series of CO₂ concentrations and related measurements in ambient air. (a) Concentration time series and MLO-SPO difference, (b) growth rates, (c) ¹⁴C and ¹³C isotopes, and (d) O₂/N₂ ratio. The data for Mauna Loa Observatory (MLO) and South Pole Observatory (SPO) are taken from the Scripps Institution of Oceanography (SIO)/University of California, San Diego (Keeling et al., 2001). The global mean CO₂ are taken from National Oceanic and Atmospheric Administration (NOAA) cooperative network (as in Chapter 2), and Greenhouse Gases Observing Satellite (GOSAT) monthly mean XCO₂ (mixing ratio) time series are taken from National Institute for Environmental Studies (Yoshida et al., 2013). CO₂ growth rates are calculated as the time derivative of deseasonalized time series (Nakazawa et al., 1997). The D(O₂/N₂) are expressed in per meg units (= (FF/M) × 10⁶, where FF = moles of O₂ consumed by fossil-fuel burning, M = 3.706 × 10¹⁹, total number of O₂ molecules in the atmosphere (Keeling and Manning, 2014). The ¹⁴CO₂ time series at Barring Head, Wellington, New Zealand (BHD) is taken from GNS Science and NIWA (Turnbull et al., 2017). The multivariate ENSO index (MEI) is shown as the shaded background in panel (b); (warmer shade indicates El Niño). Further details on data sources and processing are available in the chapter data table (Table 5.SM.6).



Time series of CO₂ concentrations and related measurements in ambient air

Atmospheric Carbon dioxide (CO₂) and Oxygen (O₂)



Airborne fraction and anthropogenic (fossil fuel and land use change) CO₂ emissions

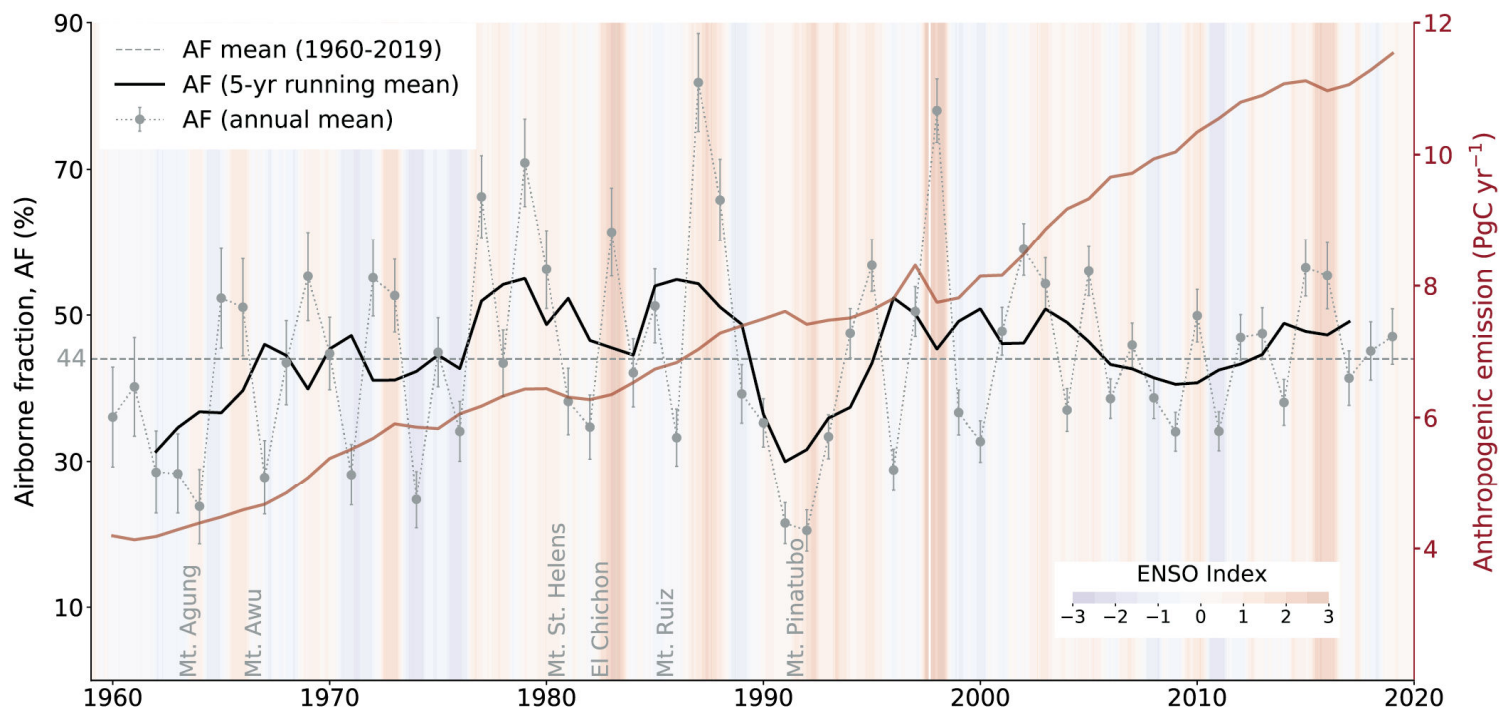
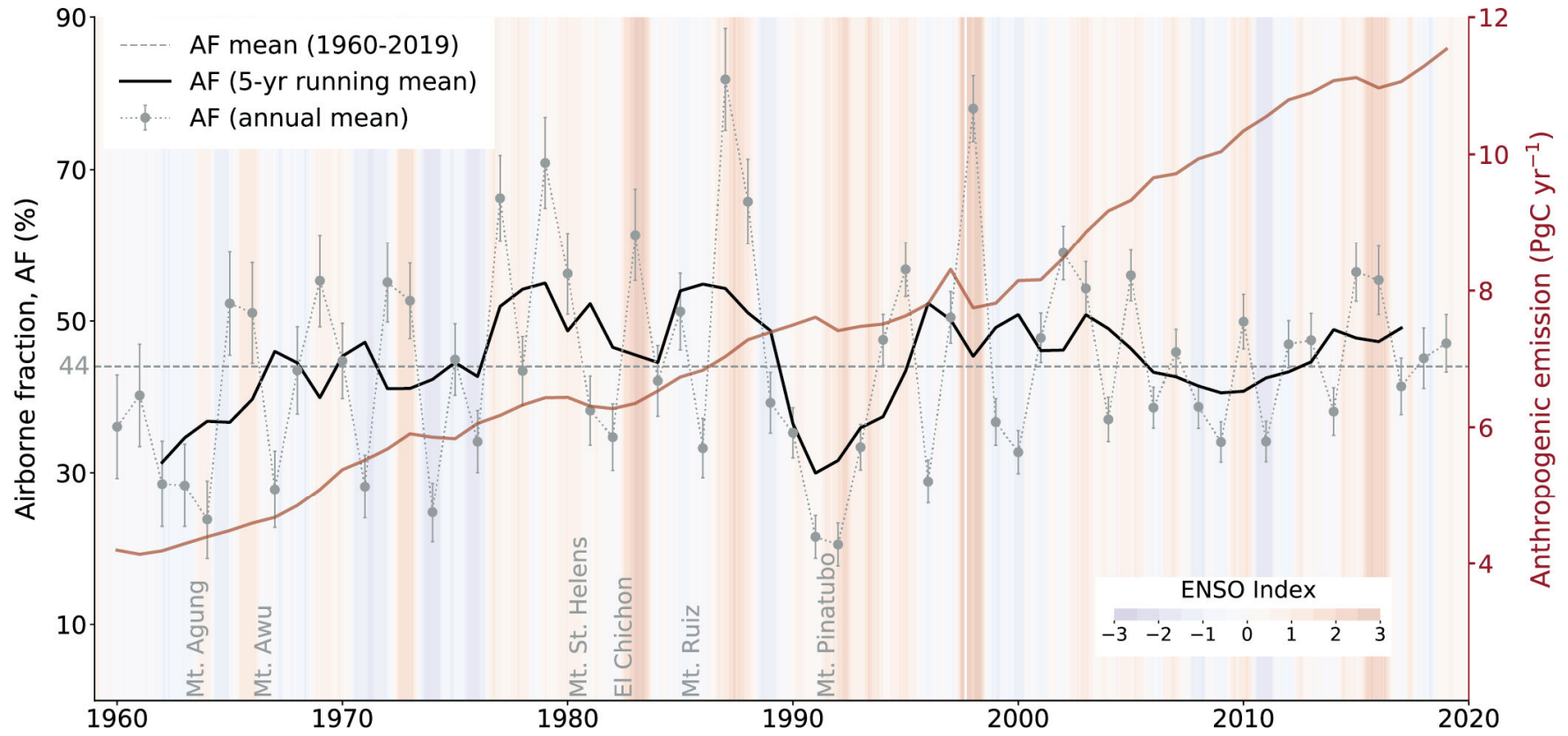


Figure 5.7 | Airborne fraction and anthropogenic (fossil fuel and land-use change) CO₂ emissions. Data as in Section 5.2.1.1. The multivariate El Niño–Southern Oscillation (ENSO) index (shaded) and the major volcanic eruptions are marked along the x-axis. Further details on data sources and processing are available in the chapter data table (Table 5.SM.6).





Statements in the Executive Summary

Contemporary Trends of Greenhouse Gases (4)

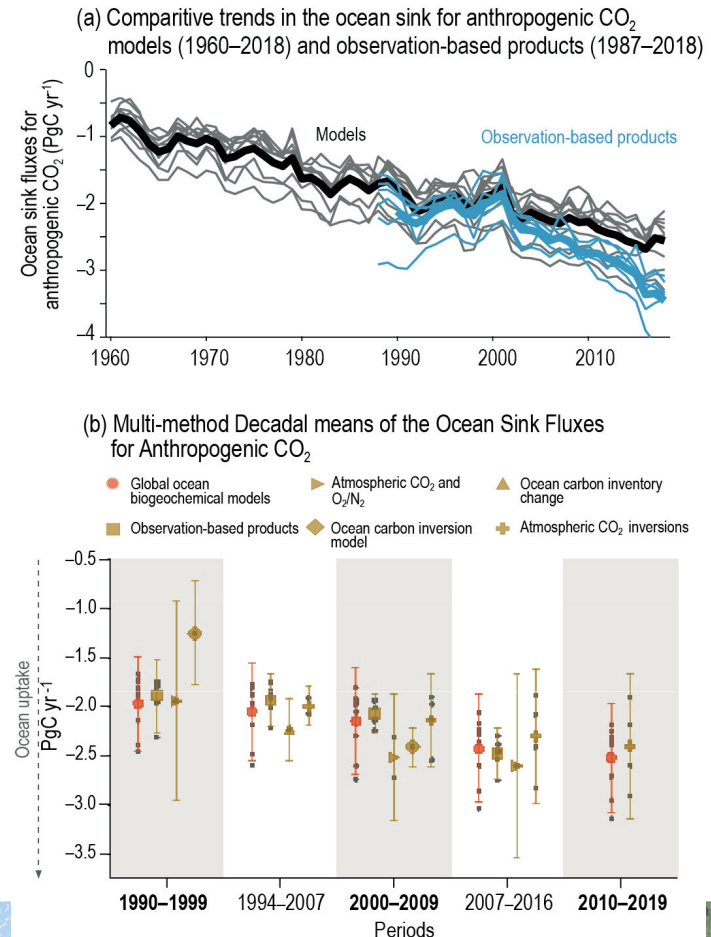
Recent observations show that ocean carbon processes are starting to change in response to the growing ocean sink, and these changes are expected to contribute significantly to future weakening of the ocean sink under medium- to high-emission scenarios. However, the effects of these changes is not yet reflected in a weakening trend of the contemporary (1960–2019) ocean sink (*high confidence*). {5.1.2, 5.2.1.3, 5.3.2.1; Figures 5.8, 5.20; Cross-Chapter Box 5.3}





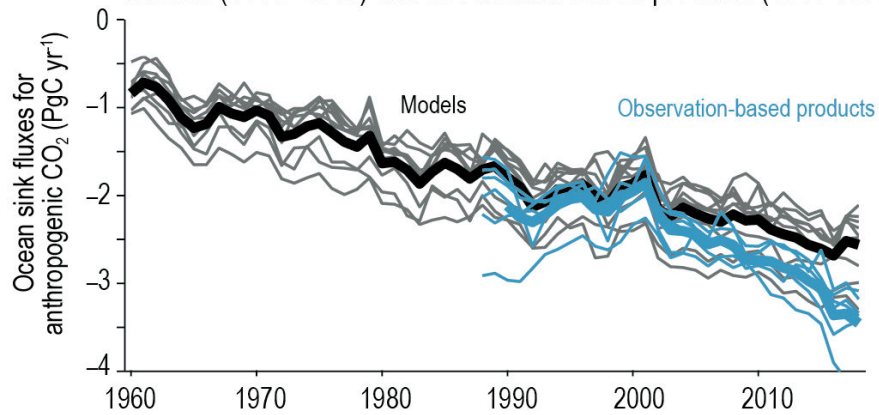
Multi-decadal trends for the ocean sink of CO₂

Figure 5.8 | Multi-decadal trends for the ocean sink of CO₂. (a) The multi-decadal (1960–2019) trends in the annual ocean sink (S_{ocean}) reconstructed from nine Global Ocean Biogeochemical Models (GOBM) forced with atmospheric re-analysis products (Hauck et al., 2020), six observationally based gap-filling products that reconstructed spatial and temporal variability in the ocean CO₂ flux from sparse observations of surface ocean $p\text{CO}_2$ (Supplementary Materials 5.SM.2). The trends in S_{ocean} were calculated from the mean annual GOBM outputs, and the observational products were used to provide confidence in the GOBM assessments ($r^2=0.85$). Thick lines represent the multi-model mean. Observationally based products have been corrected for pre-industrial river carbon fluxes (0.62 PgC yr^{-1}) based on the average of estimates from Jacobson et al. (2007) and Resplandy et al. (2018). (b) Mean decadal constraints and their confidence intervals for global ocean sink (S_{ocean}) of anthropogenic CO₂ using multiple independent or quasi-independent lines of evidence or methods for the period 1990–2019 (see Supplementary Materials Tables 5.SM.1 and 5.SM.2 for magnitudes, uncertainties and published sources). Further details on data sources and processing are available in the chapter data table (Table 5.SM.6).

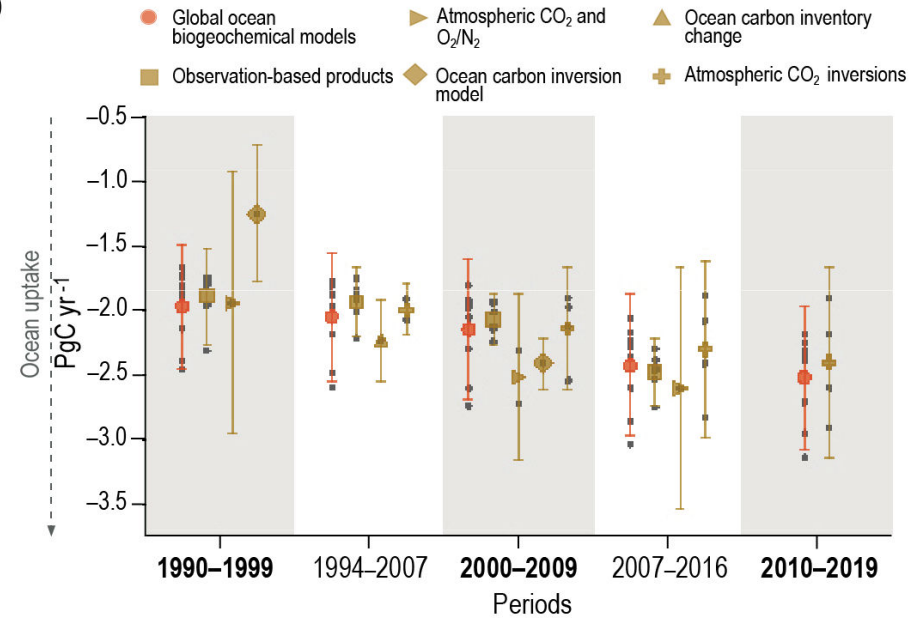


Multi-decadal trends for the ocean sink of CO₂

(a) Comparative trends in the ocean sink for anthropogenic CO₂ models (1960–2018) and observation-based products (1987–2018)

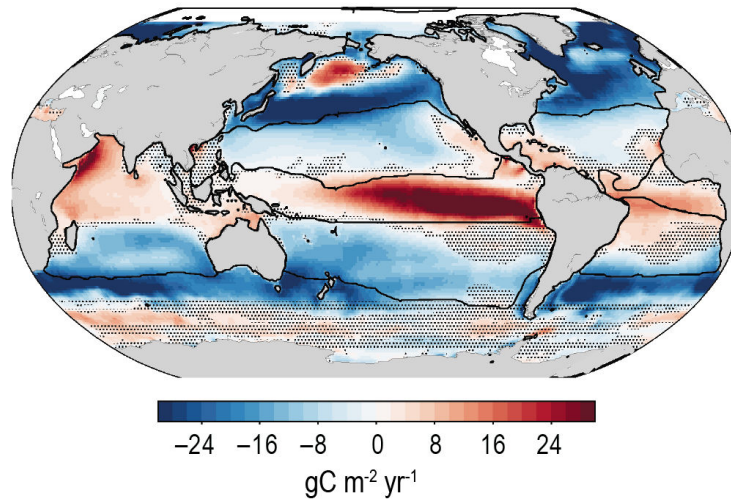


(b) Multi-method Decadal means of the Ocean Sink Fluxes for Anthropogenic CO₂



Regional characteristics of the mean decadal (1994–2007) sea-air CO₂ flux (F_{net}) and ocean storage of anthropogenic CO₂.

(a) Net air–sea flux (F_{net}) of CO₂ (1994–2007)



(b) Rate of change in anthropogenic CO₂ inventory (1994–2007)

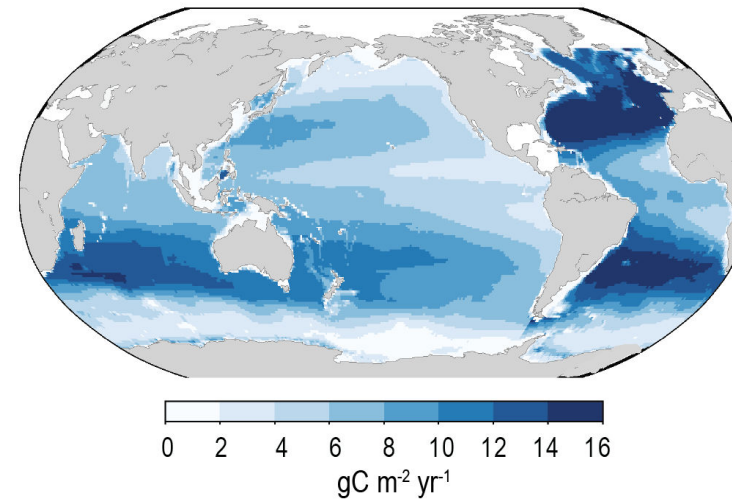
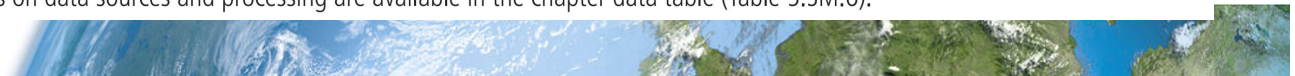


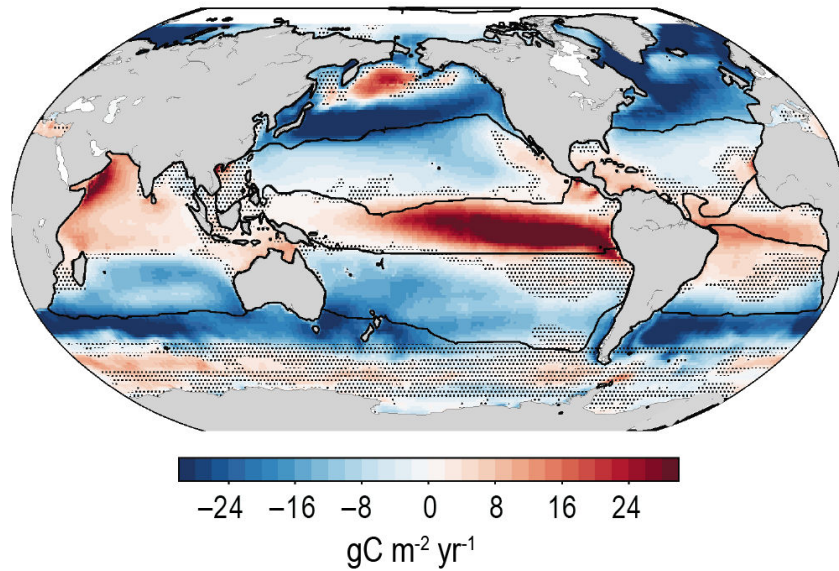
Figure 5.9 | Comparative regional characteristics of the mean decadal (1994–2007) sea-air CO₂ flux (F_{net}) and ocean storage of anthropogenic CO₂.

(a) Regional source–sink characteristics for contemporary ocean air–sea CO₂ fluxes (F_{net}) derived from the ensemble of six observation-based products using Surface Ocean CO₂ Atlas (SOCAT)v6 observational dataset (Landschützer et al., 2014; Rödenbeck et al., 2014; Zeng et al., 2014; Bakker et al., 2016; Denvil-Sommer et al., 2019; Gregor et al., 2019; Iida et al., 2021). Warm colours depict outgassing fluxes and black contours characterize the super-biomes defined from Fay and McKinley (2014) and adjusted by Gregor et al. (2019) also used to calculate the variability in regional flux anomalies (Supplementary Materials Figure 5.SM.1); **(b)** The regional characteristics of the storage fluxes of CO₂ in the ocean interior for the same period (Gruber et al., 2019b). The dots reflect ocean areas where the 1-sigma standard deviation of F_{net} from the six observational-based product reconstructions is larger than the magnitude of the mean. This reflects source–sink transition areas where the mean F_{net} is small and more strongly influenced by spatial and temporal variability across the products. Further details on data sources and processing are available in the chapter data table (Table 5.SM.6).

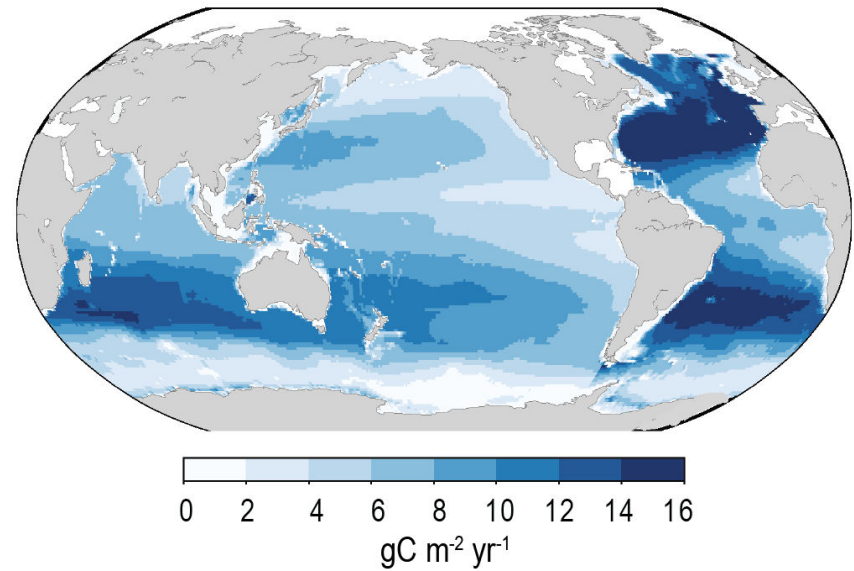


Regional characteristics of the mean decadal (1994–2007) sea-air CO₂ flux (F_{net}) and ocean storage of anthropogenic CO₂.

(a) Net air–sea flux (F_{net}) of CO₂ (1994–2007)

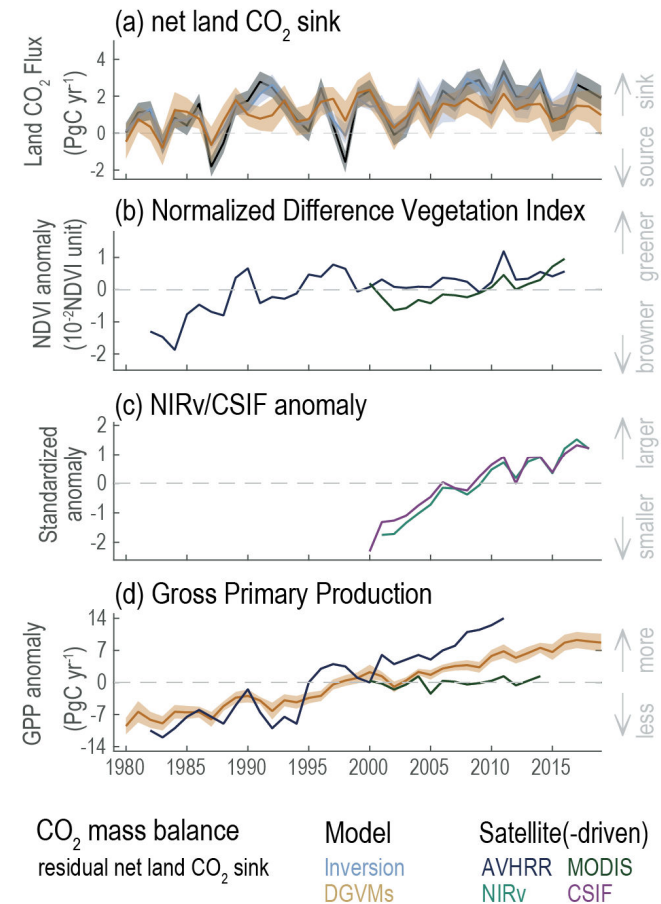


(b) Rate of change in anthropogenic CO₂ inventory (1994–2007)



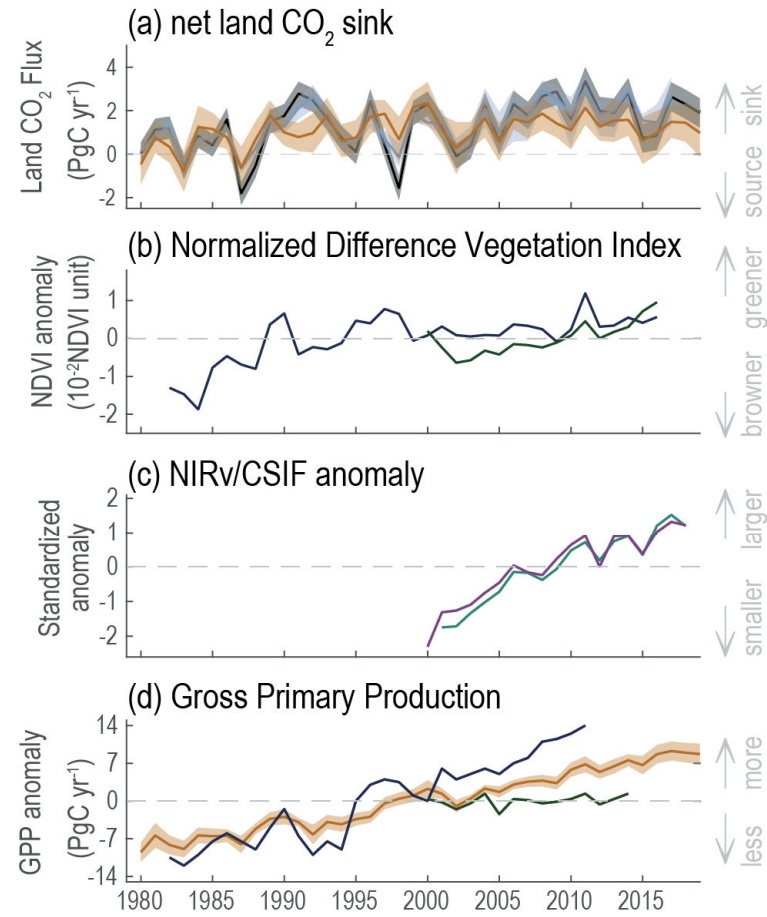
Trends of the net land CO₂ sink and related vegetation observations during 1980–2019

Figure 5.10 | Trends of the net land CO₂ sink and related vegetation observations during 1980–2019. **(a)** Net land CO₂ sink. The residual net land CO₂ sink is estimated from the global CO₂ mass balance (fossil fuel emissions minus atmospheric CO₂ growth rate and ocean CO₂ sink). Inversions indicate the net land CO₂ sink estimated by an ensemble of four atmospheric inversions. Dynamic Global Vegetation Models (DGVMs) indicate the mean net land CO₂ sink estimated by 17 dynamic global vegetation models driven by climate change, rising atmospheric CO₂, land-use change and nitrogen deposition change (for carbon-nitrogen models). The positive values indicate net CO₂ uptake from the atmosphere. **(b)** Normalized difference vegetation index (NDVI). The anomaly of global area-weighted NDVI observed by Advanced Very High Resolution Radiometer (AVHRR) and MODIS satellite sensors. AVHRR data are accessible during 1982–2016 and MODIS data are accessible during 2000–2018. **(c)** Near-infrared reflectance of vegetation (NIRv) and contiguous solar-induced chlorophyll fluorescence (CSIF). The standardized anomaly of area-weighted NIRv during 2001–2018 (Badgley et al., 2017) and CSIF during 2000–2018 (Zhang et al., 2018). **(d)** Gross primary production (GPP). The GPP from Cheng et al. (2017), DGVMs and MODIS GPP product (MOD17A3). GPP from Cheng et al. (2017) is based on an analytical model driven by climate change, rising atmospheric CO₂, AVHRR leaf area index datasets and evapotranspiration datasets. GPP from DGVMs is the ensemble mean global GPP estimated by the same 17 DGVMs that provide the net land CO₂ sink estimates. Shaded area indicates 1- σ inter-model spread except for atmospheric inversions, whose ranges were used due to limited number of models. Further details on data sources and processing are available in the chapter data table (Table 5.SM.6).





Trends of the net land CO₂ sink and related vegetation observations during 1980–2019



CO₂ mass balance
residual net land CO₂ sink

Model
Inversion
DGVMs

Satellite(-driven)
AVHRR MODIS
NIRv CSIF



Global carbon (CO₂) budget (2010-2019)

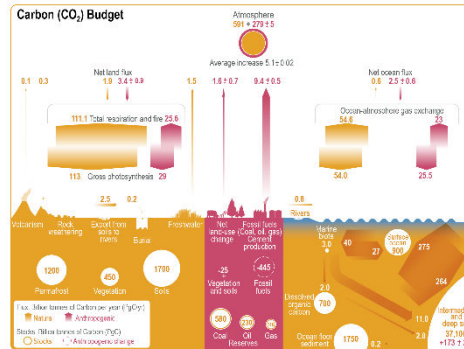
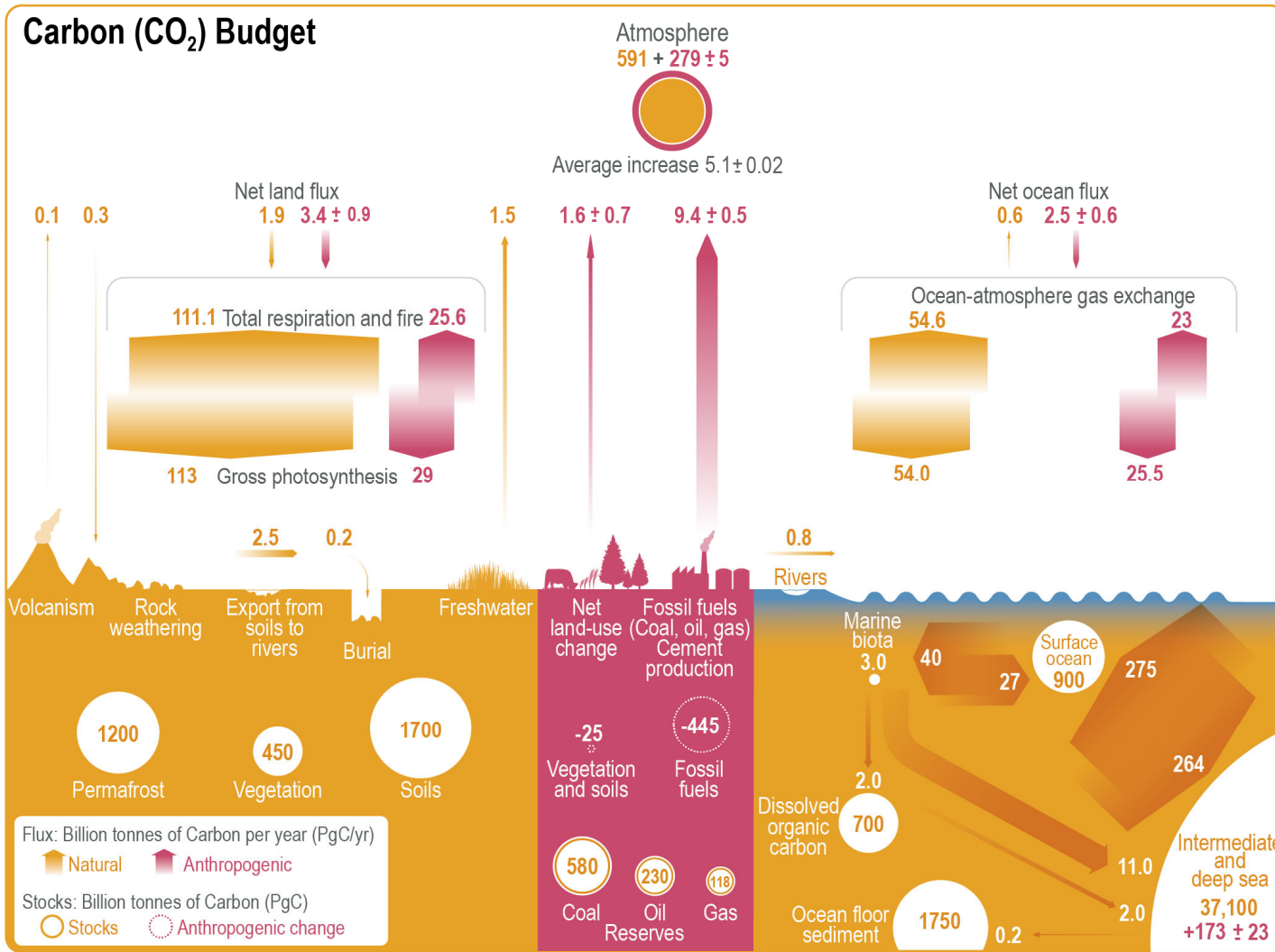


Figure 5.12 | Global carbon (CO₂) budget (2010–2019). Yellow arrows represent annual carbon fluxes (in PgC yr⁻¹) associated with the natural carbon cycle, estimated for the time prior to the industrial era, around 1750. Pink arrows represent anthropogenic fluxes averaged over the period 2010–2019. The rate of carbon accumulation in the atmosphere is equal to net land-use change emissions, including land management (called LULUCF in the main text) plus fossil fuel emissions, minus land and ocean net sinks (plus a small budget imbalance, Table 5.1). Circles with yellow numbers represent pre-industrial carbon stocks in PgC. Circles with pink numbers represent anthropogenic changes to these stocks (cumulative anthropogenic fluxes) since 1750. Anthropogenic net fluxes are reproduced from Friedlingstein et al. (2020). The relative change of gross photosynthesis since pre-industrial times is based on 15 DGVMs used in Friedlingstein et al. (2020). The corresponding emissions by total respiration and fire are those required to match the net land flux, exclusive of net land-use change emissions which are accounted for separately. The cumulative change of anthropogenic carbon in the terrestrial reservoir is the sum of carbon cumulatively lost by net land-use change emissions, and net carbon accumulated since 1750 in response to environmental drivers (warming, rising CO₂, nitrogen deposition). The adjusted gross natural ocean–atmosphere CO₂ flux was derived by rescaling the value in Figure 1 of Sarmiento and Gruber (2002) of 70 PgC yr⁻¹ by the revised estimate of the bomb radiocarbon (¹⁴C) inventory in the ocean. The original bomb ¹⁴C inventory yielded an average global gas transfer velocity of 22 cm hr⁻¹; the revised estimate is 17 cm hr⁻¹ leading to 17/22*70=54. Dissolved organic carbon reservoir and fluxes from Hansell et al. (2009). Dissolved inorganic carbon exchanges between surface and deep ocean, subduction and obduction from Levy et al. (2013). Export production and flux from (Boyd et al., 2019). Net primary production (NPP) and remineralization in surface layer of the ocean from Kwiatkowski et al. (2020); Séférian et al. (2020). Deep ocean reservoir from Keppler et al. (2020). Anthropogenic carbon reservoir in the ocean is from Gruber et al. (2019b) extrapolated to 2015. Fossil fuel reserves are from BGR (2020); fossil fuel resources are 11,490 PgC for coal, 6,780 PgC for oil and 365 PgC for natural gas. Permafrost region stores are from Hugelius et al. (2014); Strauss et al. (2017); Mishra et al. (2021) (see also Box 5.1) and soil carbon stocks outside of permafrost region from Batjes (2016); Jackson et al. (2017). Biomass stocks (range of seven estimates) are from Erb et al. (2018). Sources for the fluxes of the land–ocean continuum are provided in main text and adjusted within the ranges of the various assessment to balance the budget (Section 5.2.1.5).



Statements in the Executive Summary

Contemporary Trends of Greenhouse Gases (4)

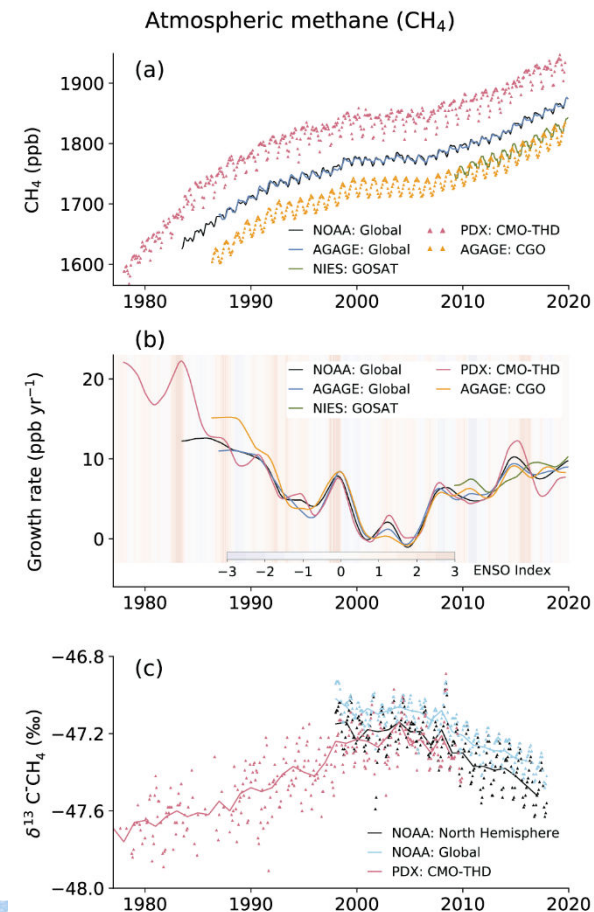
Recent observations show that ocean carbon processes are starting to change in response to the growing ocean sink, and these changes are expected to contribute significantly to future weakening of the ocean sink under medium- to high-emission scenarios. However, the effects of these changes is not yet reflected in a weakening trend of the contemporary (1960–2019) ocean sink (*high confidence*). {5.1.2, 5.2.1.3, 5.3.2.1; Figures 5.8, 5.20; Cross-Chapter Box 5.3}

Atmospheric concentration of CH₄ grew at an average rate of 7.6 ± 2.7 ppb yr⁻¹ for the last decade (2010–2019), with a faster growth of 9.3 ± 2.4 ppb yr⁻¹ over the last six years (2014–2019) (*high confidence*). The multi-decadal growth trend in atmospheric CH₄ is dominated by anthropogenic activities (*high confidence*), and the growth since 2007 is largely driven by emissions from both fossil fuels and agriculture (dominated by livestock) sectors (*medium confidence*). The interannual variability is dominated by El Niño–Southern Oscillation cycles, during which biomass burning and wetland emissions, as well as loss by reaction with tropospheric hydroxyl radical OH play an important role. {5.2.2; Figures 5.13, 5.14; Table 5.2; Cross-Chapter Box 5.2}



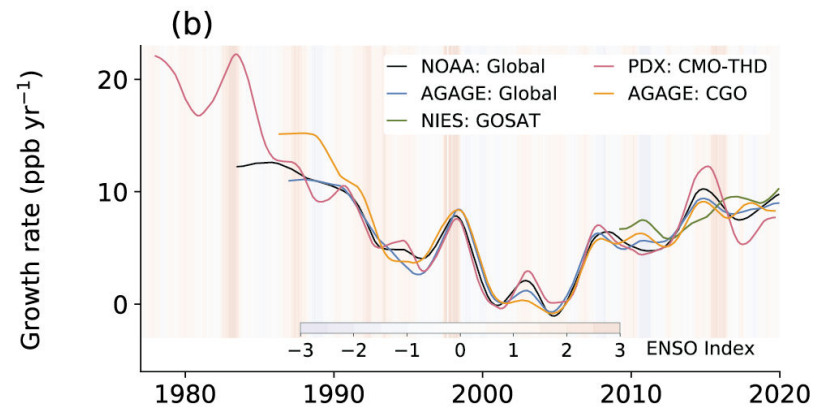
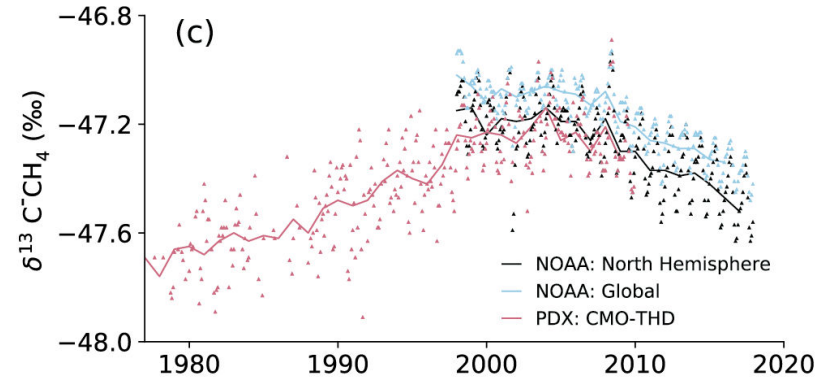
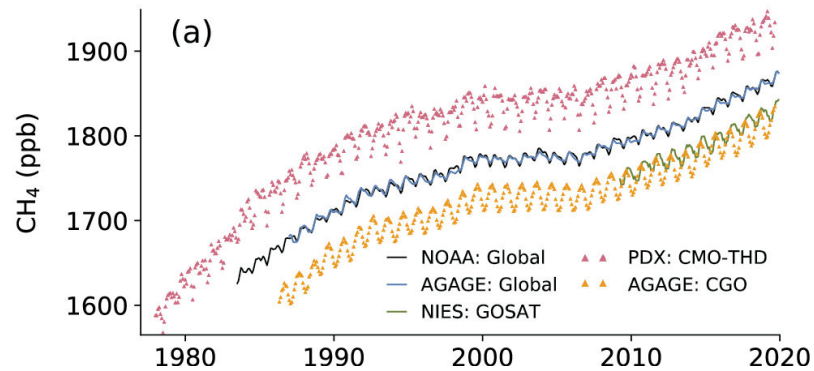
Time series of CH₄ concentrations, growth rates and isotopic composition

Figure 5.13 | Time series of CH₄ concentrations, growth rates and isotopic composition. (a) CH₄ concentrations; (b) CH₄ growth rates; (c) d¹³-CH₄. Data from selected site networks operated by the National Oceanic and Atmospheric Administration (NOAA; Dlugokencky et al., 2003), Advanced Global Atmospheric Gases Experiment (AGAGE; Prinn et al., 2018) and Portland Airport (PDX, Portland State University; Rice et al., 2016). To maintain clarity, data from many other measurement networks are not included here, and all measurements are shown in the World Meteorological Organization X2004ACH₄ global calibration standard. Global mean values of XCH₄ (total-column), retrieved from radiation spectra measured by the Greenhouse Gases Observing Satellite (GOSAT) are shown in panels (a) and (b). Cape Grim Observatory (CGO; 41°S, 145°E) and Trinidad Head (THD; 41°N, 124°W) data are taken from the AGAGE network. NOAA global and northern hemispheric (NH) means for d¹³C are calculated from 10 and 6 sites, respectively. The PDX data adjusted to NH (period: 1977–2000) are merged with THD (period: 2001–2019) for CH₄ concentration and growth rate analysis, and PDX and NOAA NH means of d¹³C data are used for joint interpretation of long-term trends analysis. The multivariate El Niño–Southern Oscillation (ENSO) index (MEI) is shown in panel (b). Further details on data sources and processing are available in the chapter data table (Table 5.SM.6).



Time series of CH₄ concentrations, growth rates and isotopic composition

Atmospheric methane (CH₄)



$$\delta^{13}\text{C} = \left(\frac{\left(\frac{^{13}\text{C}}{^{12}\text{C}}\right)_{\text{Probe}}}{\left(\frac{^{13}\text{C}}{^{12}\text{C}}\right)_{\text{Standard}}} - 1 \right) \cdot 1000 \text{ ‰}$$



Global methane (CH₄) budget (2008–2017)

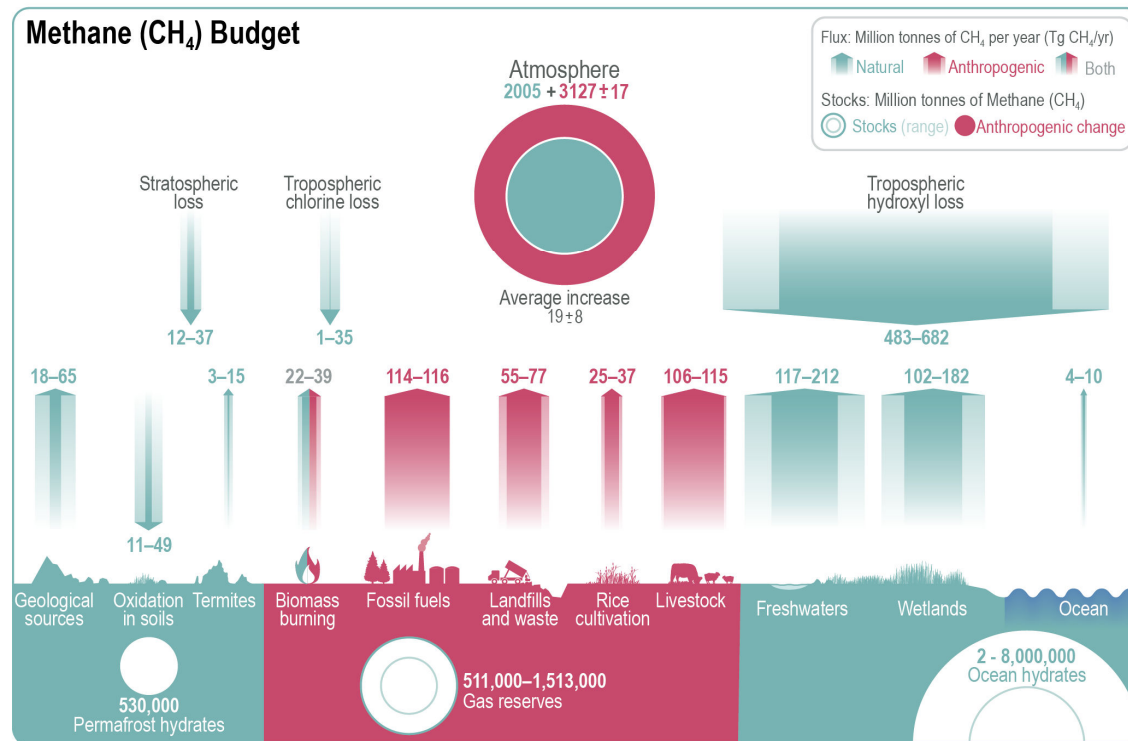
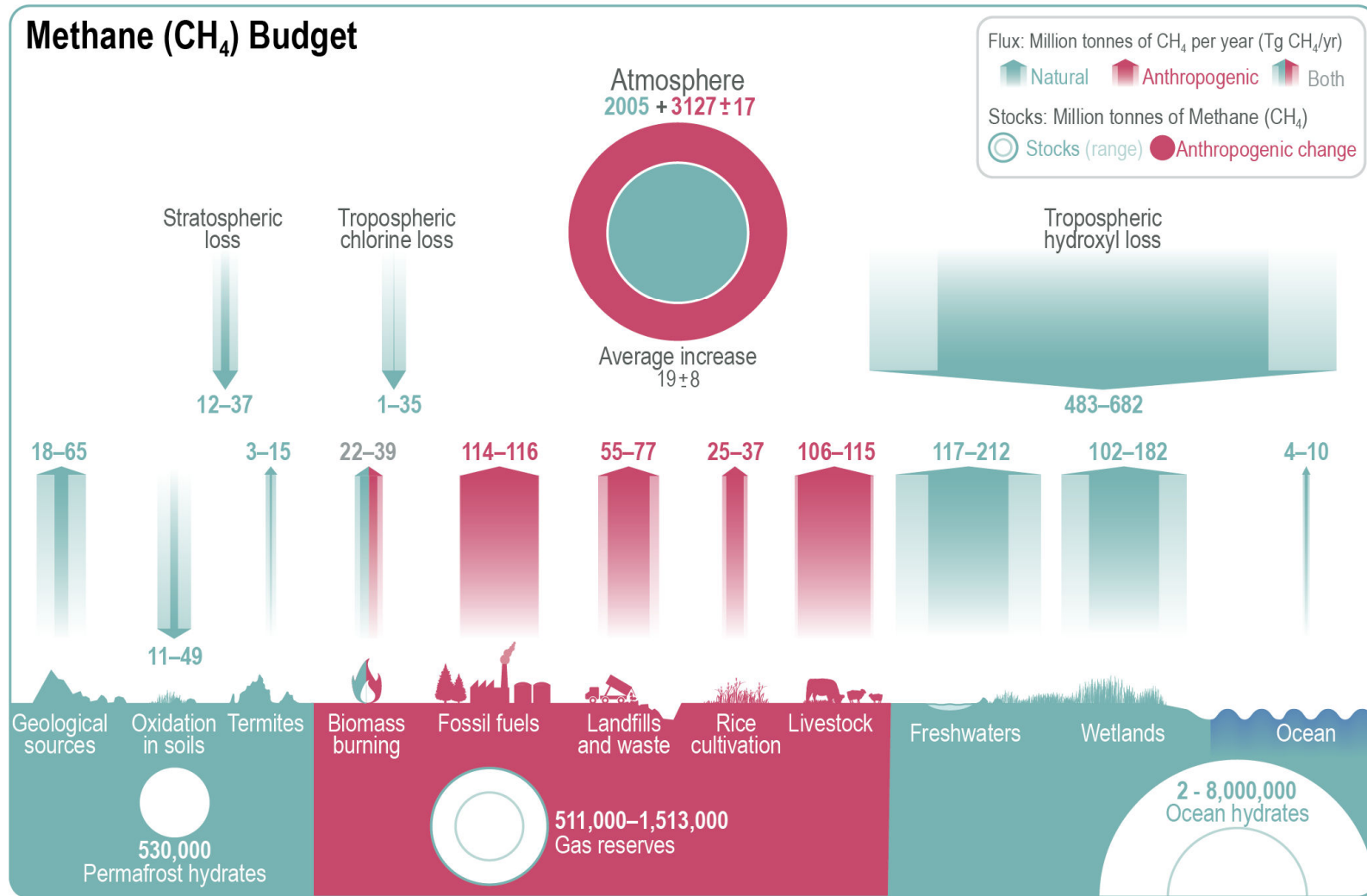


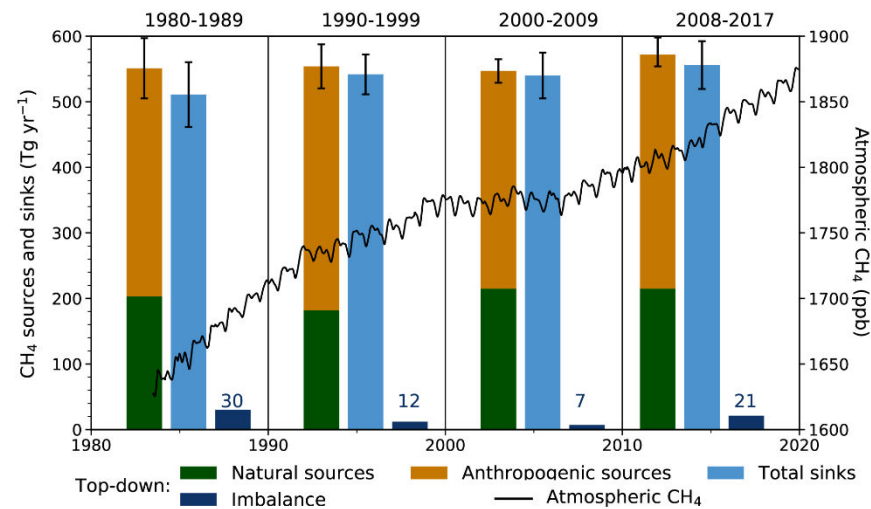
Figure 5.14 | Global methane (CH₄) budget (2008–2017). Values and data sources as in Table 5.2 (in TgCH₄). The atmospheric stock is calculated from mean CH₄ concentration, multiplying a factor of 2.75 ± 0.015 Tg ppb⁻¹, which accounts for the uncertainties in global mean CH₄ (Chandra et al., 2021). Further details on data sources and processing are available in the chapter data table (Table 5.SM.6).



Methane (CH₄) Budget

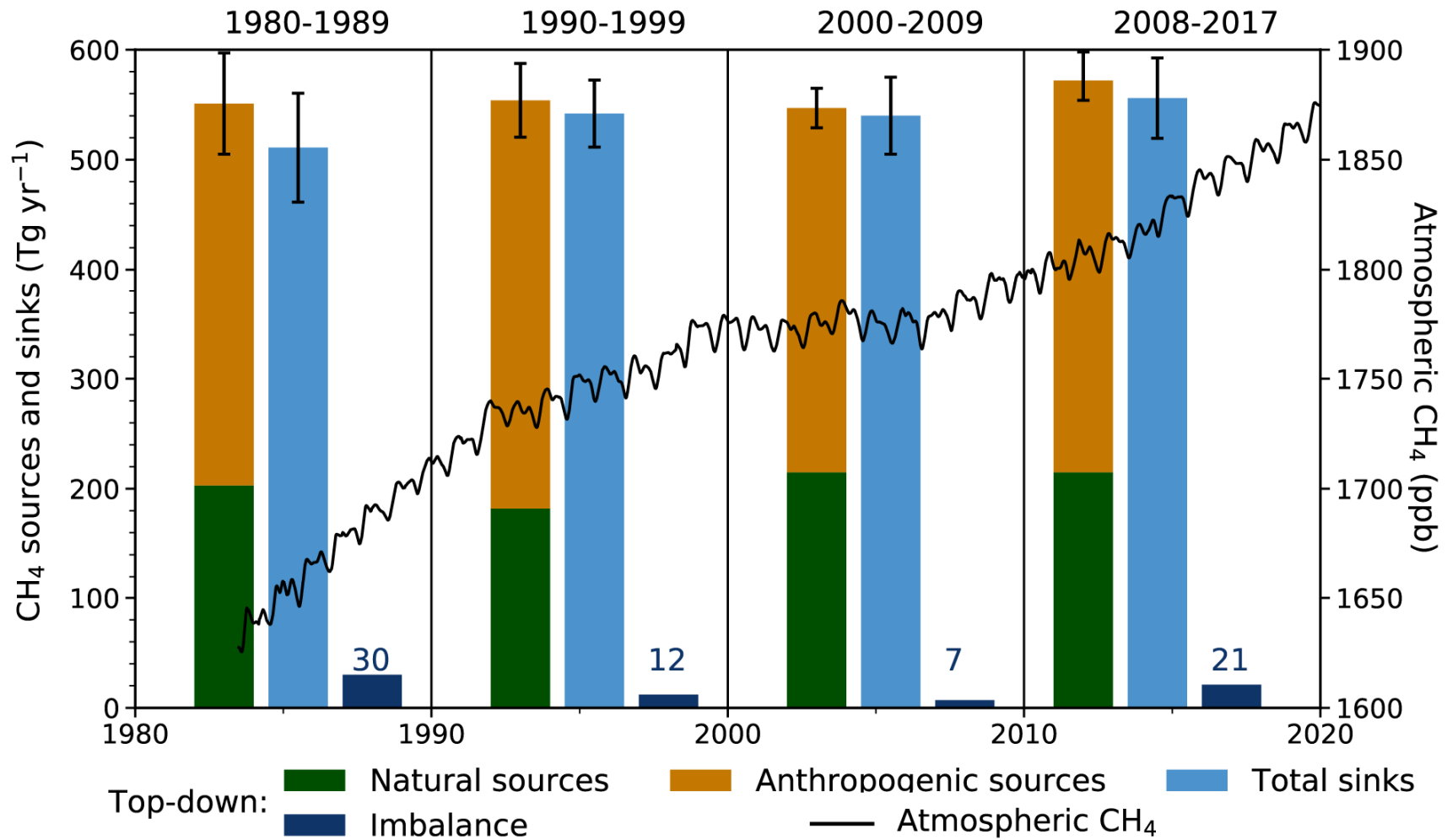


Methane sources and sinks for four decades from atmospheric inversions with the budget imbalance

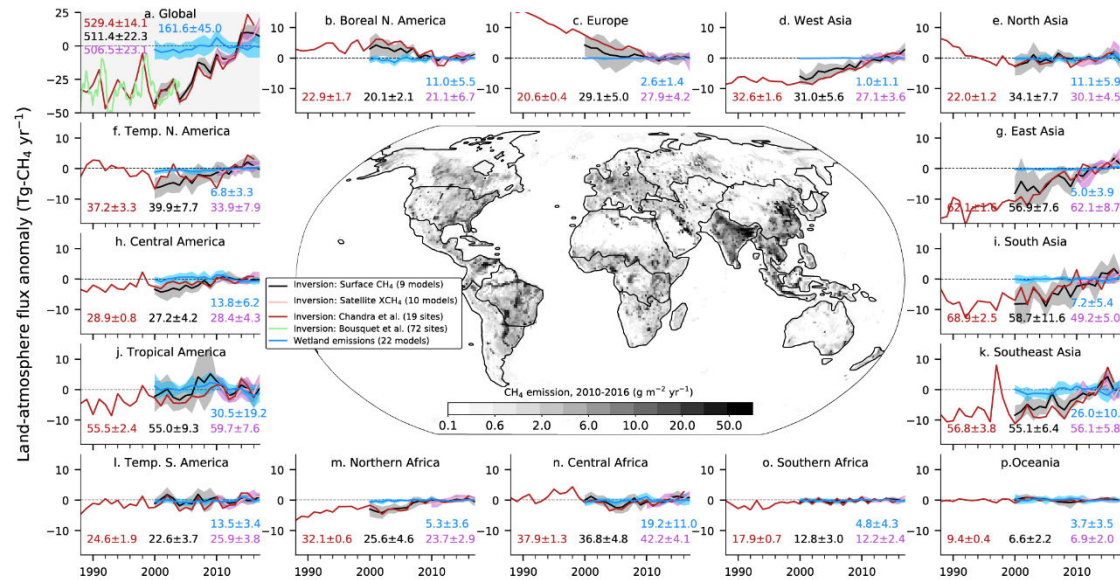


Cross-Chapter Box 5.2, Figure 1 | Methane sources and sinks for four decades from atmospheric inversions with the budget imbalance (source–sink; dark blue bars) (plotted on the left y-axis). Top-down analysis from Kirschke et al. (2013); Saunio et al. (2020). The global CH₄ concentration seen in the black line (plotted on the right y-axis), representing National Oceanic and Atmospheric Administration (NOAA) observed global monthly mean atmospheric CH₄ in dry-air mole fractions for 1983–2019 (Chapter 2, Annex V). Natural sources include emissions from natural wetlands, lakes and rivers, geological sources, wild animals, termites, wildfires, permafrost soils, and oceans. Anthropogenic sources include emissions from enteric fermentation and manure, landfills, waste and wastewater, rice cultivation, coal mining, oil and gas industry, biomass and biofuel burning. The top-down total sink is determined from global mass balance that includes chemical losses due to reactions with hydroxyl (OH), atomic chlorine (Cl), and excited atomic oxygen (O¹D), and oxidation by bacteria in aerobic soils (Table 5.2). Further details on data sources and processing are available in the chapter data table (Table 5.SM.6).



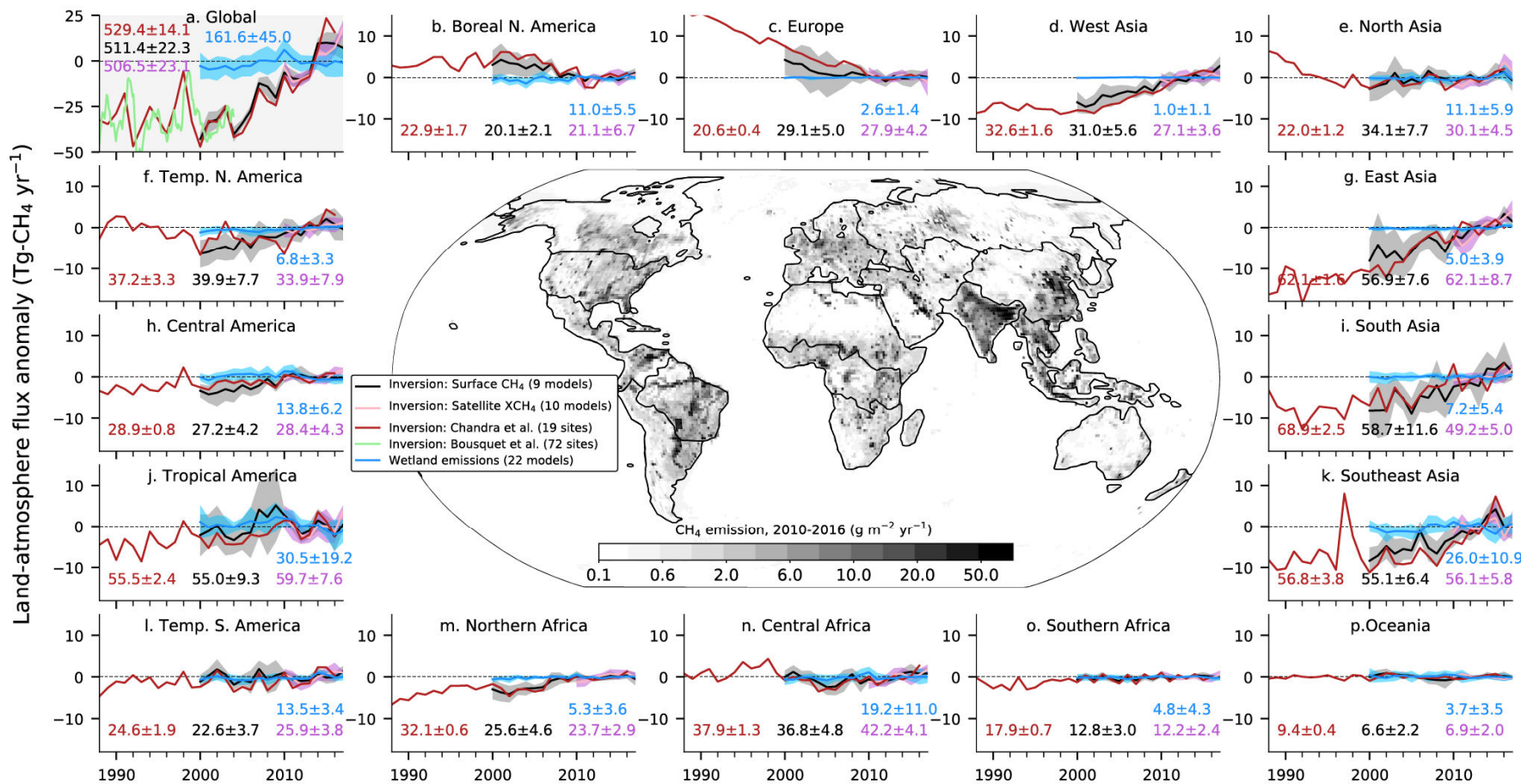


Anomalies in global and regional methane (CH₄) emissions for 1988–2017



Cross-Chapter Box 5.2, Figure 2 | Anomalies in global and regional methane (CH₄) emissions for 1988–2017. The map in the centre shows mean CH₄ emissions for 2010–2016. Multi-model mean (line) and 1-s standard deviations (shaded) for 2000–2017 are shown for 9 surface CH₄ and 10 satellite XCH₄ inversions, and 22 wetland models or model variants that participated in GCP-CH₄ budget assessment (Saunois et al., 2020). The results for the period before 2000 are available from two inversions, one using 19 sites (Chandra et al., 2021; also used for the 2010–2016 mean emissions map) and one for global totals (Bousquet et al., 2006). The long-term mean values for 2010–2016 (common for all GCP-CH₄ inversions), as indicated within each panel separately, are subtracted from the annual-mean time series for the calculation of anomalies for each region. Further details on data sources and processing are available in the chapter data table (Table 5.SM.6).





Statements in the Executive Summary

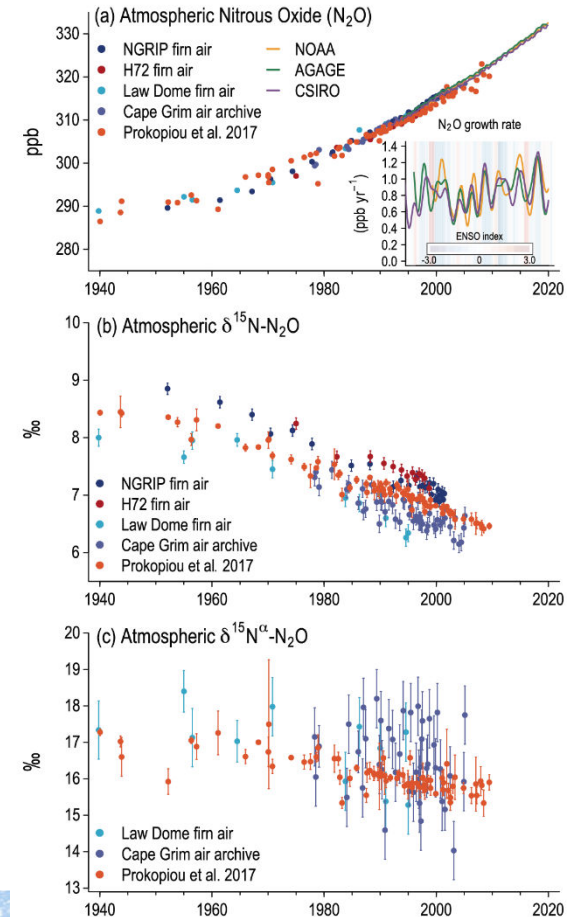
Contemporary Trends of Greenhouse Gases (5)

Atmospheric concentration of N₂O grew at an average rate of 0.85 ± 0.03 ppb yr⁻¹ between 1995 and 2019, with a further increase to 0.95 ± 0.04 ppb yr⁻¹ in the most recent decade (2010–2019). This increase is dominated by anthropogenic emissions, which have increased by 30% between the 1980s and the most recent observational decade (2007–2016) (*high confidence*). Increased use of nitrogen fertilizer and manure contributed to about two-thirds of the increase during the 1980–2016 period, with the fossil fuels/industry, biomass burning, and wastewater accounting for much of the rest (*high confidence*). {5.2.3; Figures 5.15, 5.16, 5.17}

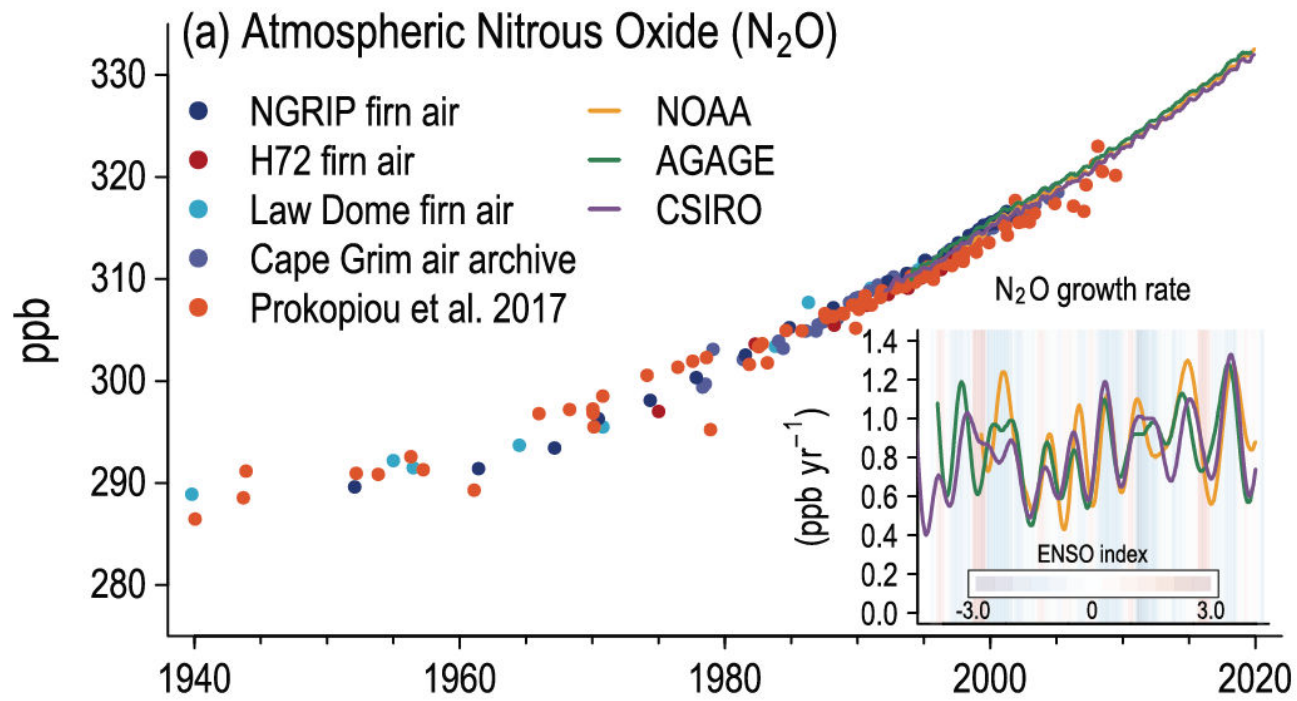


Changes in atmospheric nitrous oxide (N₂O)

Figure 5.15 | Changes in atmospheric nitrous oxide (N₂O) and its isotopic composition since 1940. (a) Atmospheric N₂O abundance (parts per billion, ppb) and growth rate (ppb yr⁻¹); (b) δ¹⁵N of atmospheric N₂O; and (c) alpha-site ¹⁵N–N₂O. Estimates are based on direct atmospheric measurements in the Advanced Global Atmospheric Gases Experiment (AGAGE), Commonwealth Scientific and Industrial Research Organisation (CSIRO), and National Oceanic and Atmospheric Administration (NOAA) networks (Prinn et al., 2000, 2018; Francey et al., 2003; Hall et al., 2007; Elkins et al., 2018), archived air samples from Cape Grim, Australia (Park et al., 2012), and firn air from the North Greenland Ice Core Project (NGRIP) Greenland and H72 Antarctica (Ishijima et al., 2007), Law Dome Antarctica (Park et al., 2012), as well as a collection of firn ice samples from Greenland (Prokopiou et al., 2017, 2018). Shading in (a) is based on the multivariate El Niño–Southern Oscillation (ENSO) index, with red indicating El Niño conditions (Wolter and Timlin, 1998). Further details on data sources and processing are available in the chapter data table (Table 5.SM.6).



Changes in atmospheric nitrous oxide (N₂O)



Decadal mean nitrous oxide (N₂O) emissions for 2007–2016 and its change since 1850 based on process-model projections.

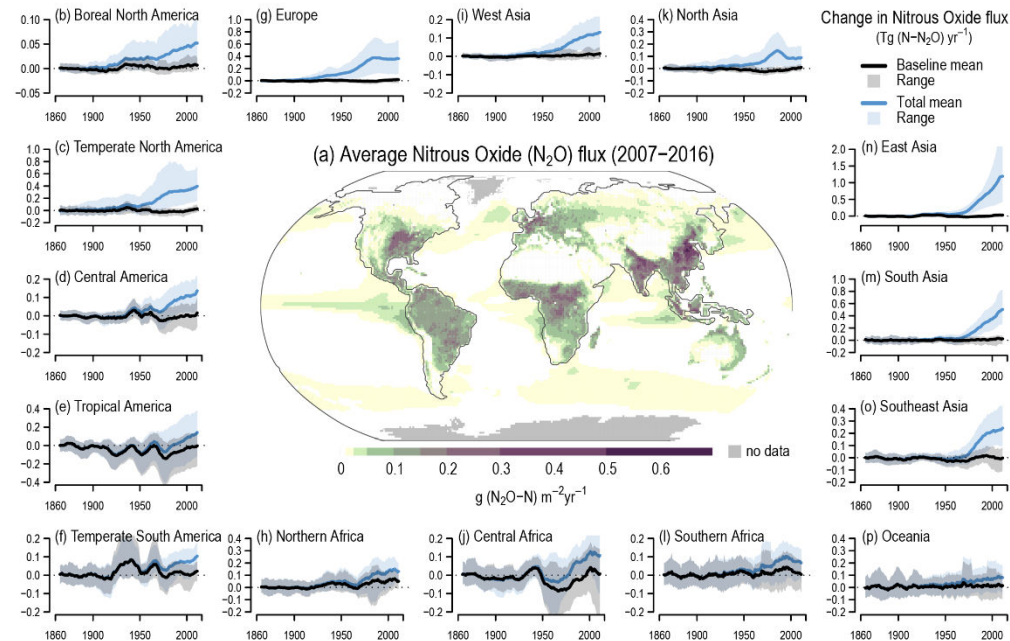
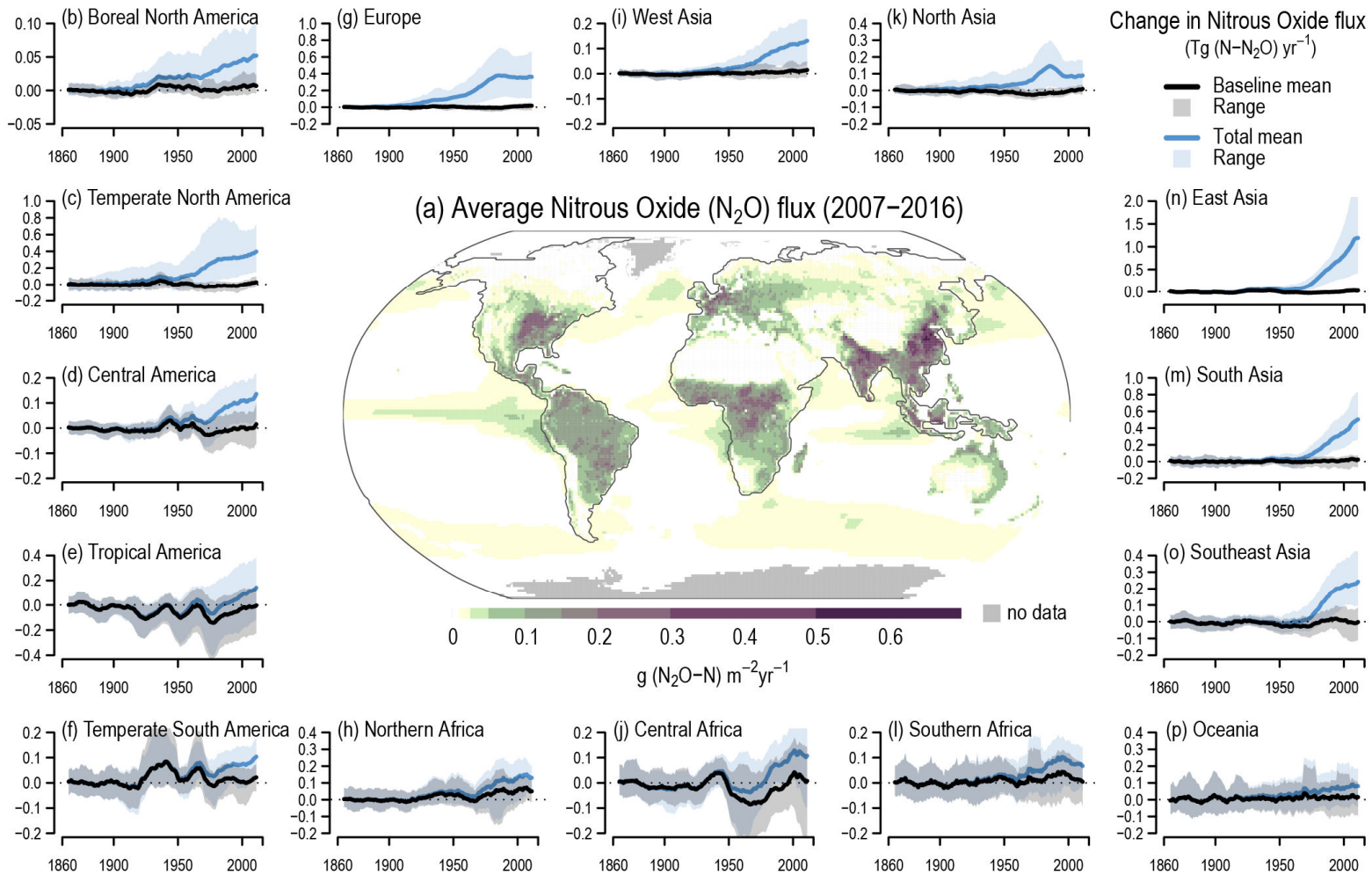


Figure 5.16 | Decadal mean nitrous oxide (N₂O) emissions for 2007–2016 and its change since 1850 based on process-model projections. The total effect, including that from anthropogenic nitrogen additions (atmospheric deposition, manure addition, fertilizer use and land-use), is evaluated against the background flux driven by changes in atmospheric carbon dioxide (CO₂) concentration, and climate change. Fluxes are derived from the N₂O model intercomparison project ensemble of terrestrial biosphere models (Tian et al., 2019) and three ocean biogeochemical models (Landolfi et al., 2017; Battaglia and Joos, 2018a; Buitenhuis et al., 2018). Further details on data sources and processing are available in the chapter data table (Table 5.SM.6).





Global nitrous oxide (N₂O) budget (2007–2016)

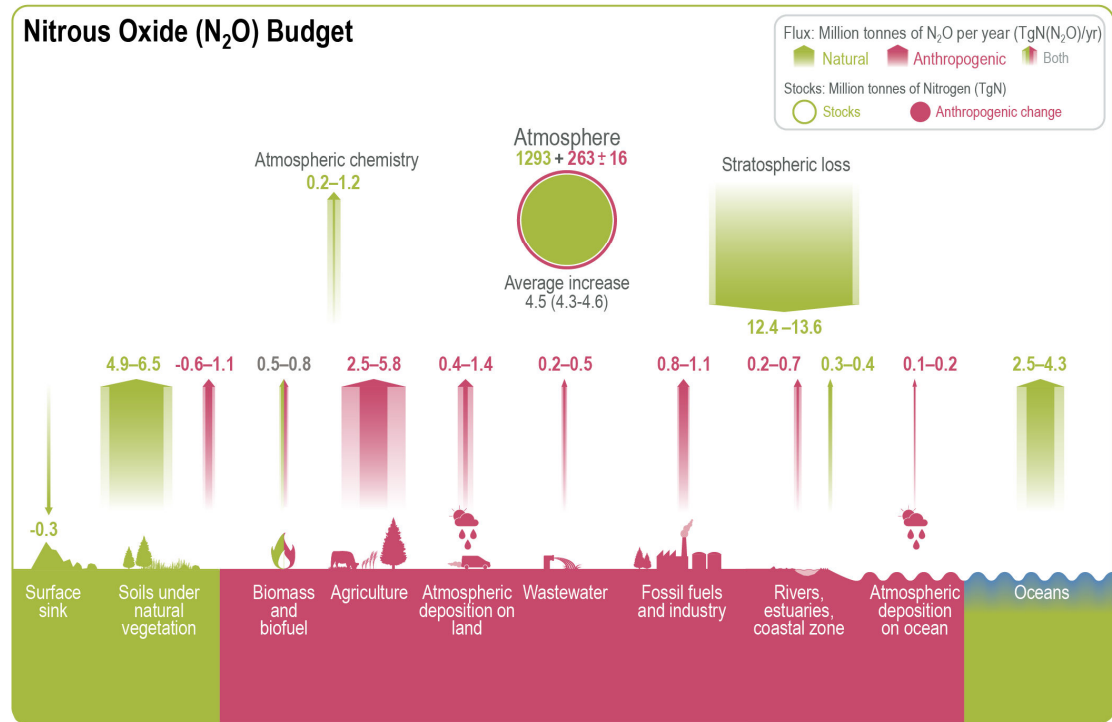
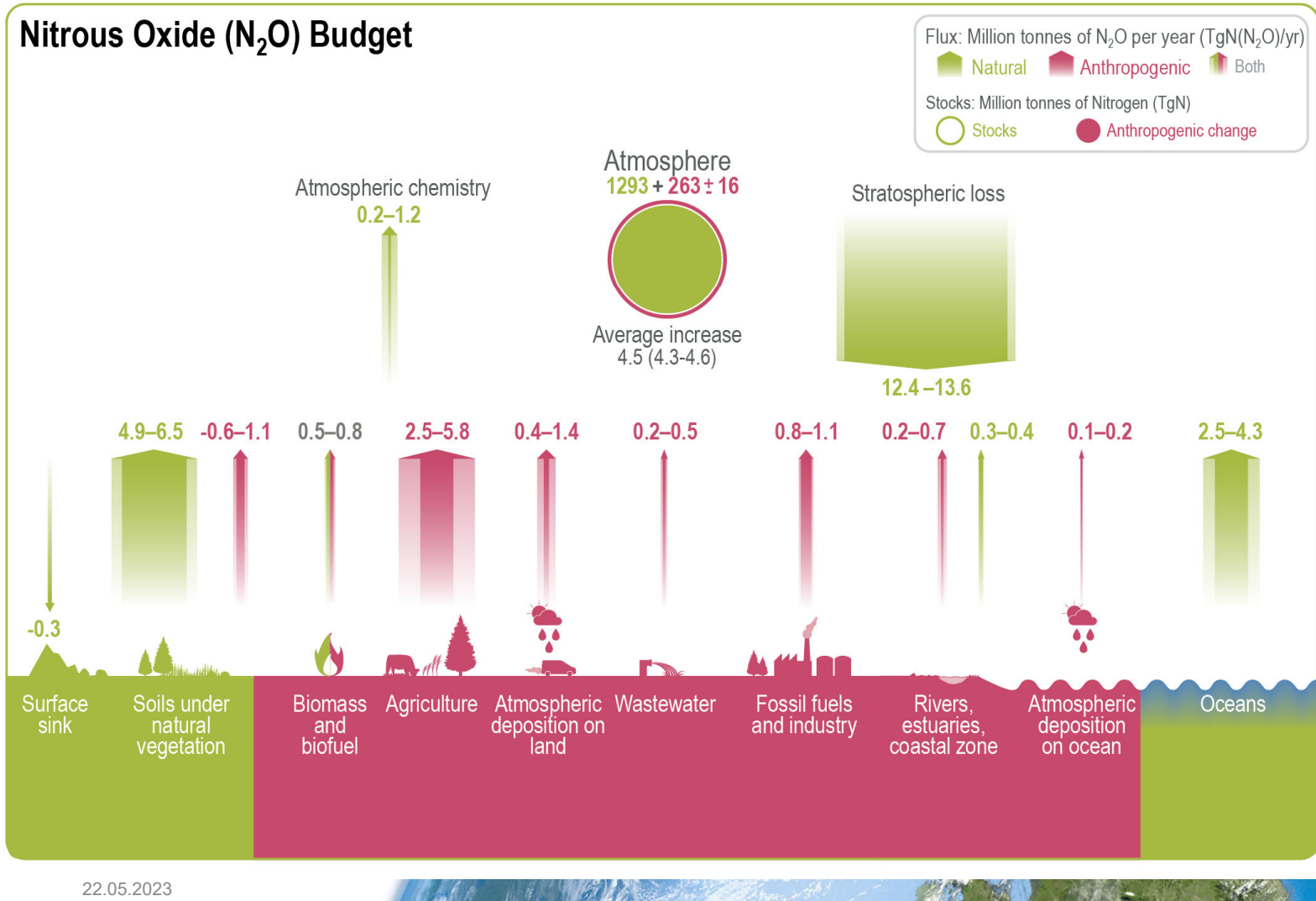


Figure 5.17 | Global nitrous oxide (N₂O) budget (2007–2016). Values and data sources as in Table 5.3. The atmospheric stock is calculated from mean N₂O concentration, multiplying a factor of $4.79 \pm 0.05 \text{ Tg ppb}^{-1}$ (Prather et al., 2012). Pool sizes for the other reservoirs are largely unknown. Further details on data sources and processing are available in the chapter data table (Table 5.SM.6).





22.05.2023



Contributions of carbon dioxide (CO₂), methane (CH₄), nitrous oxide (N₂O) and halogenated species to the total effective radiative forcing (ERF) increase since 1850 and 1960, and for 2000 to 2009

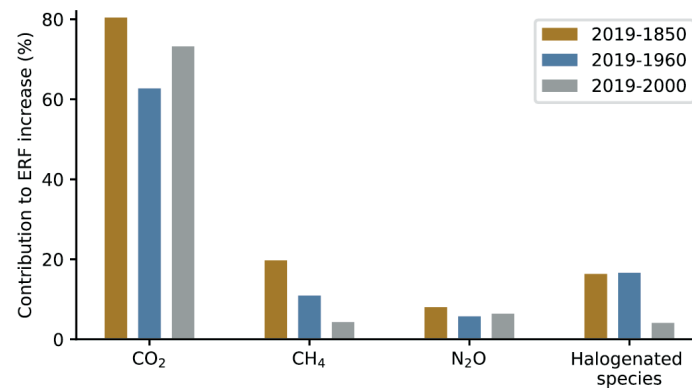
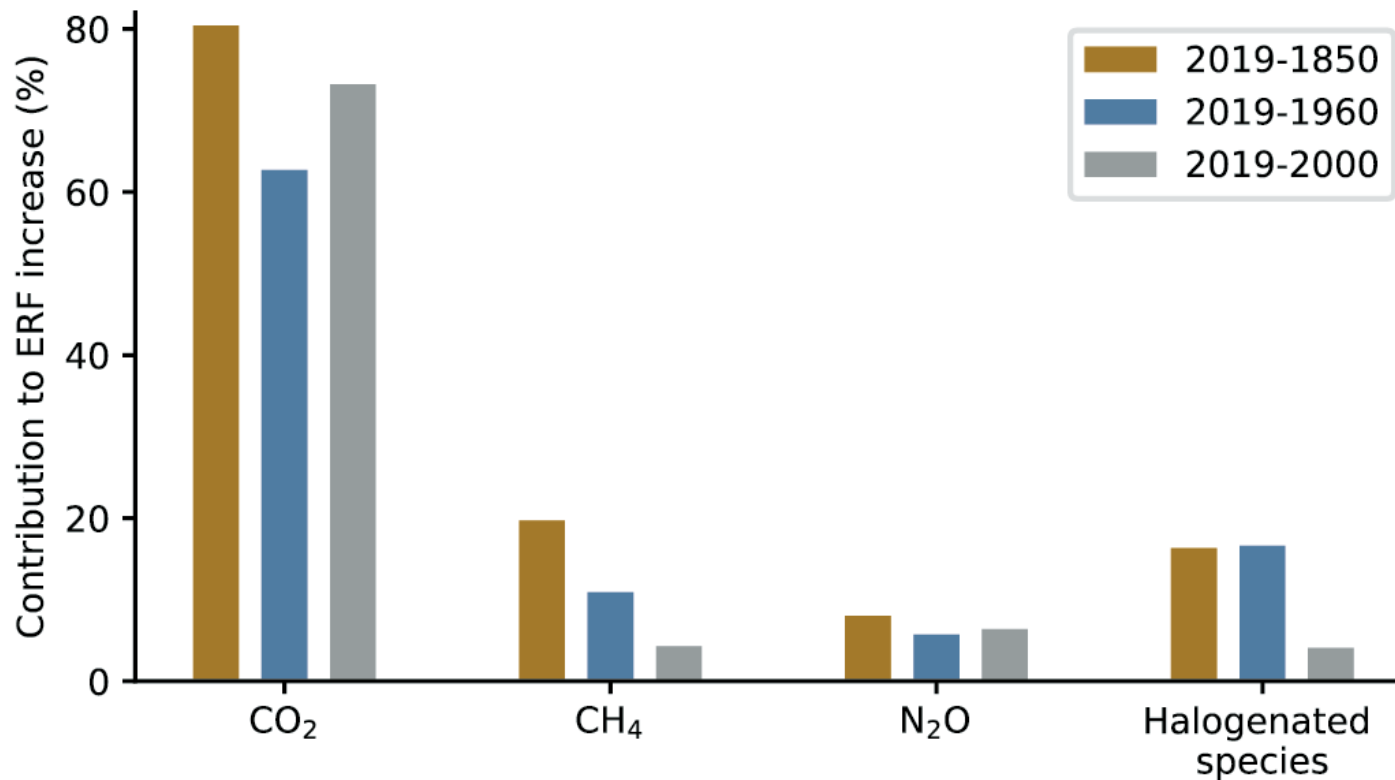


Figure 5.18 | Contributions of carbon dioxide (CO₂), methane (CH₄), nitrous oxide (N₂O) and halogenated species to the total effective radiative forcing (ERF) increases in 2019 since 1850, 1960 and 2000, respectively. ERF data are taken from Annex III (based on calculations from Chapter 7). Note that the sum of the ERFs exceeds 100% because there are negative ERFs due to aerosols and clouds. Further details on data sources and processing are available in the chapter data table (Table 5.SM.6).



Contributions of carbon dioxide (CO₂), methane (CH₄), nitrous oxide (N₂O) and halogenated species to the total effective radiative forcing (ERF) increase since 1850 and 1960, and for 2000 to 2009



Regional distributions of net fluxes of carbon dioxide (CO₂), methane (CH₄), nitrous oxide (N₂O) on the Earth's surface

Regional distributions of CO₂, CH₄ and N₂O fluxes by inverse modelling

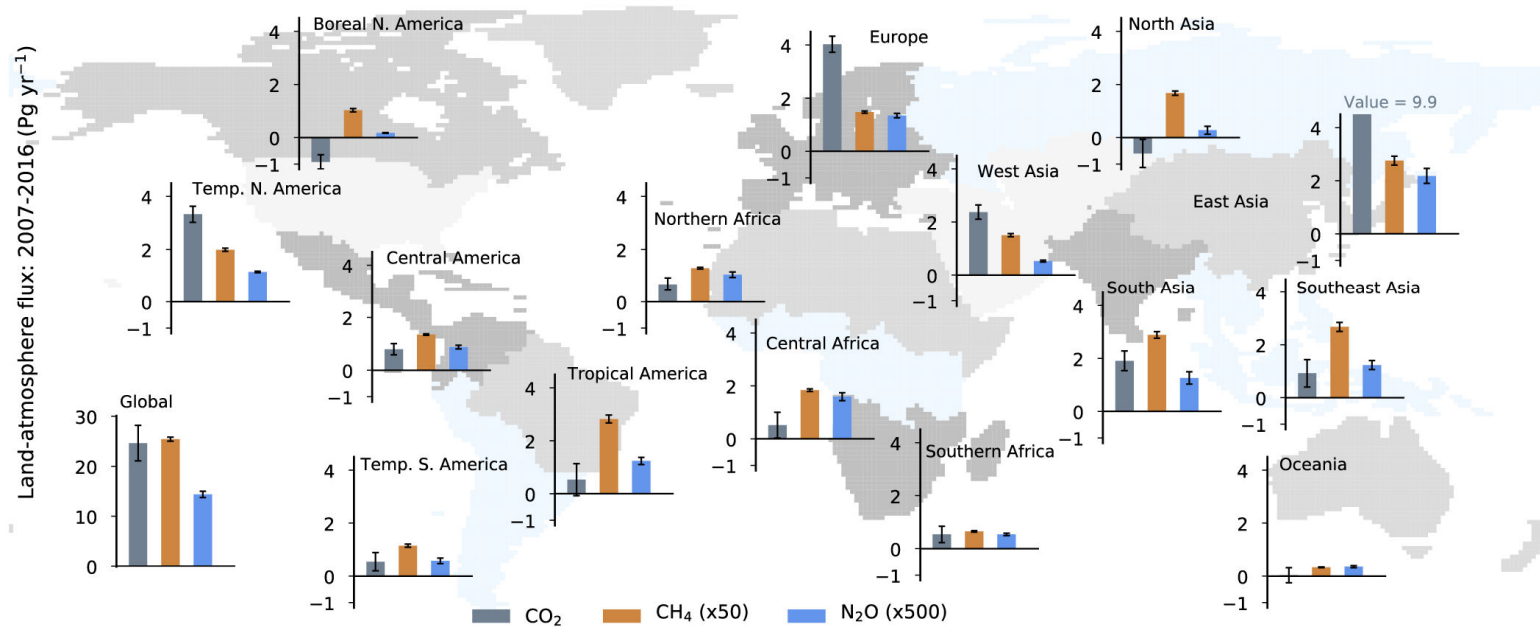
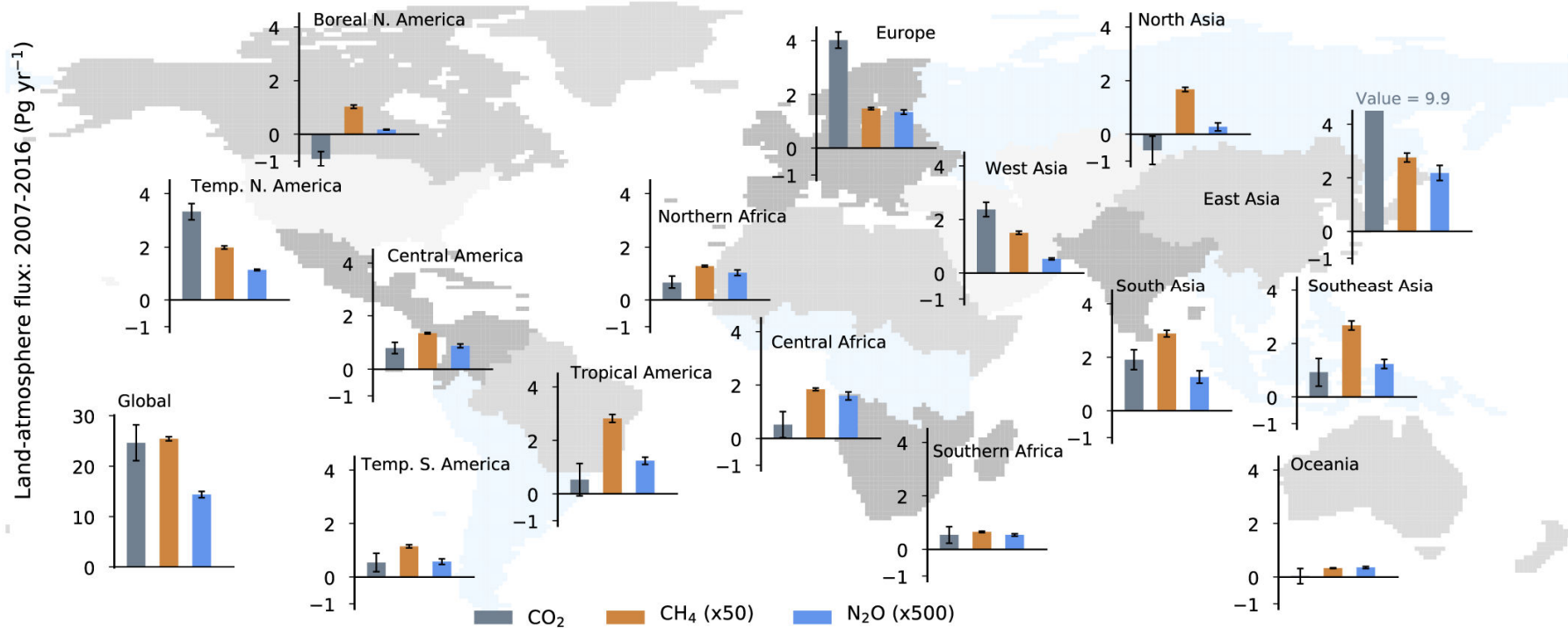


Figure 5.19 | Regional distributions of net fluxes of carbon dioxide (CO₂), methane (CH₄), nitrous oxide (N₂O) on the Earth's surface. The region divisions, shown as the shaded map, are made based on ecoclimatic characteristics of the land. The fluxes include those from anthropogenic activities and natural causes that result from responses to anthropogenic greenhouse gases and climate change (feedbacks) as in the three budgets shown in Sections 5.2.1.5, 5.2.2.5, and 5.2.3.5. The CH₄ and N₂O emissions are weighted by arbitrary factors of 50 and 500, respectively, for depiction by common y-axes. Fluxes are shown as the mean of the inverse models as available from Thompson et al. (2019); Friedlingstein et al. (2020); Saunois et al. (2020). Further details on data sources and processing are available in the chapter data table (Table 5.SM.6).

Regional distributions of net fluxes of carbon dioxide (CO₂), methane (CH₄), nitrous oxide (N₂O) on the Earth's surface

Regional distributions of CO₂, CH₄ and N₂O fluxes by inverse modelling



Statements in the Executive Summary

Ocean Acidification and Ocean Deoxygenation (1)

Ocean acidification is strengthening as a result of the ocean continuing to take up CO₂ from human-caused emissions (*very high confidence*). This CO₂ uptake is driving changes in seawater chemistry that result in the decrease of pH and associated reductions in the saturation state of calcium carbonate, which is a constituent of skeletons or shells of a variety of marine organisms. These trends of ocean acidification are becoming clearer globally, with a *very likely* rate of decrease in pH in the ocean surface layer of 0.016 to 0.020 per decade in the subtropics and 0.002 to 0.026 per decade in subpolar and polar zones since the 1980s. Ocean acidification has spread deeper in the ocean, surpassing 2000 m depth in the northern North Atlantic and in the Southern Ocean. The greater projected pH declines in CMIP6 models are primarily a consequence of higher atmospheric CO₂ concentrations in the Shared Socio-economic Pathways (SSPs) scenarios than their CMIP5-RCP analogues {5.3.2.2, 5.3.3.1; 5.3.4.1; Figures 5.20, 5.21}



Multi-decadal trends of pH in surface layer at various sites of the oceans and a global distribution of annual mean pH adjusted to the year 2000

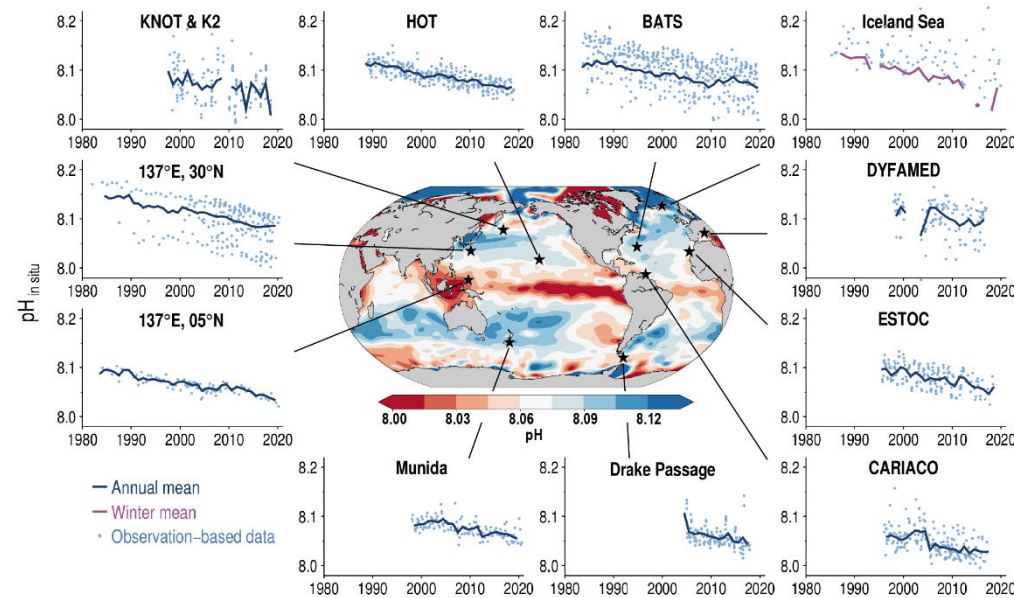
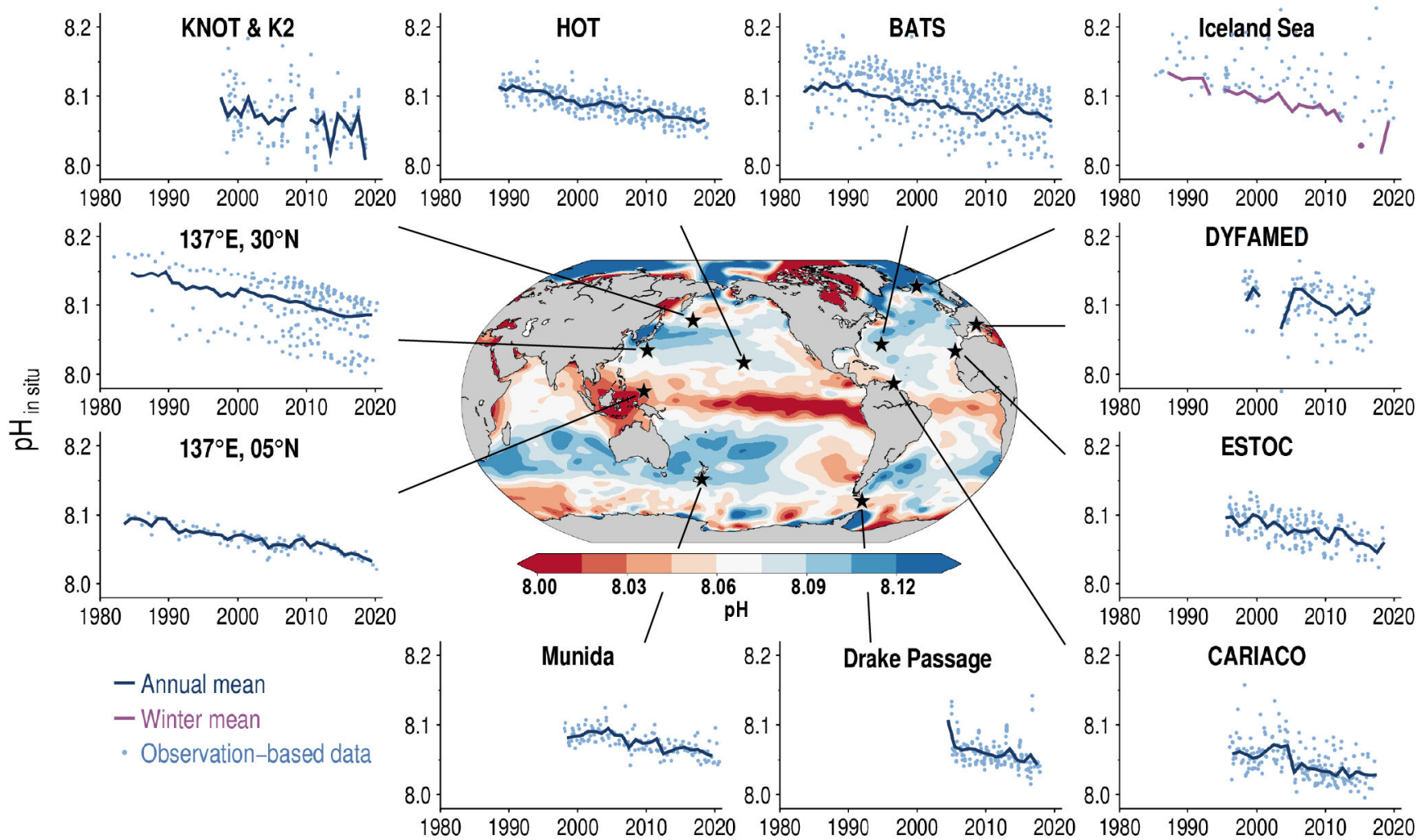


Figure 5.20 | Multi-decadal trends of pH (Total Scale) in surface layer at various sites of the oceans and a global distribution of annual mean pH adjusted to the year 2000. Time-series data of pH are from Dore et al. (2009), Olafsson et al. (2009), González-Dávila et al. (2010), Bates et al. (2014), Takahashi et al. (2014), Wakita et al. (2017), Merlivat et al. (2018), Ono et al. (2019), and Bates and Johnson (2020). Global distribution of annual mean pH have been evaluated from data of surface ocean $p\text{CO}_2$ measurements (Bakker et al., 2016; Jiang et al., 2019). Acronyms in panels: KNOT and K2 – Western Pacific subarctic gyre time series; HOT – Hawaii Ocean Time-series; BATS – Bermuda Atlantic Time-series Study; DYFAMED – Dynamics of Atmospheric Fluxes in the Mediterranean Sea; ESTOC – European Station for Time-series in the Ocean Canary Islands; CARIACO – Carbon Retention in a Colored Ocean Time-series. Further details on data sources and processing are available in the chapter data table (Table 5.SM.6).





Spread of ocean acidification from the surface into the interior of ocean since pre-industrial times

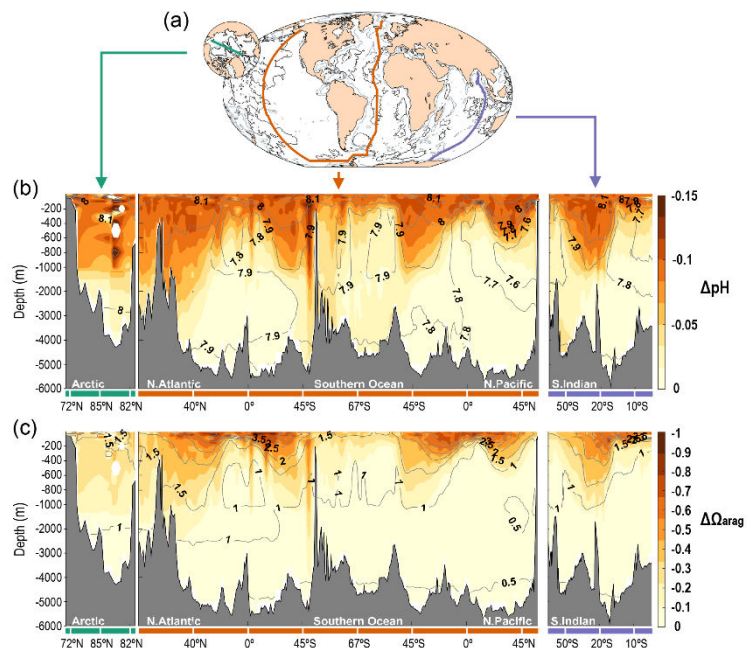
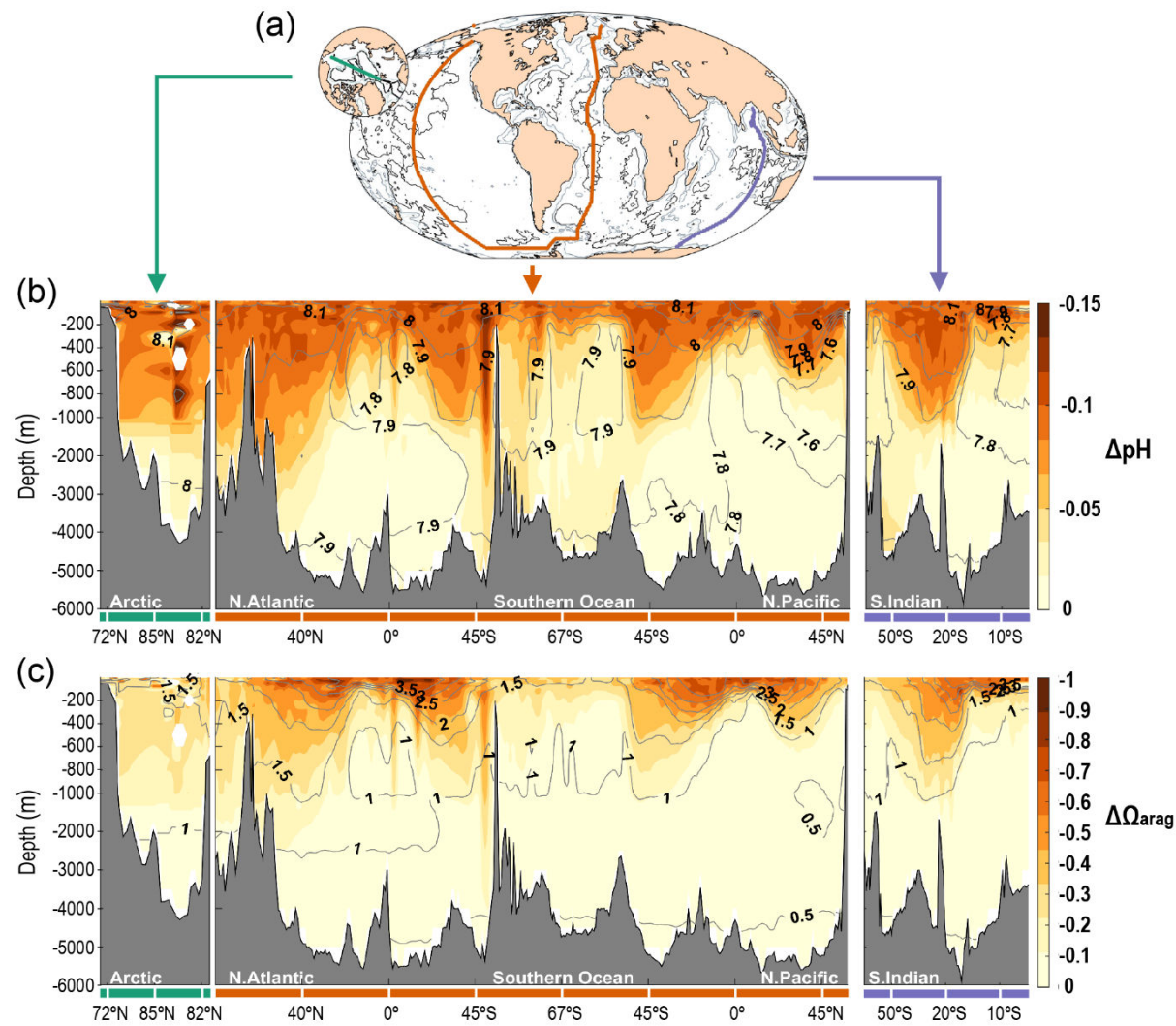


Figure 5.21 | Spread of ocean acidification from the surface into the interior of ocean since pre-industrial times. (a) Map showing the three transects used to create the cross sections shown in (b) and (c); vertical sections of the changes in (b) pH and (c) saturation state of aragonite (Ω_{arag}) between 1800–2002 due to anthropogenic CO_2 invasion (colour). Contour lines are their contemporary values in 2002. The red transect begins in the Nordic Seas and then follows the GO-SHIP lines A16 southward in the Atlantic Ocean, SR04 and S04P westward in the Southern Ocean, and P16 northward in the Pacific Ocean. The purple line follows the GO-SHIP line I09 southward in the Indian Ocean. The green line on the smaller inset crosses the Arctic Ocean from the Bering Strait to North Pole along 175°W and from the North Pole to the Fram Strait along 5°E (Lauvset et al., 2020). Further details on data sources and processing are available in the chapter data table (Table 5.SM.6).





Statements in the Executive Summary

Ocean Acidification and Ocean Deoxygenation (2)

Ocean deoxygenation is projected to continue to increase with ocean warming (*high confidence*). Earth system models (ESMs) project a 32–71% greater subsurface (100–600 m) oxygen decline, depending on scenario, than reported in the Special Report on the Ocean and Cryosphere (SROCC) for the period 2080–2099. This is attributed to the effect of larger surface warming in CMIP6 models, which increases ocean stratification and reduces ventilation (*medium confidence*). There is *low confidence* in the projected reduction of oceanic N₂O emissions under high emission scenarios because of greater oxygen losses simulated in ESMs in CMIP6, uncertainties in the process of oceanic N₂O emissions, and a limited number of modelling studies available {5.3.3.2; 7.5}



Statements in the Executive Summary

Future Projections of Carbon Feedbacks on Climate Change (1)

Oceanic and terrestrial carbon sinks are projected to continue to grow with increasing atmospheric concentrations of CO₂, but the fraction of emissions taken up by land and ocean is expected to decline as the CO₂ concentration increases (*high confidence*).

ESMs suggest approximately equal global land and ocean carbon uptake for each of the SSPs scenarios. However, the range of model projections is much larger for the land carbon sink.

Despite the wide range of model responses, uncertainty in atmospheric CO₂ by 2100 is dominated by future anthropogenic emissions rather than uncertainties related to carbon–climate feedbacks (*high confidence*). {5.4.5; Figure 5.25, 5.26}



CMIP6 Earth system model (ESM) concentration-driven historical simulations for 1850 to 2014, compared to observation-based estimates from the global carbon project (GCP)

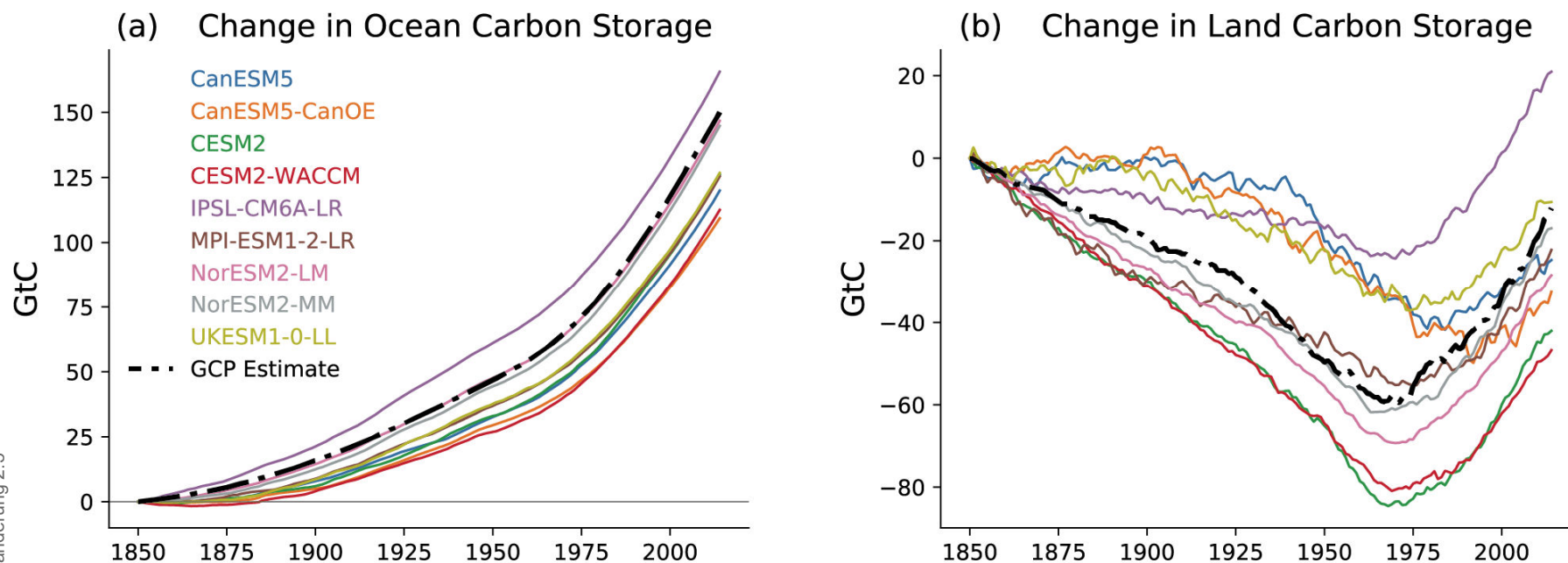


Figure 5.23 | CMIP6 Earth system model (ESM) concentration-driven historical simulations for 1850 to 2014, compared to observation-based estimates from the global carbon project (GCP). (a) Cumulative ocean carbon uptake from 1850 (PgC); (b) cumulative land carbon uptake from 1850 (PgC). Only models that simulate both land and ocean carbon fluxes are shown here. Further details on data sources and processing are available in the chapter data table (Table 5.SM.6).



Comparison of modelled zonal distribution of contemporary carbon sinks against atmospheric inversion estimates for 2000–2009

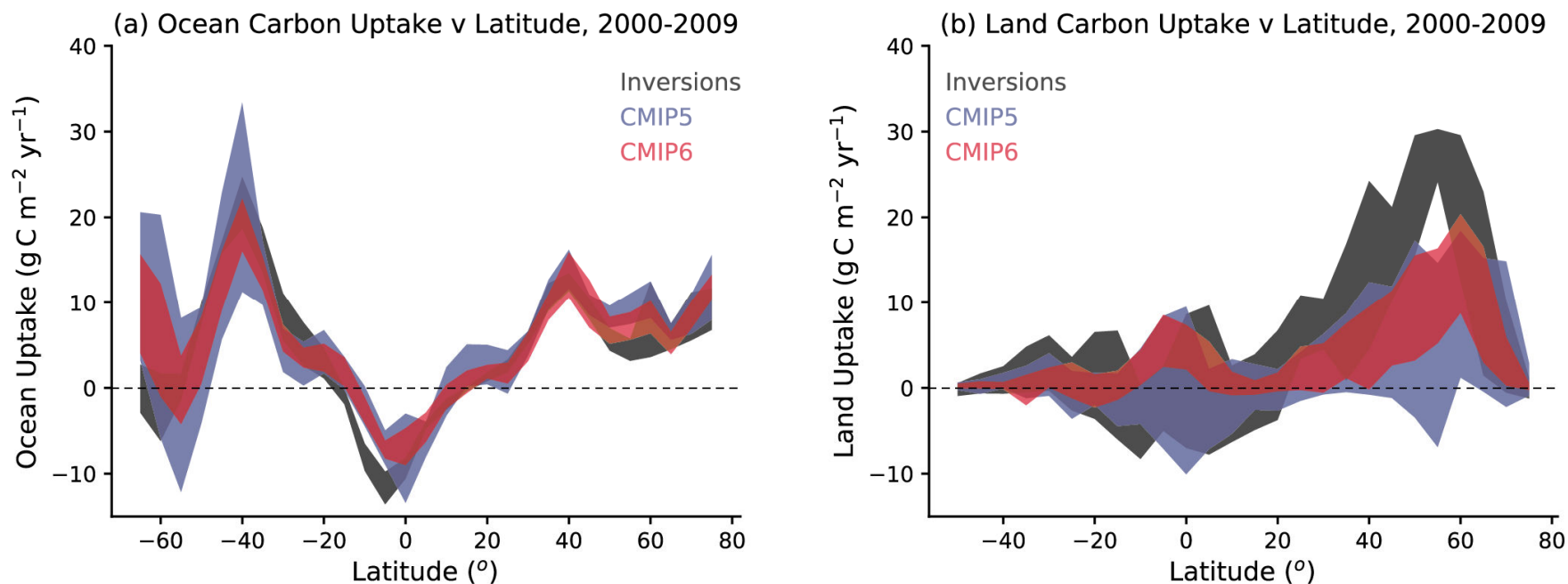


Figure 5.24 | Comparison of modelled zonal distribution of contemporary carbon sinks against atmospheric inversion estimates for 2000–2009: (a) ocean carbon uptake; (b) net land uptake. Latitude runs from 90°S (i.e., –90°N) to 90°N. Positive uptake represents a carbon sink to ocean/land while negative uptake represents a carbon source. The land uptake is taken as net biome productivity (NBP) and so includes net land-use change emissions. The bands show the mean ± 1 standard deviation across the available inversions (black bands, 3 models), CMIP5 Earth system models (ESMs) (blue bands, 12 models for the ocean, 12 models for the land), and CMIP6 ESMs (red bands, 11 models for ocean, 10 models for land). Further details on data sources and processing are available in the chapter data table (Table 5.SM.6).

Modelled evolution of the global land and ocean carbon sinks for 1850 to 2100 in concentration-driven CMIP6 Earth system model (ESM) scenario runs

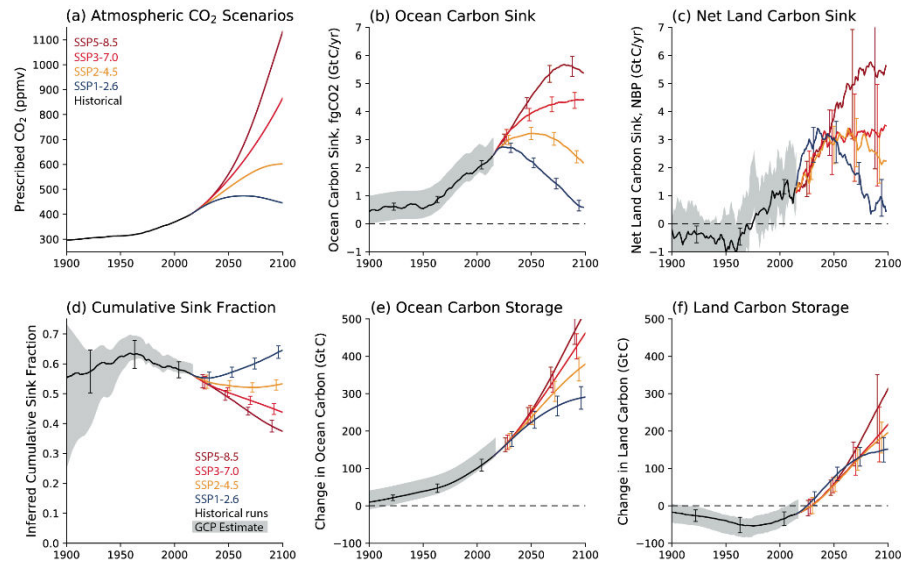
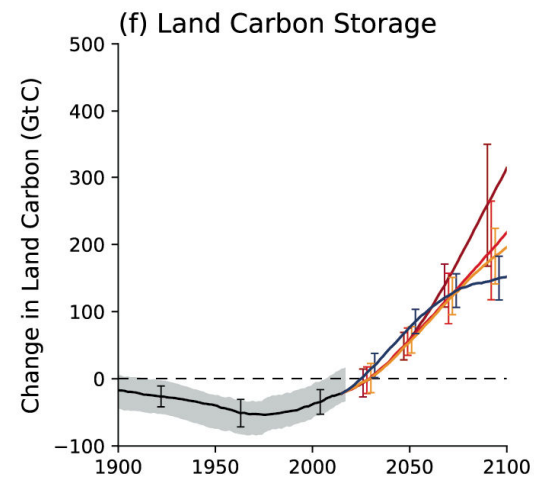
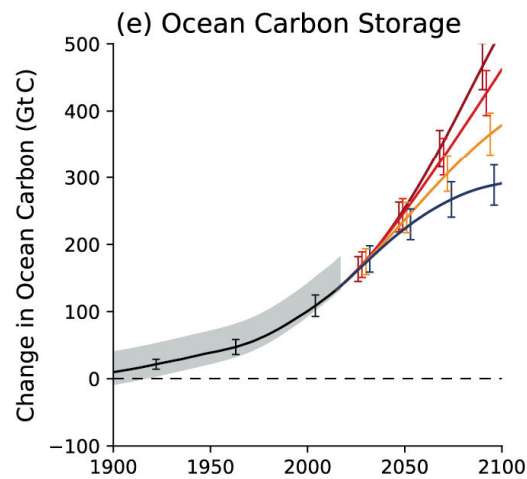
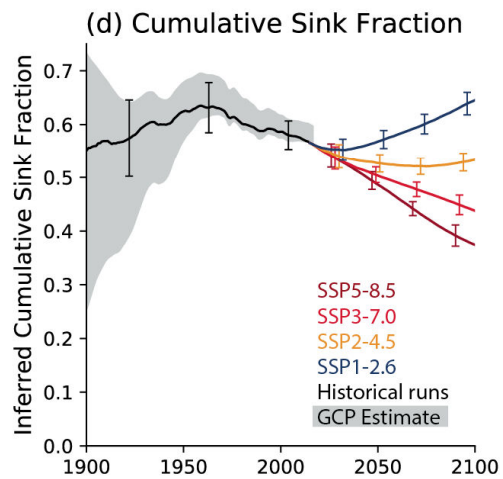
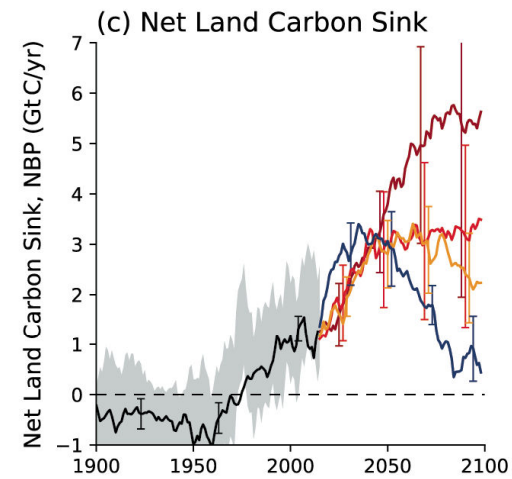
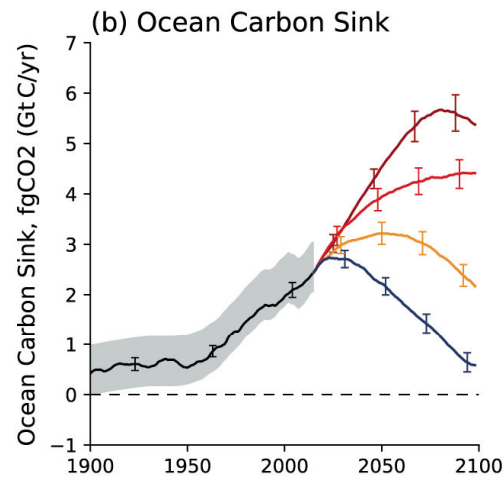
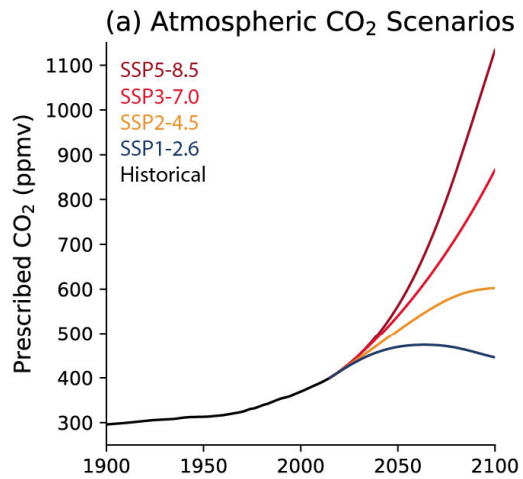


Figure 5.25 | Modelled evolution of the global land and ocean carbon sinks for 1900 to 2100 in concentration-driven CMIP6 Earth system model (ESM) scenario runs. (SSP1-2.6: blue; SSP2-4.5: orange; SSP3-7.0: red; SSP5-8.5: brown): **(a)** prescribed atmospheric CO₂ concentrations; **(b)** five-year running mean ocean carbon sink (GtC yr⁻¹); **(c)** five-year running mean net land carbon sink (GtC yr⁻¹); **(d)** inferred cumulative sink fraction of emissions from 1850; **(e)** change in ocean carbon storage from 1850 (GtC); **(f)** change in land carbon storage from 1850 (GtC). Thick lines represent the ensemble mean of the listed ESM runs, and the error bars represents ± 1 standard deviation about that mean. The grey wedges represent estimates from the global carbon project (GCP), assuming uncertainties in the annual mean ocean and net land carbon sinks of 0.5 GtC yr⁻¹ and 1 GtC yr⁻¹ respectively, and uncertainties in the changes in carbon stores (ocean, land and cumulative total emissions) of 25 GtC. The net land carbon sink is taken as net biome productivity (NBP) and so includes any modelled net land-use change emissions. Further details on data sources and processing are available in the chapter data table (Table 5.SM.6).





22.05.2023



Maps of net carbon changes under four Shared Socioeconomic Pathway (SSP) scenarios, as evaluated from nine CMIP6 Earth system models

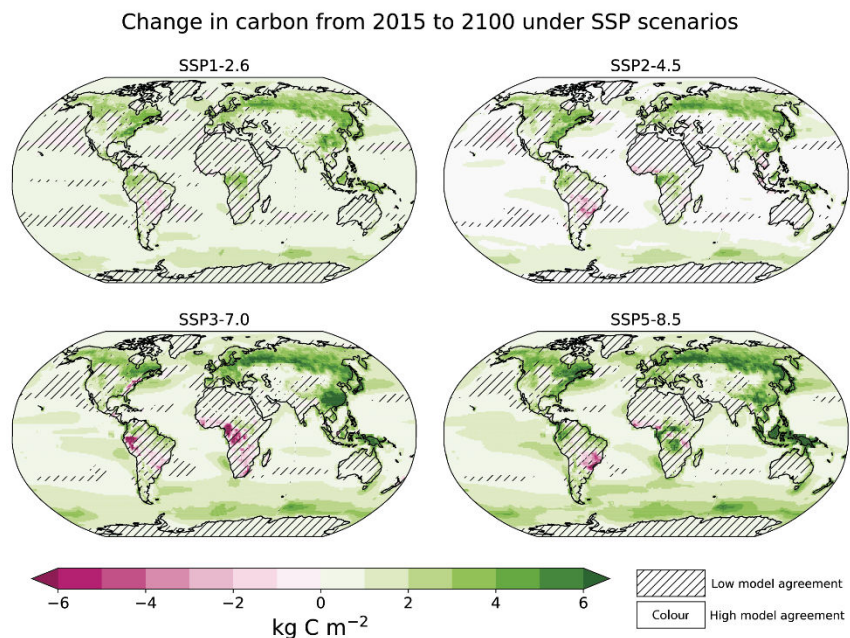
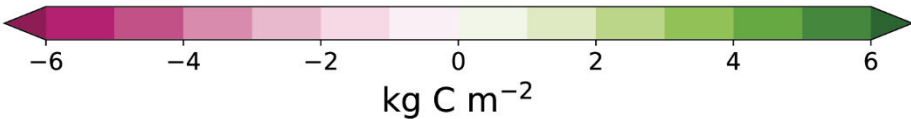
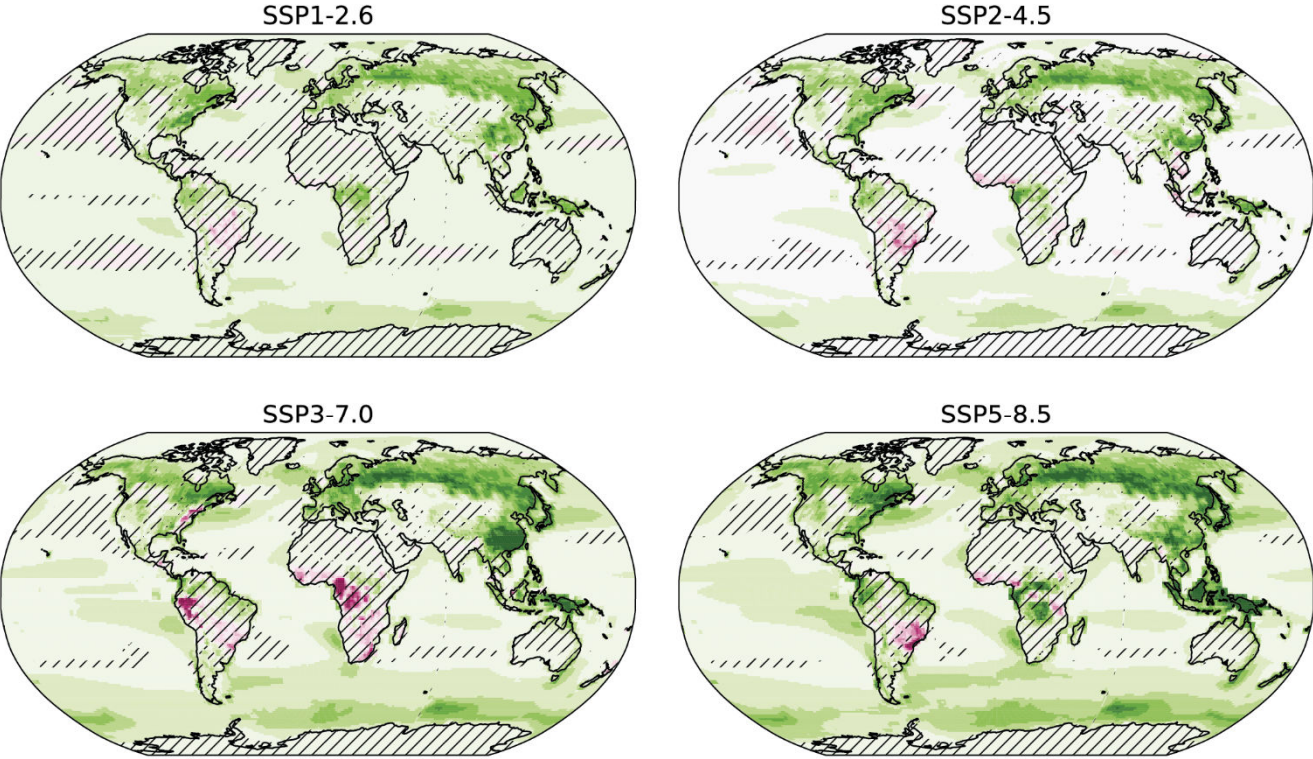




Figure 5.26 | Maps of net carbon changes under four Shared Socio-economic Pathway (SSP) scenarios, as evaluated from nine CMIP6 Earth system models. Uncertainty is represented using the simple approach (see Cross-Chapter Box Atlas.1 for more information). No overlay indicates regions with high model agreement, where $\geq 80\%$ of models agree with the ensemble mean on the sign of change. Diagonal lines indicate regions with low model agreement, where $< 80\%$ of models agree with the ensemble mean on the sign of change. On land, this is calculated as the time integral of net biome productivity (NBP), for the ocean it is the time-integral of air–sea carbon dioxide (CO_2) gas flux anomalies relative to the pre-industrial. Further details on data sources and processing are available in the chapter data table (Table 5.SM.6).



Change in carbon from 2015 to 2100 under SSP scenarios



 Low model agreement
 High model agreement



Statements in the Executive Summary

Future Projections of Carbon Feedbacks on Climate Change (2)

Increases in atmospheric CO₂ lead to increases in land carbon storage through CO₂ fertilization of photosynthesis and increased water use efficiency (*high confidence*). However, the overall change in land carbon also depends on land-use change and on the response of vegetation and soil to continued warming and changes in the water cycle, including increased droughts in some regions that will diminish the sink capacity. Climate change alone is expected to increase land carbon accumulation in the high latitudes (not including permafrost), but also to lead to a counteracting loss of land carbon in the tropics (*medium confidence*, Figure 5.25). More than half of the latest CMIP6 ESMs include nutrient limitations on the carbon cycle, but these models still project increasing tropical land carbon (*medium confidence*) and increasing global land carbon (*high confidence*) through the 21st century. {5.4.1, 5.4.3, 5.4.5; Figure 5.27; Cross-Chapter Box 5.1}



Estimates of the biogeochemical climate feedback parameter (α)

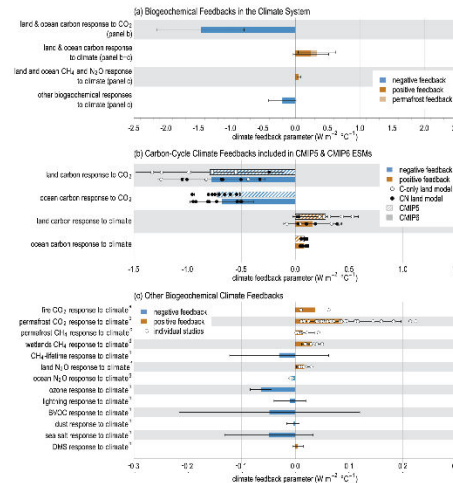
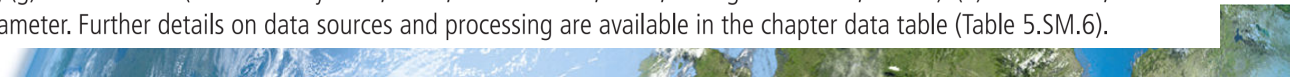
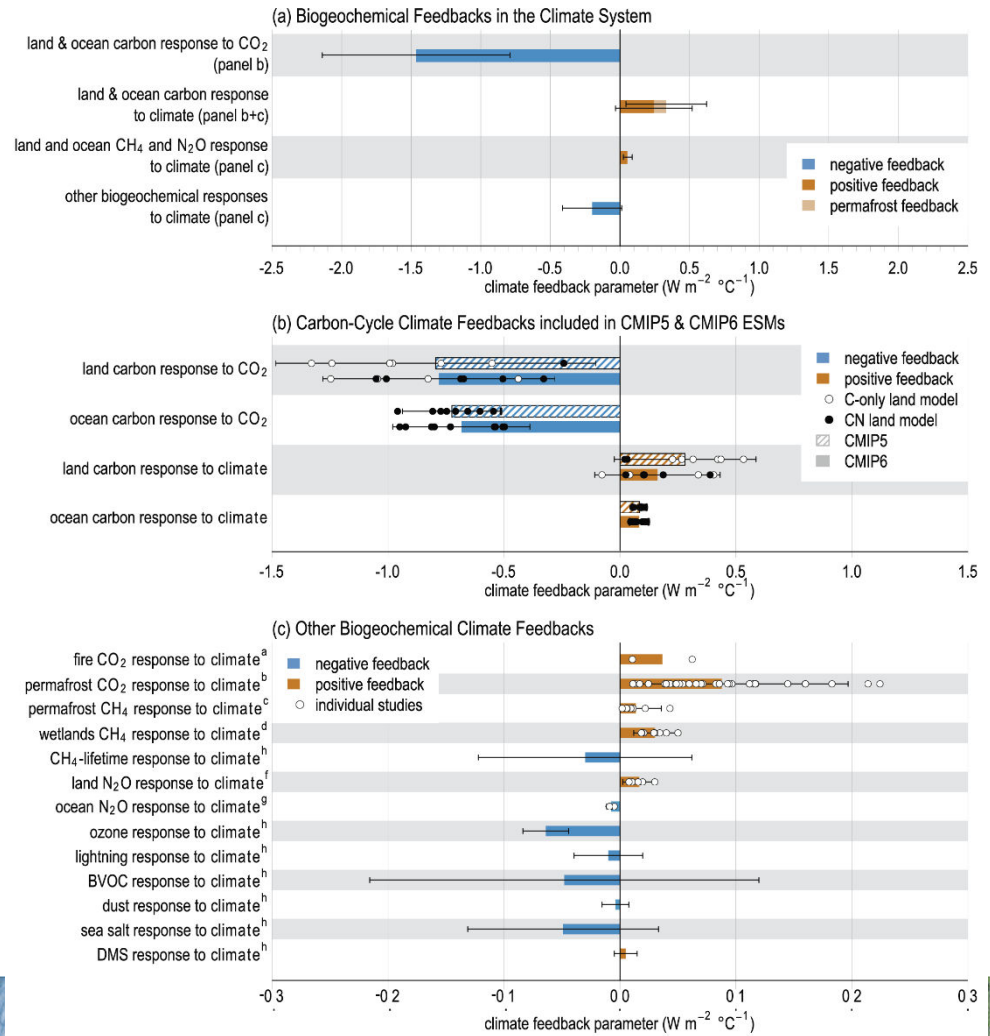


Figure 5.29 | Estimates of the biogeochemical climate feedback parameter (α). The parameter α ($W m^{-2} \text{ } ^\circ C^{-1}$) for a feedback variable x is defined as $\alpha_x = \frac{\delta N}{\delta x} \frac{dx}{dT}$ where $\frac{\delta N}{\delta x}$ is the change in top-of-atmosphere energy balance in response to a change in x induced by a change in surface temperature (T), as in Section 7.4.1.1. **(a)** Synthesis of biogeochemical feedbacks from panels (b) and (c). Orange (blue) bars correspond to positive (negative) feedbacks increasing (decreasing) radiative forcing at the top of the atmosphere. Bars denote the mean and the error bar represents the 5–95% range of the estimates; **(b)** carbon-cycle feedbacks as estimated by coupled carbon-cycle climate models in the CMIP5 (Arora et al., 2013) and CMIP6 (Arora et al., 2020) ensembles, where dots represent single model estimates, and filled (open) circles are those estimates which do (not) include the representation of a terrestrial nitrogen cycle; **(c)** Estimates of other biogeochemical feedback mechanisms based on various modelling studies. Dots represent single estimates, and coloured bars denote the mean of these estimates with no weighting being made regarding the likelihood of any single estimate, and error bars the 5–95% range derived from these estimates. Results in panel (c) have been compiled from (a) Section 5.4.3.2 (Eliseev et al., 2014a; Harrison et al., 2018); (b) Section 5.4.3.3 (Schneider von Deimling et al., 2012; Burke et al., 2013, 2017b; Koven et al., 2015a, c; MacDougall and Knutti, 2016b; Gasser et al., 2018; Kleinen and Brovkin, 2018), where the estimates from Burke et al., 2013 have been constrained as assessed in their study (c) Section 5.4.7 (Schneider von Deimling et al., 2012, 2015; Koven et al., 2015c; Turetsky et al., 2020); (d) Section 5.4.7 (Arneth et al., 2010; Denisov et al., 2013; Shindell et al., 2013; B.D. Stocker et al., 2013; Zhang et al., 2017); (f) Section 5.4.7 (Xu-Ri et al., 2012; B.D. Stocker et al., 2013; Zaehle, 2013; Tian et al., 2019); (g) Section 5.4.7 (Martinez-Rey et al., 2015; Landolfi et al., 2017; Battaglia and Joos, 2018b). (h) Section 6.3, Table 6.9 mean and the 5–95% range the assessed feedback parameter. Further details on data sources and processing are available in the chapter data table (Table 5.SM.6).



Estimates of the biogeochemical climate feedback parameter (α)



Statements in the Executive Summary

Future Projections of Carbon Feedbacks on Climate Change (3)

Future trajectories of the ocean CO₂ sink are strongly emissions-scenario dependent (*high confidence*). Emission scenarios SSP4-6.0 and SSP5-8.5 lead to warming of the surface ocean and large reductions of the buffering capacity, which will slow the growth of the ocean sink after 2050. Scenario SSP1-2.6 limits further reductions in buffering capacity and warming, and the ocean sink weakens in response to the declining rate of increasing atmospheric CO₂. There is *low confidence* in how changes in the biological pump will influence the magnitude and direction of the ocean carbon feedback. {5.4.2, 5.4.4, Cross-Chapter Box 5.3}



Statements in the Executive Summary

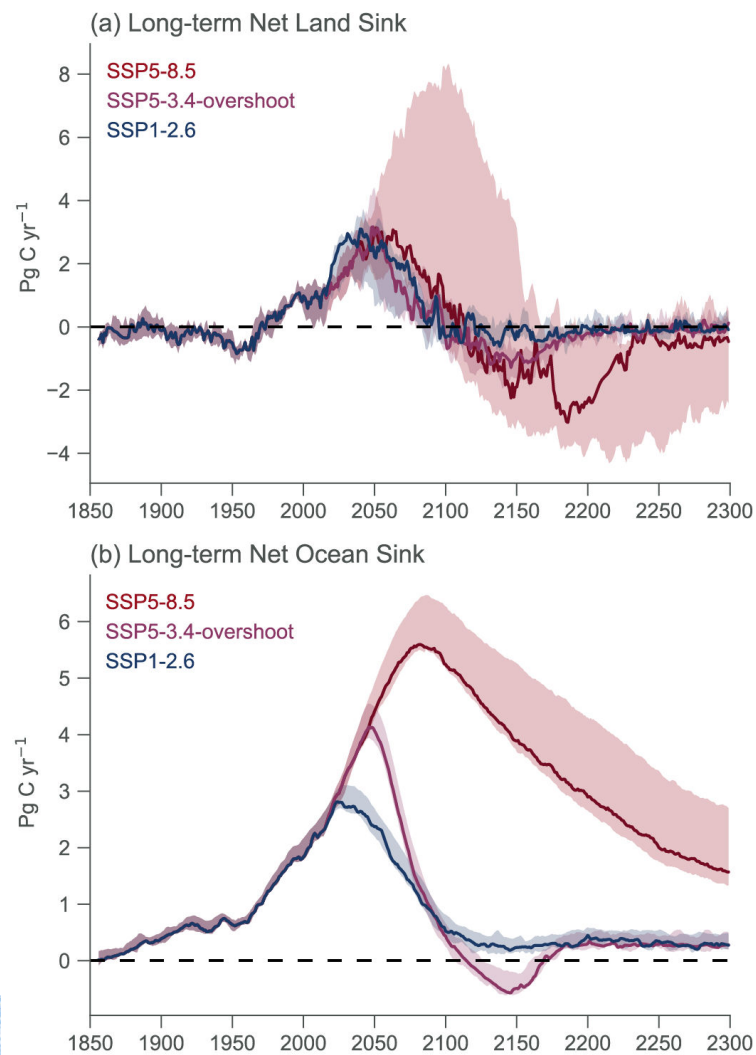
Future Projections of Carbon Feedbacks on Climate Change (4)

Beyond 2100, land and ocean may transition from being a carbon sink to a source under either very high emissions or net negative emissions scenarios, but for different reasons. Under very high emissions scenarios such as SSP5-8.5, ecosystem carbon losses due to warming lead the land to transition from a carbon sink to a source (*medium confidence*), while the ocean is expected to remain a sink (*high confidence*). For scenarios in which CO₂ concentration stabilizes, land and ocean carbon sinks gradually take up less carbon as the increase in atmospheric CO₂ slows down. In scenarios with moderate net negative CO₂ emissions and CO₂ concentrations declining during the 21st century (e.g., SSP1-2.6), the land sink transitions to a net source in decades to a few centuries after CO₂ emissions become net negative, while the ocean remains a sink (*low confidence*). Under scenarios with large net negative CO₂ emissions and rapidly declining CO₂ concentrations (e.g., SSP5-3.4-OS (overshoot)), both land and ocean switch from a sink to a transient source during the overshoot period (*medium confidence*). {5.4.10, 5.6.2.1.2; Figures 5.30, 5.33}



Trajectories of carbon cycle dynamics for models beyond 2100

Figure 5.30 | Trajectories of carbon cycle dynamics for models beyond 2100. Shown are three scenarios: SSP5-8.5; SSP5-3.4-overshoot; and SSP1-2.6, from four ESMs (CanESM5, UKESM1, CESM2-WACCM, IPSL-CM6a-LR) and one EMIC (UVIC-ESCM, Mengis et al., 2020) for which extensions beyond 2100 are available. Solid lines represent the median flux value across the ensemble, and shading represents 15th–85th percentiles across the ensemble. Further details on data sources and processing are available in the chapter data table (Table 5.SM.6).



Statements in the Executive Summary

Future Projections of Carbon Feedbacks on Climate Change (5)

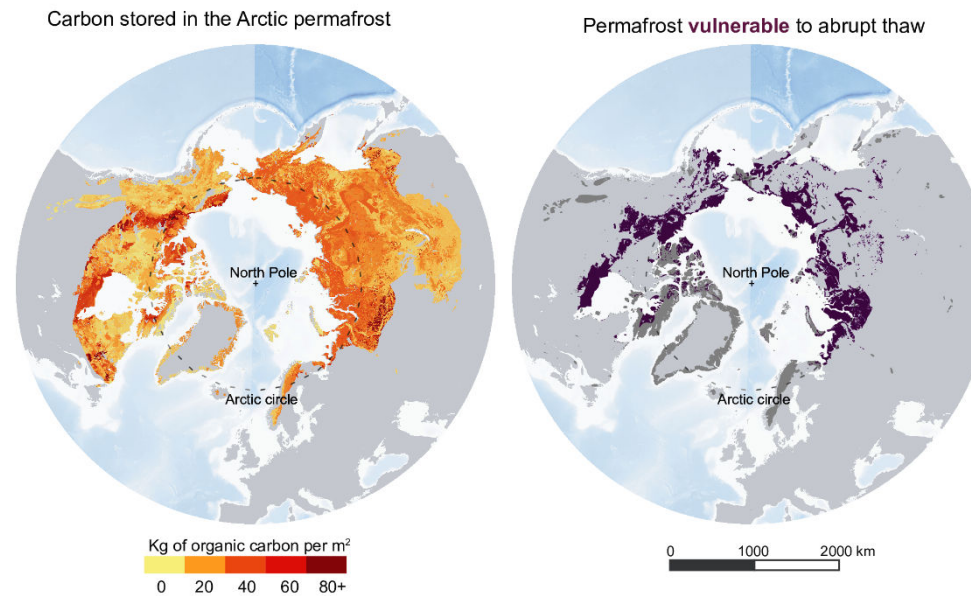
Thawing terrestrial permafrost will lead to carbon release (*high confidence*), but there is *low confidence* in the timing, magnitude and the relative roles of CO₂ versus CH₄ as feedback processes. CO₂ release from permafrost is projected to be 3–41 PgC per 1°C of global warming by 2100, based on an ensemble of models. However, the incomplete representation of important processes such as abrupt thaw, combined with weak observational constraints, only allow *low confidence* in both the magnitude of these estimates and in how linearly proportional this feedback is to the amount of global warming. It is *very unlikely* that gas clathrates in terrestrial and subsea permafrost will lead to a detectable departure from the emissions trajectory during this century. {5.4.9; Box 5.1}



The Arctic permafrost is a big pool of carbon that is sensitive to climate change

FAQ5.2: Can thawing permafrost substantially increase global temperatures?

The thawing of frozen ground in the Arctic will release carbon that will amplify global warming but this will not lead to runaway warming.



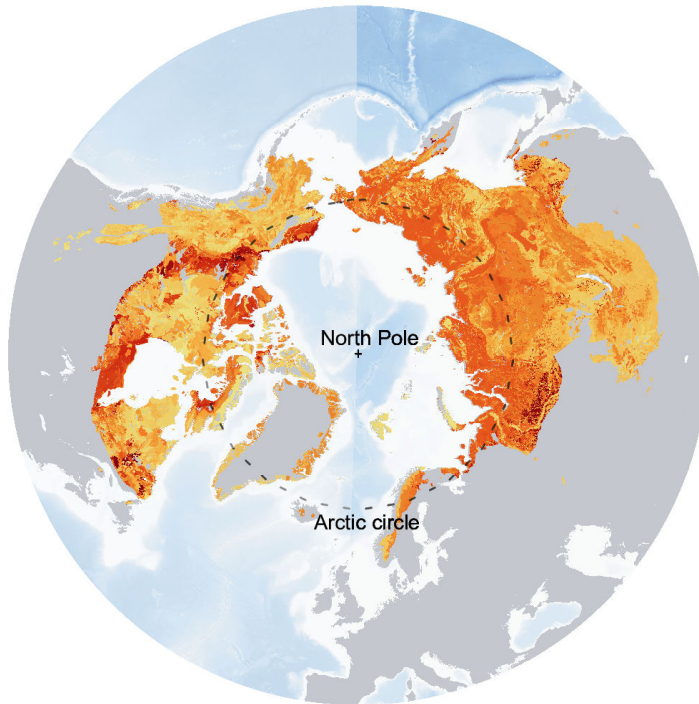
FAQ 5.2, Figure 1 | The Arctic permafrost is a big pool of carbon that is sensitive to climate change. (Left) Quantity of carbon stored in the permafrost, to 3 m depth (NCSCDv2 dataset) and **(right)** area of permafrost vulnerable to abrupt thaw (Circumpolar Thermokarst Landscapes dataset).



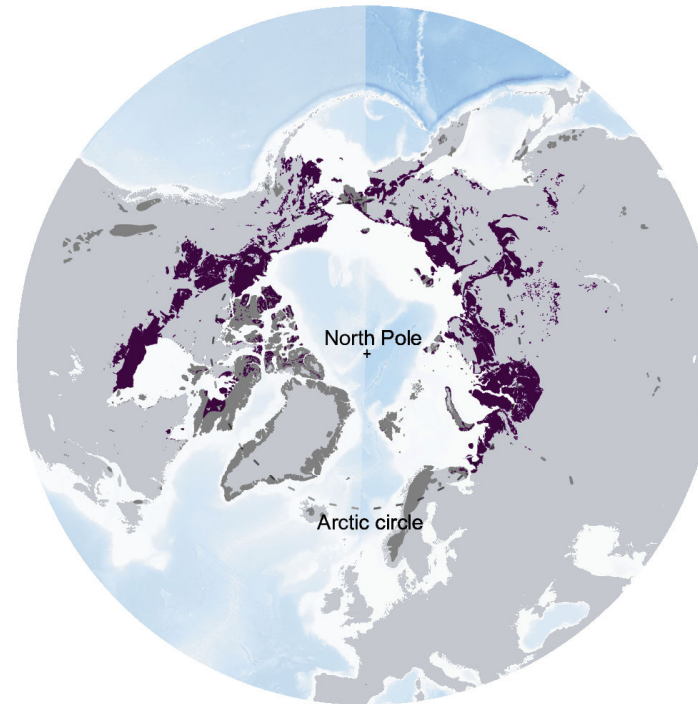
FAQ5.2: Can thawing permafrost substantially increase global temperatures?

The thawing of frozen ground in the Arctic will release carbon that will amplify global warming but this will not lead to runaway warming.

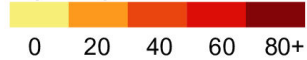
Carbon stored in the Arctic permafrost



Permafrost **vulnerable** to abrupt thaw



Kg of organic carbon per m²



0 1000 2000 km

Statements in the Executive Summary

Future Projections of Carbon Feedbacks on Climate Change (6)

The net response of natural CH₄ and N₂O sources to future warming will be increased emissions (*medium confidence*). Key processes include increased CH₄ emissions from wetlands and permafrost thaw, as well as increased soil N₂O emissions in a warmer climate, while ocean N₂O emissions are projected to decline at centennial time scale. The magnitude of the responses of each individual process and how linearly proportional these feedbacks are to the amount of global warming is known with *low confidence* due to incomplete representation of important processes in models combined with weak observational constraints. Models project that over the 21st century the combined feedback of 0.02–0.09 W m⁻² °C⁻¹ is comparable to the effect of a CO₂ release of 5-18 PgCeq °C⁻¹ (*low confidence*). {5.4.7, 5.4.8; Figure 5.29}



Statements in the Executive Summary

Future Projections of Carbon Feedbacks on Climate Change (7)

The response of biogeochemical cycles to the anthropogenic perturbation can be **abrupt at regional scales, and irreversible on decadal to century time scales (*high confidence*)**. The probability of crossing uncertain regional thresholds (e.g., high severity fires, forest dieback) increases with climate change (*high confidence*). Possible abrupt changes and tipping points in biogeochemical cycles lead to additional uncertainty in 21st century GHG concentrations, but these are very likely to be smaller than the uncertainty associated with future anthropogenic emissions (*high confidence*). {5.4.9}



Statements in the Executive Summary

Remaining Carbon Budgets to Climate Stabilization (1)

There is a near-linear relationship between cumulative CO₂ emissions and the increase in global mean surface air temperature (GSAT) caused by CO₂ over the course of this century for global warming levels up to at least 2°C relative to pre-industrial (*high confidence*). Halting global warming would thus require global net anthropogenic CO₂ emissions to become zero. The ratio between cumulative CO₂ emissions and the consequent GSAT increase, which is called the transient climate response to cumulative emissions of CO₂ (TCRE), *likely* falls in the 1.0°C–2.3°C per 1000 PgC range. The narrowing of this range compared to AR5 is due to a better integration of evidence across the science in this assessment. Beyond this century, there is *low confidence* that the TCRE remains an accurate predictor of temperature changes in scenarios of very low or net negative CO₂ emissions because of uncertain Earth system feedbacks that can result in further warming or a path-dependency of warming as a function of cumulative CO₂ emissions. {5.4, 5.5.1}



Illustration of relationship between cumulative emissions of CO₂ and global mean surface air temperature increase and conceptual schematic of the assessment of the remaining carbon budget from its constituting components

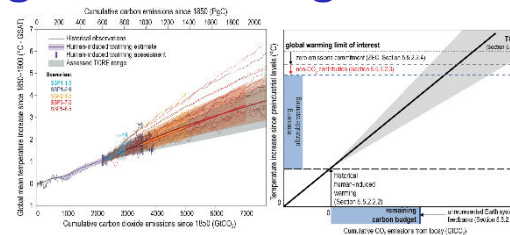
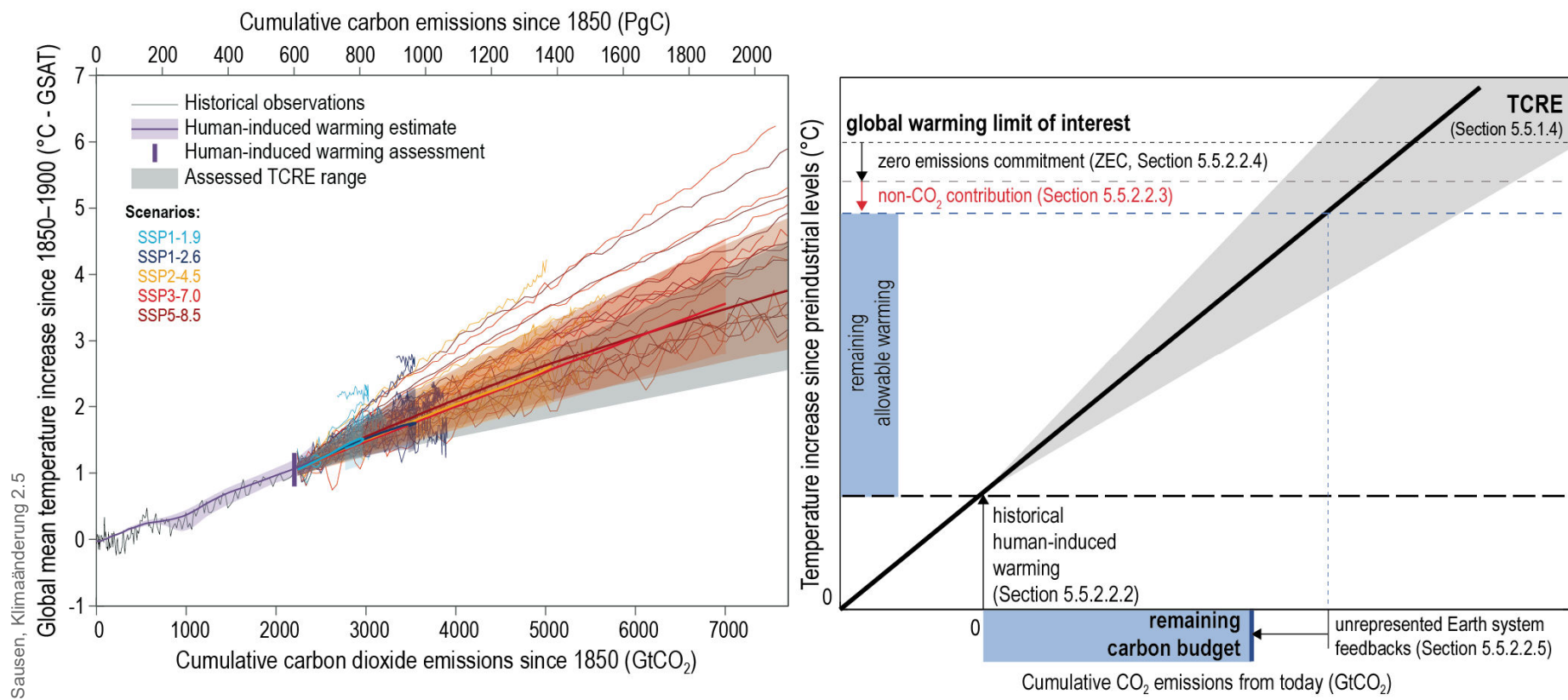


Figure 5.31 | Illustration of relationship between cumulative emissions of carbon dioxide (CO₂) and global mean surface air temperature (GSAT) increase (left) and conceptual schematic of the assessment of the remaining carbon budget from its constituting components (right). Carbon budgets consistent with various levels of additional warming are provided in Table 5.8 and should not be read from the illustrations in either panel. Left-hand panel: Historical data (thin black line data) shows historical CO₂ emissions as reported in Friedlingstein et al. (2020) together with the assessed global mean surface air temperature increase from 1850–1900 as assessed in Chapter 2 (Box 2.3, GSAT). The orange-brown range with its central line shows the estimated human-induced share of historical warming (Haustein et al., 2017). The vertical orange-brown line shows the assessed range of historical human-induced warming for the 2010–2019 period relative to 1850–1900 (Chapter 3). The grey cone shows the assessed range for the transient climate response to cumulative CO₂ emissions (TCRE) assessed to fall *likely* in the 1.0°C–2.3°C per 1000 PgC range (Section 5.5.1.4), starting from 2015. Thin coloured lines show CMIP6 simulations for the five scenarios of the AR6 core set (SSP1-1.9, sky blue; SSP1-2.6, dark blue; SSP2-4.5, yellow; SSP3-7.0, red; SSP5-8.5, maroon), starting from 2015. Diagnosed carbon emissions (Arora et al., 2020) are complemented with estimated land-use change emissions for each respective scenario (Gidden et al., 2019). Coloured areas show the Chapter 4 assessed *very likely* range of GSAT projections and thick coloured central lines the median estimate, for each respective scenario. These projections are expressed relative to the cumulative CO₂ emissions that are available for emissions-driven CMIP6 ScenarioMIP experiments for each respective scenario (Riahi et al., 2017; Rogelj et al., 2018a; Gidden et al., 2019). Right-hand panel: schematic illustration of assessment of remaining carbon budget based on multiple lines of evidence. The remaining allowable warming is estimated by combining the global warming limit of interest with the assessed historical human induced warming (Section 5.5.2.2.2), the assessed future potential non-CO₂ warming contribution (Section 5.5.2.2.3) and the zero emissions commitment (Section 5.5.2.2.4). Note that contributions in the right-hand panel are illustrative and contributions are not to scale. For example, the central ZEC estimate was assessed to be zero. The remaining allowable warming (vertical blue bar) is subsequently combined with the assessed TCRE (Sections 5.5.1.4 and 5.5.2.2.1) and contribution of unrepresented Earth system feedbacks in models used to estimate ZEC and TCRE (Section 5.5.2.2.5) to provide an assessed estimate of the remaining carbon budget (horizontal blue bar; see Table 5.8). Further details on data sources and processing are available in the chapter data table (Table 5.SM.6).

Illustration of relationship between cumulative emissions of CO₂ and global mean surface air temperature increase and conceptual schematic of the assessment of the remaining carbon budget from its constituting components



Sausen, Klimaänderung 2.5

IPCC 2021, Chap. 5



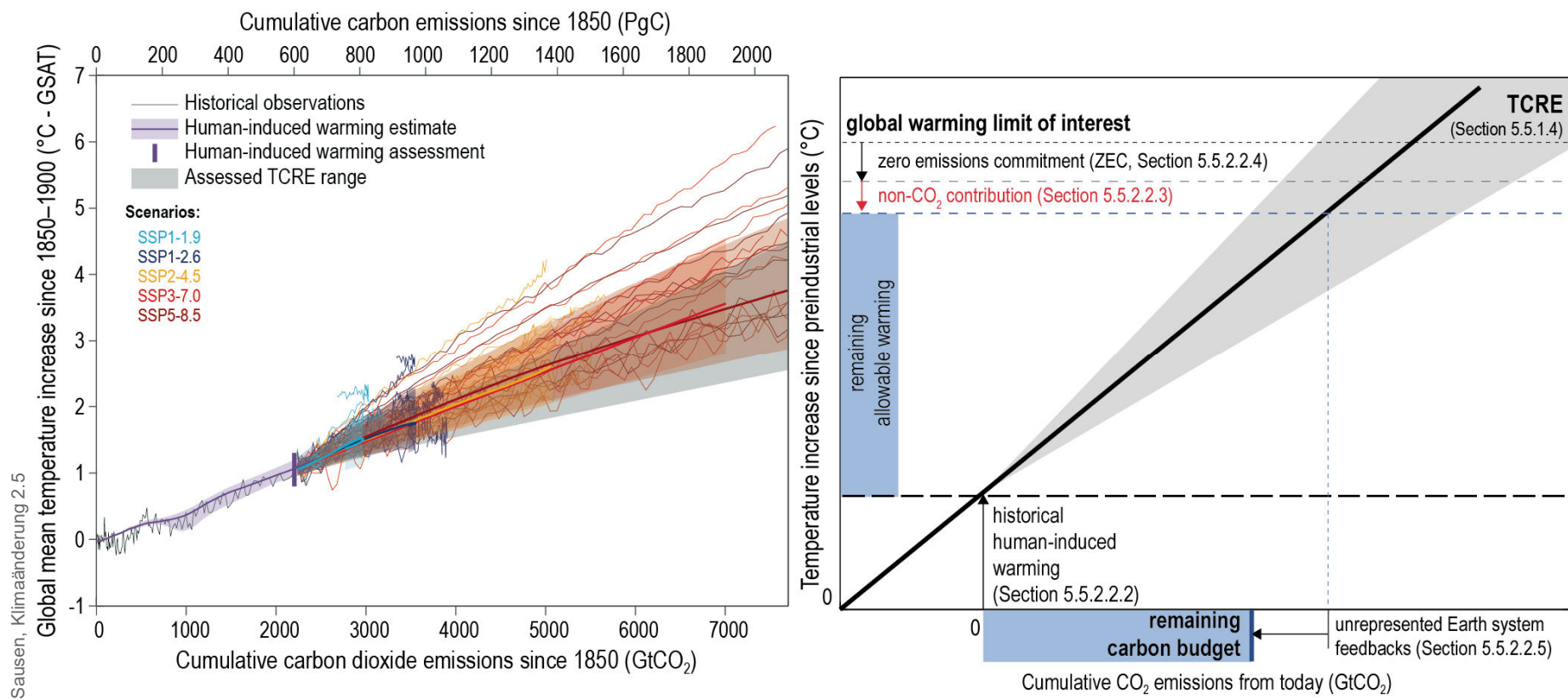
Statements in the Executive Summary

Remaining Carbon Budgets to Climate Stabilization (2)

Mitigation requirements over this century for limiting maximum warming to specific levels can be quantified using a carbon budget that relates cumulative CO₂ emissions to global mean temperature increase (*high confidence*). For the period 1850–2019, a total of 655 ± 65 PgC (2390 ± 240 GtCO₂) of anthropogenic CO₂ has been emitted. Remaining carbon budgets (starting from 1 January 2020) for limiting warming to 1.5°C, 1.7°C, and 2.0°C are 140 PgC (500 GtCO₂), 230 PgC (850 GtCO₂) and 370 PgC (1350 GtCO₂), respectively, based on the 50th percentile of TCRE. For the 67th percentile, the respective values are 110 PgC (400 GtCO₂), 190 PgC (700 GtCO₂) and 310 PgC (1150 GtCO₂). These remaining carbon budgets may vary by an estimated ± 60 PgC (220 GtCO₂) depending on how successfully future non-CO₂ emissions can be reduced. Since AR5 and SR1.5, estimates have undergone methodological improvements, resulting in larger, yet consistent estimates. {5.5.2, 5.6; Figure 5.31; Table 5.8}



Illustration of relationship between cumulative emissions of CO₂ and global mean surface air temperature increase and conceptual schematic of the assessment of the remaining carbon budget from its constituting components



Sausen, Klimaänderung 2.5

IPCC 2021, Chap. 5



Statements in the Executive Summary

Remaining Carbon Budgets to Climate Stabilization (3)

Several factors affect the precise value of remaining carbon budgets, including estimates of historical warming, future emissions from thawing permafrost, and variations in projected non-CO₂ warming. Remaining carbon budget estimates can increase or decrease by 150 PgC (550 GtCO₂, *likely range*) due to uncertainties in the level of historical warming, and by an additional ± 60 PgC (± 220 GtCO₂, *likely range*) due to geophysical uncertainties surrounding the climate response to non-CO₂ emissions such as CH₄, N₂O, and aerosols. Permafrost thaw is included in the estimates together with other feedbacks that are often not captured by models. Despite the large uncertainties surrounding the quantification of the effects of additional Earth system feedback processes, such as emissions from wetlands and permafrost thaw, these feedbacks represent identified additional amplifying risk factors that scale with additional warming and mostly increase the challenge of limiting warming to specific temperature thresholds. These uncertainties do not change the basic conclusion that global CO₂ emissions would need to decline to at least net zero to halt global warming. {5.4, 5.5.2}



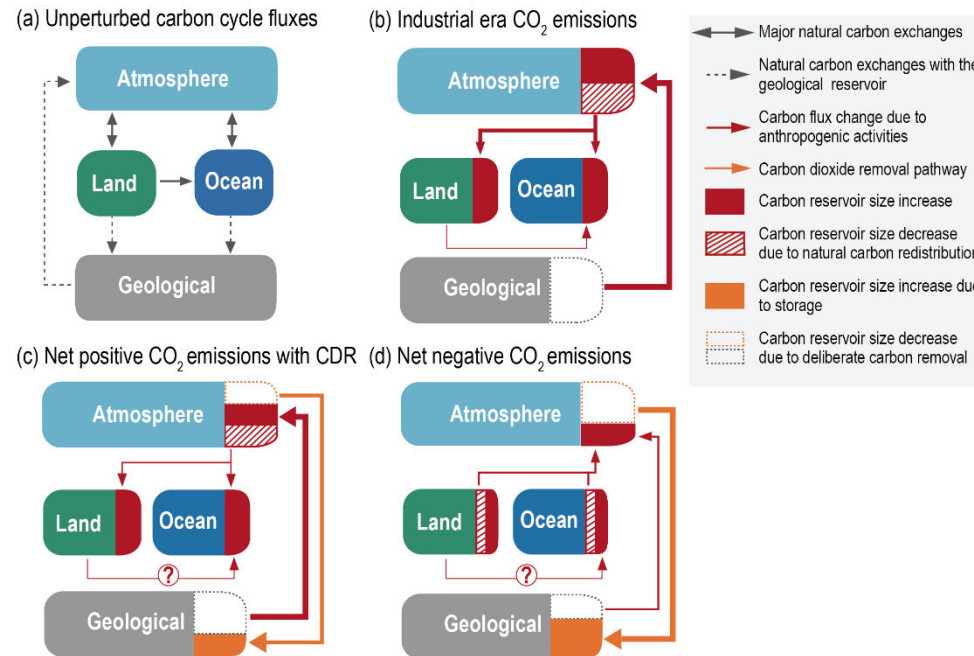
Statements in the Executive Summary

Biogeochemical Implications of Carbon Dioxide Removal and Solar Radiation Modification (1)

Land- and ocean-based carbon dioxide removal (CDR) methods have the potential to sequester CO₂ from the atmosphere, but the benefits of this removal would be partially offset by CO₂ release from land and ocean carbon stores (*very high confidence*). The fraction of CO₂ removed that remains out of the atmosphere, a measure of CDR effectiveness, decreases slightly with increasing amount of removal (*medium confidence*) and decreases strongly if CDR is applied at lower CO₂ concentrations (*medium confidence*). {5.6.2.1; Figures 5.32, 5.33, 5.34}

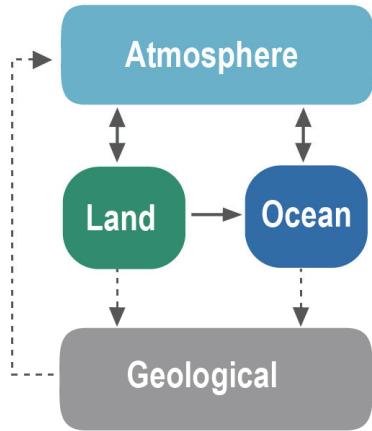


Schematic representation of carbon fluxes between atmosphere, land, ocean and geological reservoirs

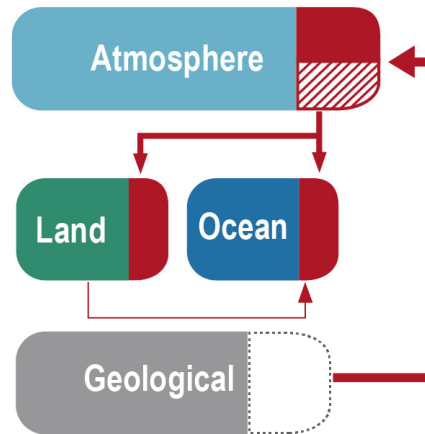


Box 5.3, Figure 1 | Schematic representation of carbon fluxes between atmosphere, land, ocean and geological reservoirs. Different system conditions are shown: **(a)** an unperturbed Earth system; and changes in carbon fluxes for **(b)** an Earth system perturbed by fossil fuel carbon dioxide (CO₂) emissions; **(c)** an Earth system in which fossil fuel CO₂ emissions are partially offset by carbon dioxide removal (CDR); **(d)** an Earth system in which CDR exceeds CO₂ emissions from fossil fuels ('net negative' CO₂ emissions). Carbon fluxes depicted in (a) (solid and dashed black lines) also occur in (b–d). The question mark in the land-to-ocean carbon flux perturbation in (c) and (d) indicates that the effect of CDR on this flux is unknown. Note that box sizes do not scale with the size of carbon reservoirs. Adapted from Keller et al. (2018a). Further details on data sources and processing are available in the chapter data table (Table 5.SM.6).

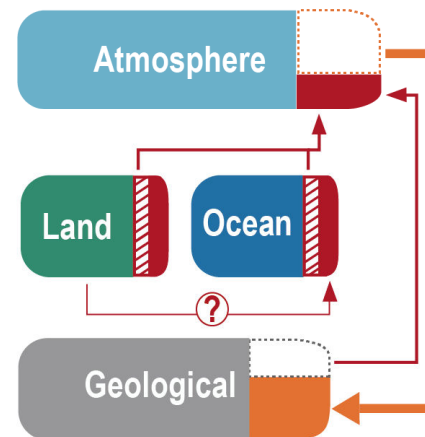
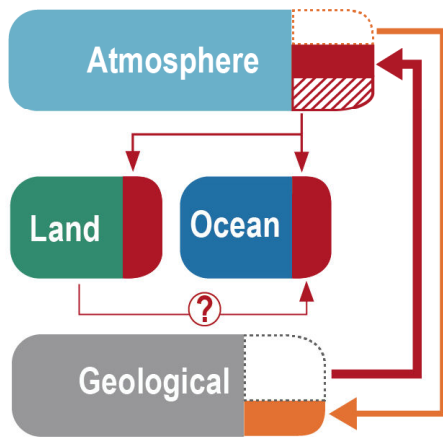
(a) Unperturbed carbon cycle fluxes



(b) Industrial era CO₂ emissions



(c) Net positive CO₂ emissions with CDR (d) Net negative CO₂ emissions



- Major natural carbon exchanges
- Natural carbon exchanges with the geological reservoir
- Carbon flux change due to anthropogenic activities
- Carbon dioxide removal pathway
- Carbon reservoir size increase
- Carbon reservoir size decrease due to natural carbon redistribution
- Carbon reservoir size increase due to storage
- Carbon reservoir size decrease due to deliberate carbon removal



Statements in the Executive Summary

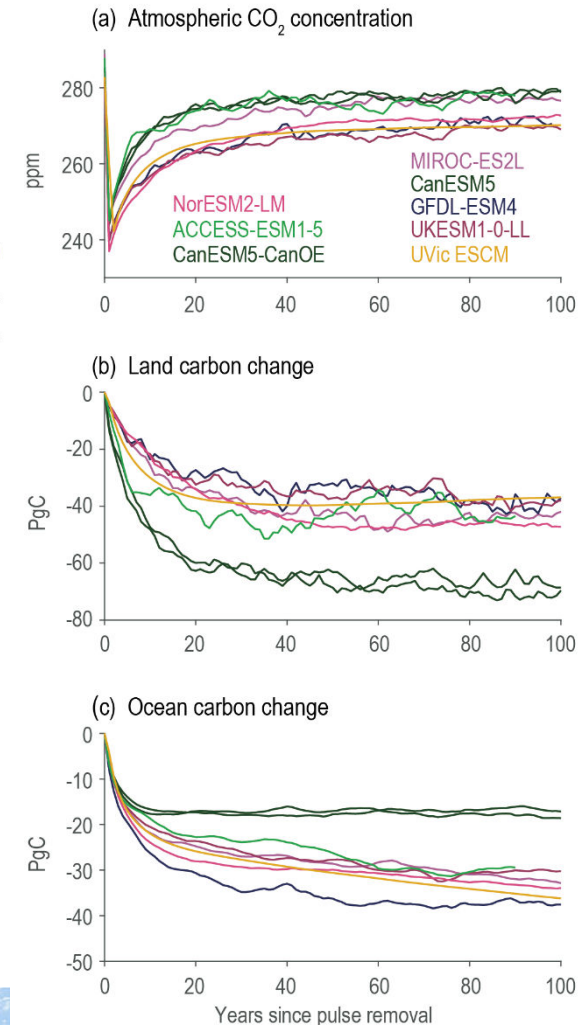
Biogeochemical Implications of Carbon Dioxide Removal and Solar Radiation Modification (2)

The century-scale climate–carbon cycle response to a CO₂ removal from the atmosphere is not always equal and opposite to the response to a CO₂ emission (*medium confidence*). For simultaneously cumulative CO₂ emissions and removals of greater than or equal to 100 PgC, CO₂ emissions are $4 \pm 3\%$ more effective at raising atmospheric CO₂ than CO₂ removals are at lowering atmospheric CO₂. The asymmetry originates from state-dependencies and non-linearities in carbon cycle processes and implies that an extra amount of CDR is required to compensate for a positive emission of a given magnitude to attain the same change in atmospheric CO₂. The net effect of this asymmetry on the global surface temperature is poorly constrained due to low agreement between models (*low confidence*). {5.6.2.1; Figure 5.35}



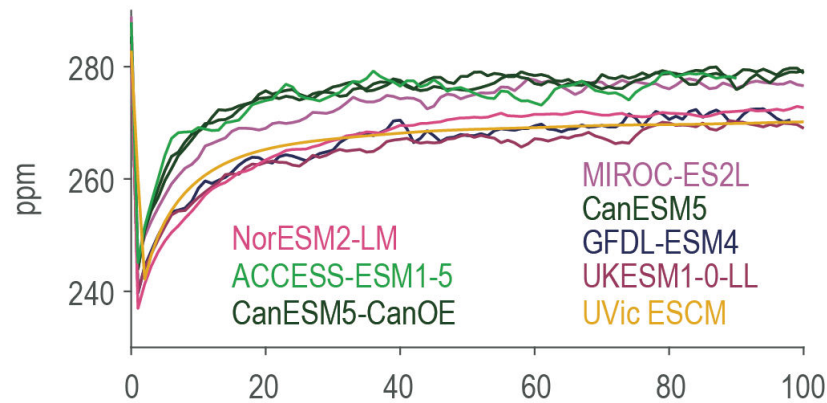
Carbon cycle response to instantaneous carbon dioxide (CO₂) removal from the atmosphere

Figure 5.32 | Carbon cycle response to instantaneous carbon dioxide (CO₂) removal from the atmosphere. (a) Atmospheric CO₂ concentration; (b) change in land carbon reservoir; (c) change in ocean carbon reservoir. Results are shown for simulations with seven CMIP6 Earth system models and the University of Victoria Earth System Climate Model (UVic ESCM) of intermediate complexity forced with 100 PgC instantaneously removed from the atmosphere. The 'pulse' removal is applied from a model state in equilibrium with a pre-industrial atmospheric CO₂ concentration (CDRMIP experiment CDR-pi-pulse; Keller et al., 2018b). Changes in land and ocean carbon reservoirs are calculated relative to a pre-industrial control simulation. Data for the UVic ESCM is from Zickfeld et al. (2021). Further details on data sources and processing are available in the chapter data table (Table 5.SM.6).

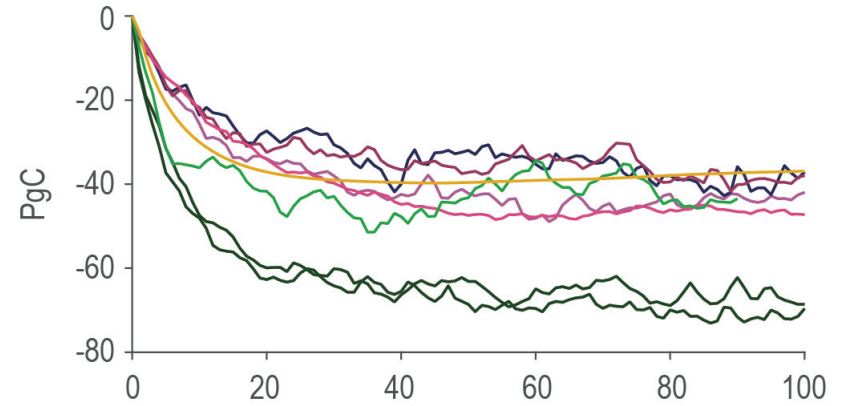


Carbon cycle response to instantaneous carbon dioxide (CO₂) removal from the atmosphere

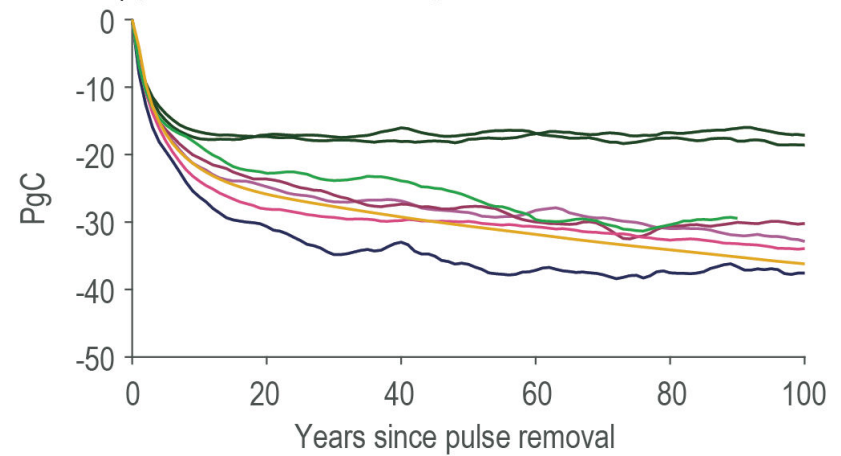
(a) Atmospheric CO₂ concentration



(b) Land carbon change



(c) Ocean carbon change



Carbon sink response in a scenario with net carbon dioxide (CO₂) removal from the atmosphere

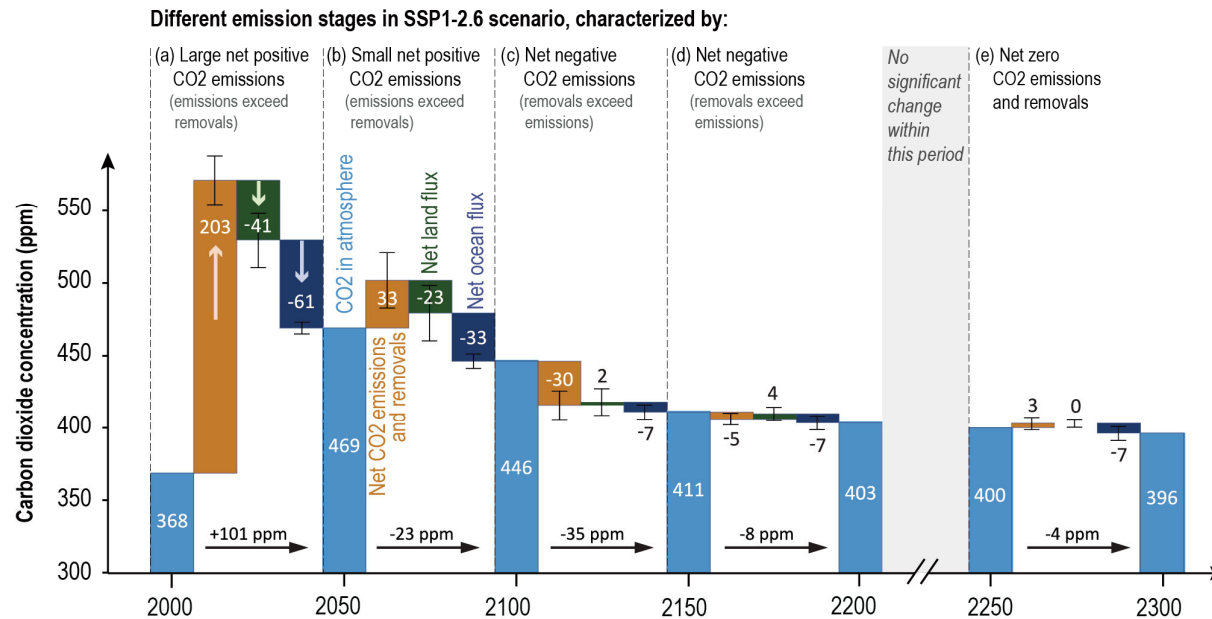
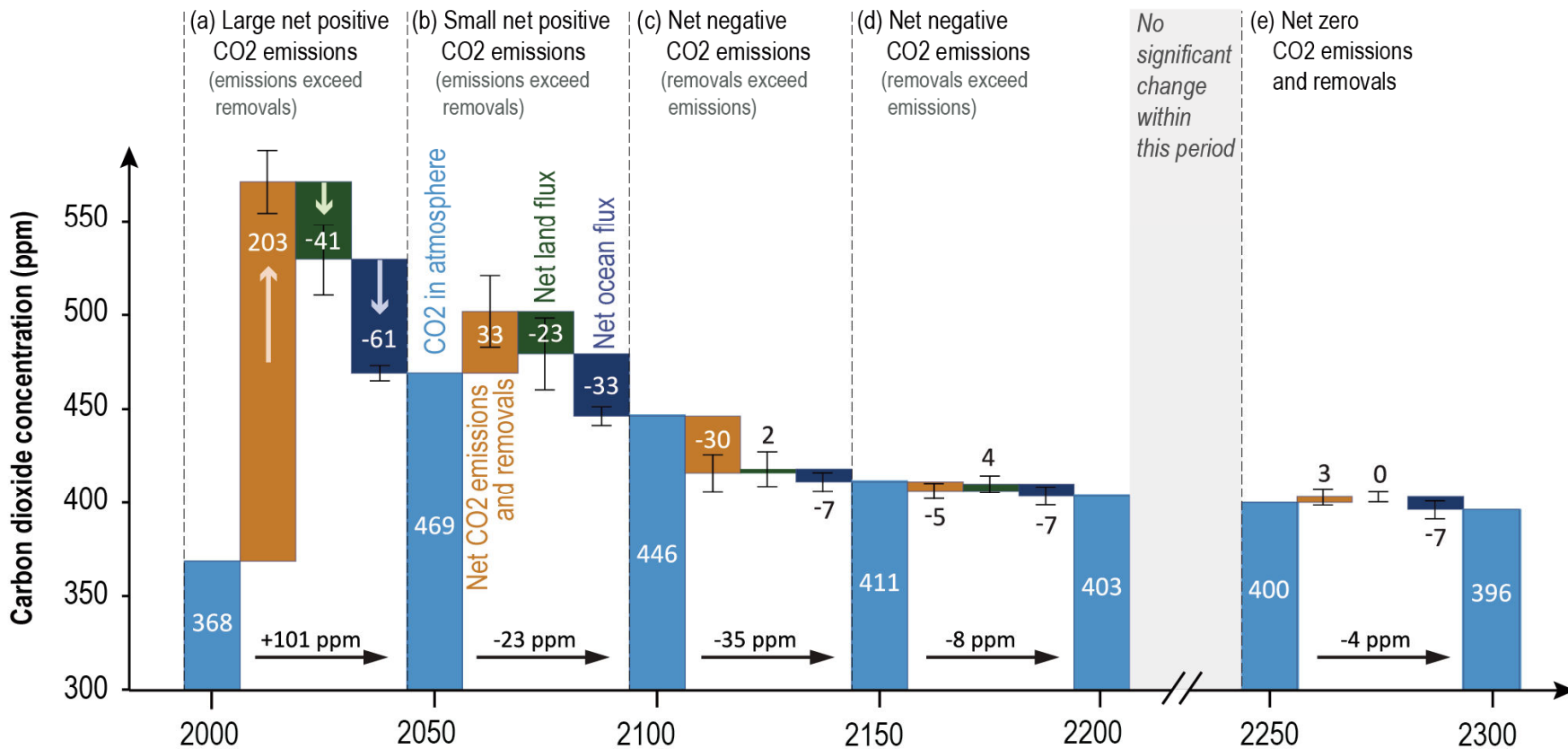


Figure 5.33 | Carbon sink response in a scenario with net carbon dioxide (CO₂) removal from the atmosphere. Shown are CO₂ flux components from concentration-driven Earth system model (ESM) simulations during different emissions stages of SSP1-2.6 and its long-term extension: **(a)** Large net positive CO₂ emissions; **(b)** small net positive CO₂ emissions; **(c)**, **(d)** net negative CO₂ emissions; **(e)** net zero CO₂ emissions. Positive flux components act to raise the atmospheric CO₂ concentration, whereas negative components act to lower the CO₂ concentration. Net CO₂ emissions, land and ocean CO₂ fluxes represent the multi-model mean and standard deviation (error bar) of four ESMs (CanESM5, UKESM1, CESM2-WACCM, IPSL-CM6a-LR) and one Earth system model of intermediate complexity (UVic ESCM; Mengis et al., 2020). Net CO₂ emissions are calculated from concentration-driven ESM simulations as the residual from the rate of increase in atmospheric CO₂ and land and ocean CO₂ fluxes. Fluxes are accumulated over each 50-year period and converted to concentration units (ppm). Further details on data sources and processing are available in the chapter data table (Table 5.SM.6).

Carbon sink response in a scenario with net carbon dioxide (CO₂) removal from the atmosphere

Different emission stages in SSP1-2.6 scenario, characterized by:



Statements in the Executive Summary

Biogeochemical Implications of Carbon Dioxide Removal and Solar Radiation Modification (3)

Wide-ranging side-effects of CDR methods have been identified that can either weaken or strengthen the carbon sequestration and cooling potential of these methods and affect the achievement of sustainable development goals (*high confidence*). Biophysical and biogeochemical side-effects of CDR methods are associated with changes in surface albedo, the water cycle, emissions of CH₄ and N₂O, ocean acidification and marine ecosystem productivity (*high confidence*). These side-effects and associated Earth system feedbacks can decrease carbon uptake and/or change local and regional climate, and in turn limit the CO₂ sequestration and cooling potential of specific CDR methods (*medium confidence*). Deployment of CDR, particularly on land, can also affect water quality and quantity, food production and biodiversity, with consequences for the achievement of related sustainable development goals (*high confidence*). These effects are often highly dependent on local context, management regime, prior land use, and scale of deployment (*high confidence*). A wide range of co-benefits are obtained with methods that seek to restore natural ecosystems or improve soil carbon (*high confidence*). The biogeochemical effects of terminating CDR are expected to be small for most CDR methods (*medium confidence*). {5.6.2.2; Figure 5.36; Cross-Chapter Box 5.1}



Characteristics of carbon dioxide removal (CDR) methods, ordered according to the time scale of carbon storage

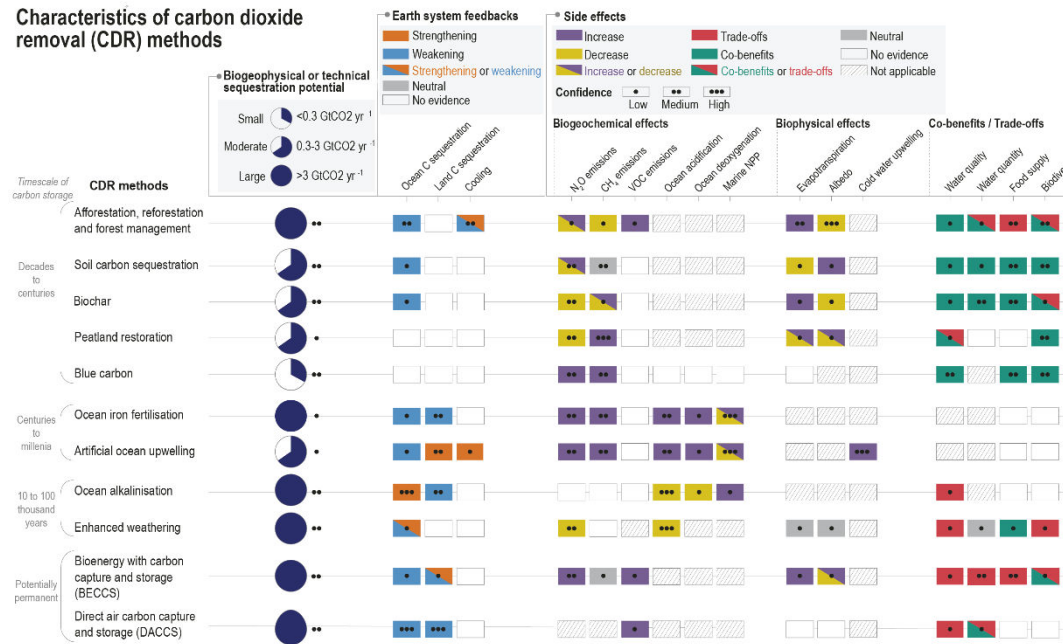
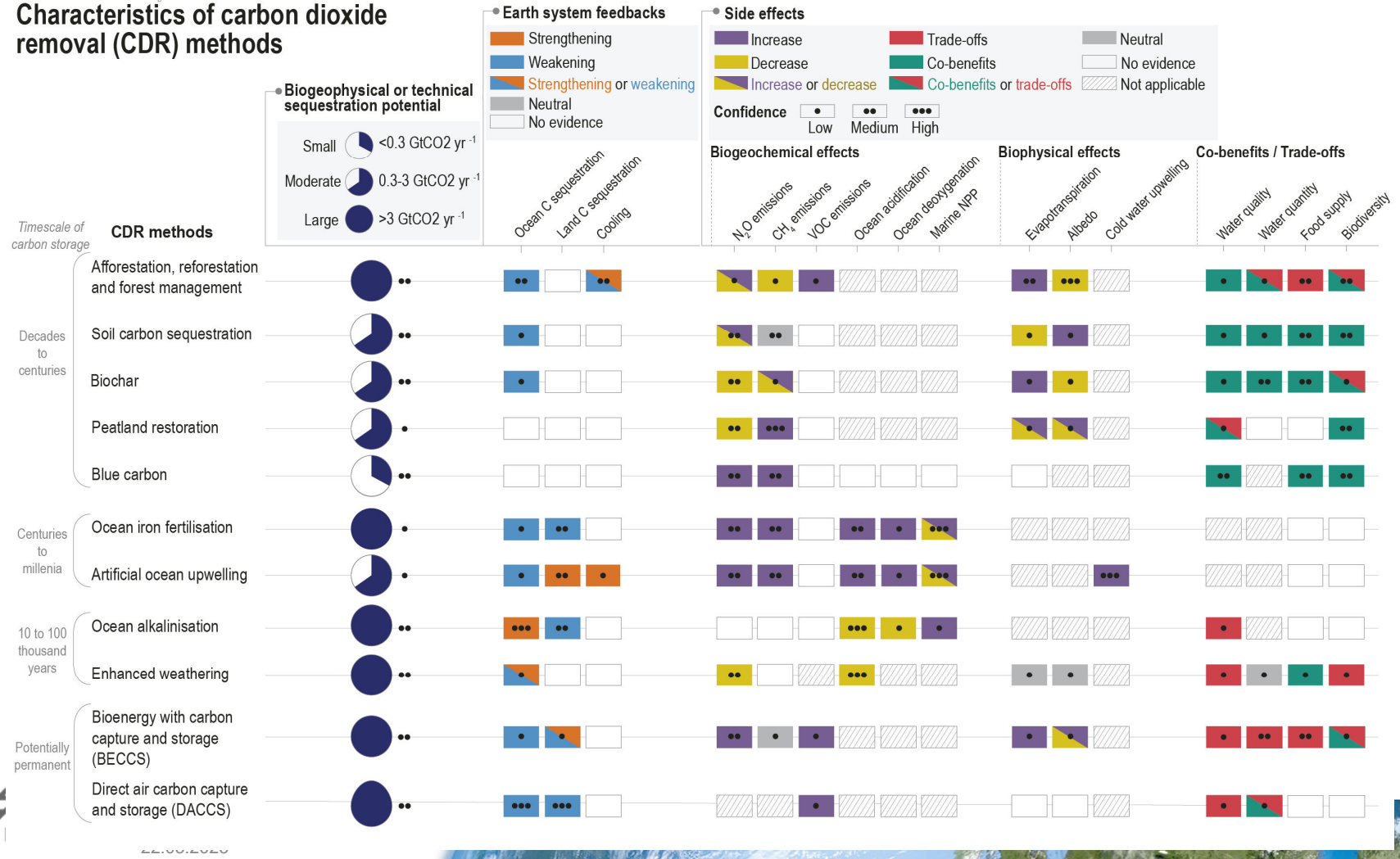


Figure 5.36 | Characteristics of carbon dioxide removal (CDR) methods, ordered according to the time scale of carbon storage. The first column shows biogeophysical (for open-ocean methods) or technical (for all other methods) sequestration potentials (i.e., the sequestration potentials constrained by biological, geophysical, geochemical limits and thermodynamics and, for technical potentials, availability of technologies and practices; technical potentials for some methods also consider social or environmental factors if these represent strong barriers for deployment; see Glossary, Annex VII), classified into low ($<0.3 \text{ GtCO}_2 \text{ yr}^{-1}$), moderate ($0.3\text{--}3 \text{ GtCO}_2 \text{ yr}^{-1}$) and large ($>3 \text{ GtCO}_2 \text{ yr}^{-1}$) (details underlying this classification are provided in Supplementary Materials Table 5.SM.5). The other columns show Earth system feedbacks that deployment of a given CDR method would have on carbon sequestration and climate, along with biogeochemical, biophysical, and other side effects of a given method. Earth system feedbacks do not include the direct effect of CO_2 sequestration on atmospheric CO_2 , only secondary effects. For Earth system feedbacks, the colours indicate whether the feedbacks strengthen or weaken carbon sequestration and the climate cooling effect of a given CDR method. For biogeochemical and biophysical side effects the colours indicate whether the deployment of a CDR method increases or decreases the magnitude of the effect, whereas for co-benefits and trade-offs the colour indicates whether deployment of a CDR method results in beneficial (co-benefits) or adverse side effects (trade-offs) for water quality and quantity, food production and biodiversity. The details and references underlying the Earth system feedback and side effect assessment are provided in Supplementary Materials Table 5.SM.4. Further details on data sources and processing are available in the chapter data table (Table 5.SM.6).

Characteristics of carbon dioxide removal (CDR) methods



Statements in the Executive Summary

Biogeochemical Implications of Carbon Dioxide Removal and Solar Radiation Modification (4)

Solar radiation modification (SRM) would increase the global land and ocean CO₂ sinks (medium confidence) but would not stop CO₂ from increasing in the atmosphere, thus exacerbating ocean acidification under continued anthropogenic emissions (*high confidence*). SRM acts to cool the planet relative to unmitigated climate change, which would increase the land sink by reducing plant and soil respiration and slow the reduction of ocean carbon uptake due to warming (*medium confidence*). SRM would not counteract or stop ocean acidification (*high confidence*). The sudden and sustained termination of SRM would rapidly increase global warming, with the return of positive and negative effects on the carbon sinks (*very high confidence*) {4.6.3; 5.6.3}



Cumulative carbon dioxide (CO₂) uptake by land and ocean carbon sinks in response to stratospheric sulfur dioxide (SO₂) injection

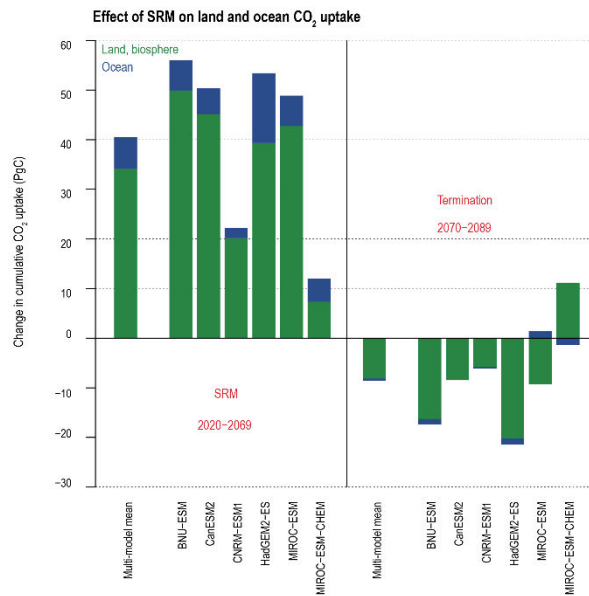
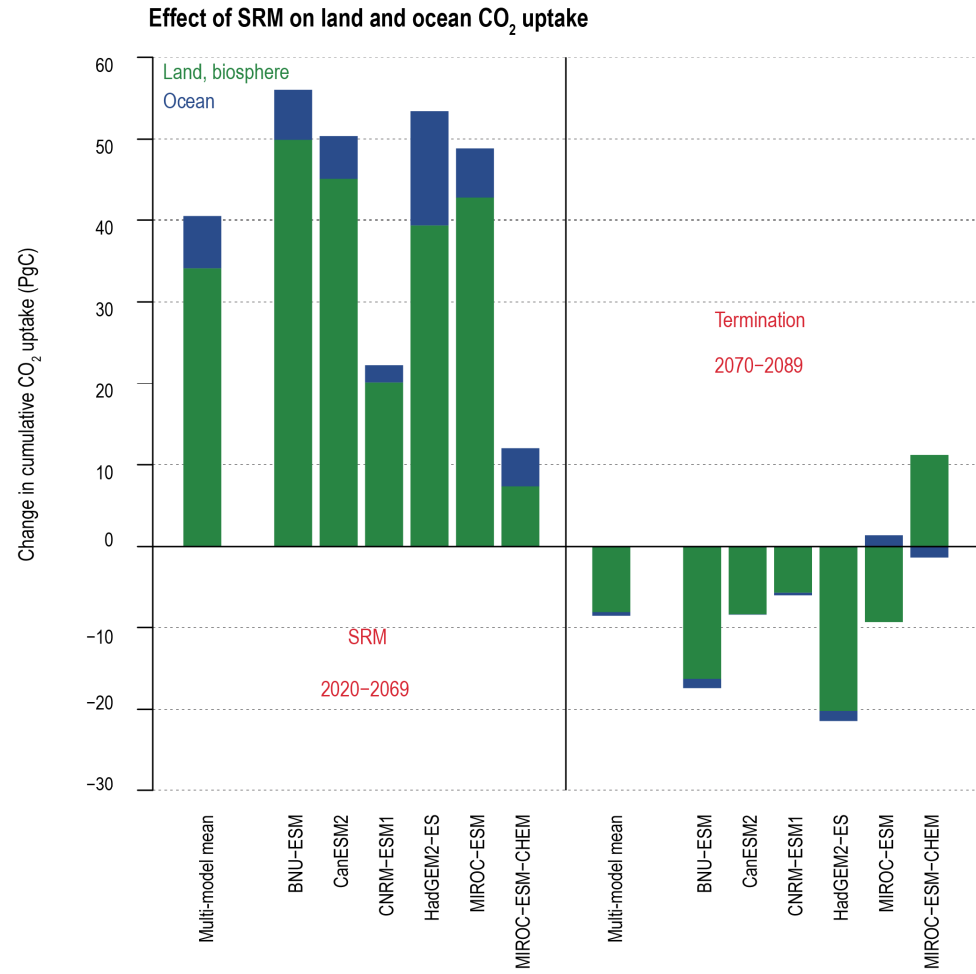


Figure 5.37 | Cumulative carbon dioxide (CO₂) uptake by land and ocean carbon sinks in response to stratospheric sulphur dioxide (SO₂) injection. Results are shown for a scenario with 50-year (2020–2069) continuous stratospheric SO₂ injection at a rate of 5 Tg yr⁻¹ applied to a RCP4.5 baseline scenario (GeoMIP experiment G4; Kravitz et al., 2011), followed by termination in year 2070. Anomalies are shown relative to RCP4.5 for the multi-model ensemble mean and for each of six Earth system models (ESMs) over the 50-year period of stratospheric SO₂ injection (left-hand side), and over 20 years after termination of SO₂ injection (right-hand side). Adapted from Plazzotta et al. (2019). Further details on data sources and processing are available in the chapter data table (Table 5.SM.6).



Cumulative carbon dioxide (CO₂) uptake by land and ocean carbon sinks in response to stratospheric sulfur dioxide (SO₂) injection



Solar Radiation Modification as Side Effect

Shipping Emissions: From Cooling to Warming of Climate—and Reducing Impacts on Health

JAN FUGLESTVEDT*
TERJE BERNTSEN

Center for International Climate and Environmental Research
Oslo (CICERO)

VERONIKA EYRING

Deutsches Zentrum für Luft- und Raumfahrt (DLR), Institut
für Physik der Atmosphäre, Oberpfaffenhofen, Germany

IVAR ISAKSEN

CICERO

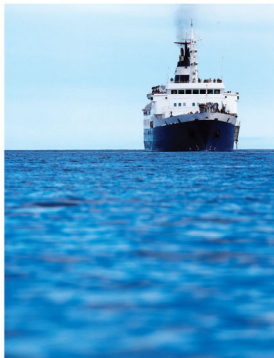
DAVID S. LEE

Manchester Metropolitan University, Manchester, U.K.

ROBERT SAUSEN

DLR, Oberpfaffenhofen, Germany

How should shipping emissions' ability to cool or warm the climate be addressed?



PHOTOS.COM

Presently, more than 80% of world trade is transported by ships (4, 5). As melting of the Arctic ice continues, shipping may find itself even more detrimental to climate and environment, as new lanes may open up in a region perhaps even more sensitive than others to new and increasing emissions. The transnational nature of this sector makes it difficult to allocate emissions and responsibilities to states; emissions from international shipping are not regulated by the Kyoto Protocol. However, the role of this sector in new climate agreements is on the agenda for the UN Climate Change Conference (COP 15) in Copenhagen in December 2009. Thus, there are several reasons why research and policymaking need to pay attention to the development of the shipping sector.

Regulations of SO₂ emissions have been discussed for over a decade within the International Maritime Organization (IMO) because of shipping's contribution to regional acidification and air pollution. The Marine Environment Protection Committee (MEPC) of the IMO recently adopted NO_x regulations and progressive reductions in SO₂ emissions from ships, with the global cap (a fuel S content limit) initially reduced from the current 4.5 to 3.5% by 2012, to be followed by progressive reduction to 0.5% by 2020, subject to a feasibility review by 2018 (6). In addition, the S limits in emission control areas will be reduced from the current level of 1.5 to 1% in 2010, and further to 0.1% in 2015.

VOL. 43, NO. 24, 2009 / ENVIRONMENTAL SCIENCE & TECHNOLOGY • 9057

10.1021/es901944t © 2009 American Chemical Society
Published on Web 11/19/2009

Shipping Emissions: From Cooling to Warming of Climate—and Reducing Impacts on Health

JAN FUGLESTVEDT*

TERJE BERNTSEN

Center for International Climate and Environmental Research
Oslo (CICERO)

VERONIKA EYRING

Deutsches Zentrum für Luft- und Raumfahrt (DLR), Institut
für Physik der Atmosphäre, Oberpfaffenhofen, Germany

IVAR ISAKSEN

CICERO

DAVID S. LEE

Manchester Metropolitan University, Manchester, U.K.

ROBERT SAUSEN

DLR, Oberpfaffenhofen, Germany

How should shipping emissions' ability to cool or warm the climate be addressed?



Solar Radiation Modification as Side Effect

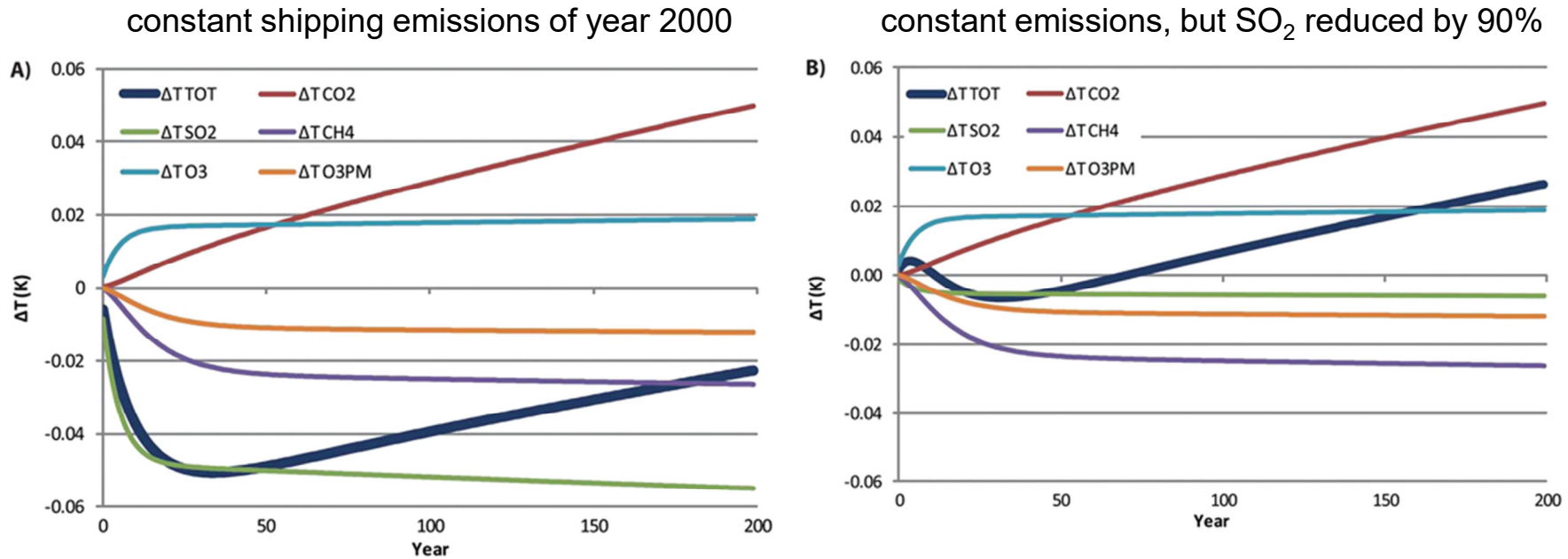


FIGURE 2. Global mean temperature changes due to emissions of CO₂ and SO₂ and NO_x-induced changes in O₃, CH₄, and O₃PM (the latter being the primary mode ozone controlled by CH₄), and the total temperature change (ΔT_{TOT}). Plotted are (a) the response to a scenario with all emissions kept constant at year 2000 levels and (b) the responses to a scenario with SO₂ emissions reduced by 90% with all other emissions at year 2000 levels.

Fuglestad et al., 2009



Chapter 6: Short-lived climate forcers

Nächste Vorlesung am 7. Juni 2022



Knowledge for Tomorrow